

Computer generated holography for 3D lithographic illumination

Dissertation

zur Erlangung des akademischen Grades

Doktoringenieur
(Dr.-Ing.)

vorgelegt der
Fakultät für Maschinenbau der
Technischen Universität Ilmenau

von Herrn
M. Sc. David Fischer

1. Gutachter: Prof. Dr. rer. nat. habil. Stefan Sinzinger
(Technische Universität Ilmenau)
2. Gutachter: Prof. Dr. sc. nat. habil. Christoph Schierz
(Technische Universität Ilmenau)
3. Gutachter: Prof. Dr. Andreas Heinrich
(Hochschule Aalen)

Tag der Einreichung: 07. Dezember 2020

Tag der wissenschaftlichen Aussprache: 21. Juli 2021

DOI: 10.22032/dbt.50106

URN: urn:nbn:de:gbv:ilm1-2021000259

Abstract

Maskless holographic lithography systems use the possibilities of light shaping in phase and amplitude enabled by holographic projection for the projection of two and three dimensional patterns. The aim is the structured illumination of photoresist, allowing the structuring of the resist. The computer generated holograms (CGH) used for this are calculated with appropriate algorithms and displayed on a spatial light modulator (SLM). In this work such a system is developed, containing algorithms for hologram calculation, a spatial light modulator for hologram display, an optical projection system with a laser as the light source, and a positioning system for substrates coated with photoresist. By optimization of the parameters of the calculation algorithms, the calibration of the hologram display technology, and the design of an appropriate projection system, patterns are projected that allow patterning of micrometer sized structures in photoresist. Good uniformity of the intensity of the projected patterns is challenging because the coherence of the light source and the hologram calculation method typically cause a speckle contrast, which manifests as intensity noise. Because the depth of focus is typically limited in microlithography, for projection on uneven substrates parts of the pattern may not be in focus at the photoresist on the substrate, thus blurred structures are exposed. In order to be able to correct this, a surface measurement method of the area to be structured and a segment-wise refocusing by adjustment of the hologram calculation are implemented. Both aspects are to be parallelized for the area to be structured. For the former, an appropriate pattern is projected via the SLM, allowing for a spatially resolved measurement of surface topography. For the latter, short distance propagation steps are integrated into the hologram calculation, in order to allow for a simultaneous projection in multiple projection planes. Finally, exposure tests are conducted, in order to confirm the performance of the system.

Zusammenfassung

Maskenlose holographische Lithographiesysteme nutzen die Möglichkeiten der gezielten Lichtformung in Phase und Amplitude durch Holographie, die für die Projektion zwei- und dreidimensionaler Muster genutzt werden kann. Das Ziel ist die strukturierte Belichtung von Fotoresist, wodurch das Einbringen von Strukturen in den Resist ermöglicht wird. Die computergenerierten Hologramme (CGH) werden dabei mittels Algorithmen berechnet und auf einem räumlichen Lichtmodulator (SLM) dargestellt. In dieser Arbeit wird ein solches System entwickelt, bestehend aus geeigneten Algorithmen zur Hologrammberechnung, einem Lichtmodulator zur Darstellung der Hologramme, einem optischen Projektionssystem mit Laser als Lichtquelle, sowie einem Positionierungssystem für zu belichtende Fotoresists auf Substraten. Durch gezielte Optimierung der Parameter der Berechnungs- und Darstellungsmethoden sowie des optischen Projektionssystems werden Muster projiziert, welche ein Einbringen von mikrometergroßen Strukturen in Fotoresist ermöglichen. Das Erreichen guter Uniformität der Intensität der projizierten Muster ist bei holographischer Projektion eine besondere Herausforderung, da durch die Kohärenz der Lichtquelle in Verbindung mit der Hologrammberechnungsmethodik üblicherweise ein Specklekontrast entsteht, der ein Intensitätsrauschen verursacht. Da in der Mikrolithographie die Schärfentiefe üblicherweise stark begrenzt ist, sind bei Projektion auf unebenen Substraten Teile des Musters an der Substratoberfläche nicht im Fokus, somit werden verschwommene Strukturen in den Fotoresist einbelichtet. Um dies zu korrigieren, werden eine Oberflächenvermessung des zu strukturierenden Gebiets sowie eine abschnittsweise Refokussierung mittels Anpassung der Hologrammberechnung umgesetzt. Sowohl die Messung als auch die angepasste Belichtung werden parallelisiert in dem zu strukturierenden Feld durchgeführt. Für ersteres wird ein geeignetes Muster durch den Lichtmodulator projiziert, welches eine orts aufgelöste Bestimmung der Oberflächenpositionen ermöglicht. Für letzteres werden Kurzstanzpropagationsschritte in die Hologrammberechnung integriert, um eine gleichzeitige Projektion in mehrere Tiefenebenen zu ermöglichen. Zuletzt zeigen Belichtungstests die Leistungsfähigkeit des Systems.

Table of Contents

Title Page	i
Abstract	iii
Zusammenfassung	v
List of Figures	xi
List of Tables	xiii
Abbreviations	xv
Symbols	xv
1 Introduction	1
2 Fundamentals and State of the Art	3
2.1 Lithography considerations	4
2.1.1 Depth of focus in lithography	4
2.1.2 Maskless optical lithography methods	5
2.1.3 Holographic lithography	5
2.2 Fundamentals of computer generated holograms (CGH)	6
2.2.1 Thin phase-only computer generated holograms	7
2.2.2 Phase wrapping	8
2.2.3 Applications of computer generated holograms (CGH)	8
2.3 Wave optics and propagation algorithms	9
2.3.1 Electromagnetic waves	10
2.3.2 Fraunhofer (far field) propagation	11
2.3.3 Angular spectrum propagation	11
2.3.4 Overview of propagation algorithms	12
2.3.5 Spatial sampling	13
2.4 Hologram calculation methods and considerations	14
2.4.1 Overview of hologram calculation algorithms	15
2.4.2 Iterative Fourier transform algorithm	16
2.4.3 Error diffusion algorithm	16
2.4.4 The noise problem in CGH: Speckle reduction	18
2.4.5 Hologram calculation for 3D projections	19

TABLE OF CONTENTS

2.5	Physical realization of computer generated holograms	21
2.5.1	Technologies for manufacturing of computer generated holograms	21
2.5.2	Technologies for dynamic display of computer generated holograms . . .	22
2.6	Summary of Chapter 2	23
3	LCoS technology aspects for holographic projection	25
3.1	LCoS technology	25
3.2	Fundamental LCoS phase effects	26
3.2.1	Pixel crosstalk	27
3.2.2	Unmodulated zero order light	28
3.2.3	Spatially varying phase response	28
3.2.4	Flicker	29
3.2.5	Aberrations caused by backplane curvature	29
3.2.6	Spatial frequency response	29
3.2.7	Tilt angle dependency	30
3.3	LCoS-SLM characterization and calibration	30
3.3.1	Phase response calibration	30
3.3.2	Pixel crosstalk measurement	32
3.3.3	Aberration measurement and correction	33
3.4	Summary of Chapter 3	41
4	Optimization of Hologram calculation	43
4.1	Quadratic phase hologram calculation	43
4.1.1	Near field projection	44
4.1.2	Far field projection	45
4.2	Optimization of 2D projection algorithm and input parameters	48
4.2.1	Test images, quality criteria, and target parameters	48
4.2.2	Simulation	48
4.2.3	Experimental validation	53
4.2.4	Inverted quadratic phase factor	56
4.3	Extension of the algorithm with short distance propagation for 3D projection .	56
4.3.1	Simulation	58
4.3.2	Experimental validation	59
4.4	Summary of Chapter 4	61
5	Optical setup for lithographic projection and surface measurement	63
5.1	Fundamental design choices	63
5.2	Off-axis projection and compensation of off-axis intensity gradient	65
5.3	Optical system for small feature projection	66
5.3.1	Choice of objective and lenses	66
5.3.2	Limitations of lateral resolution	68
5.4	Integrated optical surface measurement system	68
5.4.1	Choice of projected pattern and hologram phase for measurement	70
5.4.2	Surface scanning methods	71

5.4.3	Measurement resolution and axial offset of the lasers	72
5.4.4	System limit: surface tilt	72
5.5	Summary of Chapter 5	74
6	Lithography experiments	75
6.1	Determination of correct dose and exposure time	75
6.2	Determination of projection resolution	77
6.3	Defocus variation	78
6.4	Summary of Chapter 6	79
7	Summary and Outlook	81
	References	83

List of Figures

2.1	CGH projection schematic	4
2.2	Schematic of the DOF for parallel patterning on nonplanar surfaces	6
2.3	Wrapped and unwrapped lens phase	8
2.4	Examples of target patterns for hologram calculation	9
2.5	Propagation between transversal planes	10
2.6	Effect of spatial discretization	14
2.7	Schematic of the IFTA	17
2.8	Schematic of error diffusion algorithm	18
2.9	Example for speckle contrast and noise window for double constraint GSA	20
2.10	Schematic of hologram calculation for 2D and 3D projections	20
3.1	Simplified LCoS structure	26
3.2	Phase modulation with liquid crystals	27
3.3	LCoS time invariant phase imperfections	27
3.4	Projection of Siemens star with zero order spot	28
3.5	Schematic of LCoS flicker effect	29
3.6	Incorporation of LCoS in optical setups	30
3.7	Calibration of phase response	31
3.8	Setup for measurement of diffraction orders	32
3.9	Results for measurement of diffraction orders	33
3.10	Effect of backplane aberrations	34
3.11	Preliminary SLM aberration measurement with Michelson setup	35
3.12	Shack-Hartmann principle	35
3.13	Schematic of optical setup for wavefront measurement	36
3.14	Focal spots from different micro lens arrays	37
3.15	Micro lens designs and resulting focal spot arrays on camera sensor	37
3.16	Focal spot displacement	39
3.17	Block diagram of spot detection and wavefront calculation	39
3.18	Measurement with aberration compensation phasemap	39
3.19	Wavefront measurements with Shack-Hartmann-Sensor	40
4.1	Schematic of quadratic phase Fresnel hologram calculation	44
4.2	Optical setup for far field quadratic phase factor calculation	47
4.3	Schematic of far field quadratic phase hologram calculation algorithms	47
4.4	Test images for evaluation of hologram calculation algorithms	49

LIST OF FIGURES

4.5	Parameter variation of quadratic phase factor with simulation	50
4.6	Simulated parameter variation of quadratic phase factor: initial hologram amplitude	50
4.7	Parameter variation of scaling factor for comparison of algorithm variations . .	51
4.8	Parameter variation of zero intensity frame	52
4.9	Simulation of obstructed hologram	53
4.10	Schematic of optical system	54
4.11	Comparison of algorithm variations with experiments	55
4.12	Experimental evaluation of parameter variation of scaling factor	55
4.13	Schematic of inverted quadratic phase	56
4.14	Schematic of error diffusion multi plane hologram calculation	57
4.15	Schematic of multi plane hologram calculation	58
4.16	Schematic for simulation of multi plane holograms	58
4.17	Analysis of 3D projection in experiment and simulation by AS propagation . .	60
5.1	Optical laboratory setup	64
5.2	Off-axis intensity limited by sinc^2 function	65
5.3	Schematic of projection system	67
5.4	Schematic of illumination optical subsystem	69
5.5	Schematic of imaging and measurement subsystem	69
5.6	Holograms for measurement projection	70
5.7	Mechanical scanning for surface measurement	71
5.8	Optical scanning for surface measurement	72
5.9	Surface measurements by focal spot intensity evaluation	73
5.10	Schematic for measurement of tilted surfaces	73
6.1	Schematic of measurement and structuring process	76
6.2	Measurement of projection size	77
6.3	Variation of exposure time	77
6.4	Pattern in Photoresist for determination of resolution	78
6.5	Pattern in Photoresist without corrections and optimizations	78
6.6	Variation of defocus	79

List of Tables

2.1	Overview of propagation algorithms	13
2.2	Parameters for categorization of common computer generated holograms	14
2.3	Overview of technologies for the dynamic display of holograms	22

Abbreviations

AS angular spectrum
CCD 'charge-coupled device': camera sensor
CGH computer generated hologram
CW continuous wave
DBS direct binary search
DMD digital micromirror device
DOE diffractive optical element
DOF depth of focus
ECB electrically controlled birefringence
ED error diffusion
FFT Fast Fourier Transform

GSA Gerchberg-Saxton algorithm
IFTA iterative Fourier transform algorithm
LCD liquid crystal display
LCoS liquid crystal on silicon
LC liquid crystal
LED light emitting diode
LUT look-up table
NA numerical aperture
ORA optimal-rotation-angle
PAN parallel aligned nematic
PSNR peak signal-noise ratio
RMS root mean square
RSD relative standard deviation
RS Rayleigh-Sommerfeld
SBP space-bandwidth product
SF scaling factor
SHS Shack-Hartmann sensor
SLM spatial light modulator

Symbols

A complex amplitude in source plane
 U complex amplitude in target plane
 Δ_u, Δ_v spatial frequency sampling interval
 Δ_x, Δ_y spatial sampling interval

f focal length
 \mathcal{F} Fourier transform
 m, n pixel coordinates
 ϕ phase / phase distribution
 s_h spatial extent of source signal
 s_p spatial extent of target signal
 u, v spatial frequency coordinates
 x, y spatial (transversal) coordinates
 λ wavelength
 z_p propagation distance

1

Introduction

Optical microlithography is a key tool in the process of manufacturing various types of microstructures, for example in semiconductors/microelectronics, micro optics, or micromechanical systems. It is used to create patterns in photoresist that can then be etched into a substrate. A central trade off in optical lithography is that of throughput versus flexibility. Mask-based patterning offers high throughput, but any change to the pattern requires manufacturing of a new mask beforehand. Direct write patterning offers very high flexibility by serial scanning of an electron or laser focus spot across a substrate, however throughput is greatly limited, especially when smaller structures and larger patterning fields are involved. While both methods have many applications in research and industry, the area of flexible patterning at increased throughput is filled by flexible (maskless) parallelized patterning processes that commonly use the dynamic pixel-wise light modulation of spatial light modulator (SLM) based optical setups. However, these setups are typically limited to structuring of planar surfaces because they use 2D pattern projection. Microstructuring on nonplanar surfaces, for example on lens surfaces, is also desirable due to the increased degrees of freedom for system design.

At this point, the projection with computer generated holograms (CGH) can offer an extension of the process window. It allows for dynamic three-dimensional projection of patterns, which can enable the aforementioned parallel microstructuring on nonplanar substrates. In computer generated holography, no physical recording of a wavefront is used. Hologram calculation algorithms are used to calculate a wavefront that reconstructs a digitally generated object. For a physical reconstruction of the pattern, the calculated hologram has to be manufactured with a suitable method, or displayed on a spatial light modulator (SLM). A SLM is a pixelated element (micro display), capable of dynamic display of phase- or amplitude patterns.

In this work the flexible (maskless) parallelized submicrometer patterning on nonplanar surfaces with holographic projection is investigated with the goal to achieve structuring on nonplanar substrates, with structure sizes smaller than demonstrated before.

To achieve this goal, suitable methods are required. Since one of the inherent challenges of projection with CGHs is speckle contrast, an optimized hologram calculation algorithm is developed for achieving high uniformity of the projected three-dimensional pattern.

Furthermore a well-calibrated SLM for dynamic display of holograms, and an optical system for projection and demagnification to achieve the desired pattern resolution are necessary. All three aspects are elaborated on in separate chapters of this work.

Chapter 2 gives background on the fundamentals required for CGH calculation, the methods for 3D projection, physical reconstruction methods, the main aspects important for reconstruction quality, the depth of focus (DOF) problem in lithography and how holographic lithography can be beneficial for lithography on nonplanar surfaces.

Chapter 3 introduces the liquid crystal on silicon (LCoS) technology used as a phase-only SLM for hologram display, and details the various technological aspects that can degrade phase modulation and thus projection quality. Further, the characterization and calibration of the device used in this work is described.

Chapter 4 contains the implementation, evaluation and optimizations of quadratic phase-based hologram calculation algorithms that are used in this work. A detailed analysis of the input parameters of the algorithms is conducted for optimization of projection quality and diffraction efficiency. Also, a method for extension of the algorithm to allow 3D projection is investigated and validated experimentally.

Chapter 5 describes the optical system design which is required for bringing the projected pattern into the photoresist. The choices for components and system parameters are elaborated and the optical system performance is estimated. Further, in order to be able to measure the position of the nonplanar surfaces to be structured on, the optical system is extended by a surface measurement method based on dynamic pattern projection available through SLM. The capabilities and limits of the measurement method are investigated.

Chapter 6 contains the lithography tests conducted with the optical system, using the components and methods described in the previous three chapters. This is done to experimentally validate the functionality of the designed lithography system.

Chapter 7 is the summary and outlook. The challenges of this work and the approaches for solving them are summarized, and the main achievements of this work are presented. Also, the next steps and possible optimizations are outlined.

2

Fundamentals and State of the Art

In this chapter, first, the depth of focus (DOF) challenge in lithography, an overview of various optical lithography methods, and the state of the art in dynamic holographic lithography methods are given, to motivate this work and place it within context. Then, the basic properties and parameters of computer generated holograms (CGH) are described. Also, some examples of applications of CGH are given as an introduction to CGH. Furthermore, the fundamentals of propagation algorithms are described, as these are the basis for CGH calculation. For this, first the approximations used and the challenges in implementation of the algorithms on a computer are discussed, and then the properties of the algorithms used in this work are described in more detail. The description of hologram calculation methods includes an overview, the algorithms used in this work, consideration of the speckle problem, and 3D projection. For the physical implementation of calculated CGH, common methods are described with a distinction made between dynamic and static hologram display/manufacturing methods. Fig. 2.1 is an overview of the steps and methods used for CGH projection in this work.

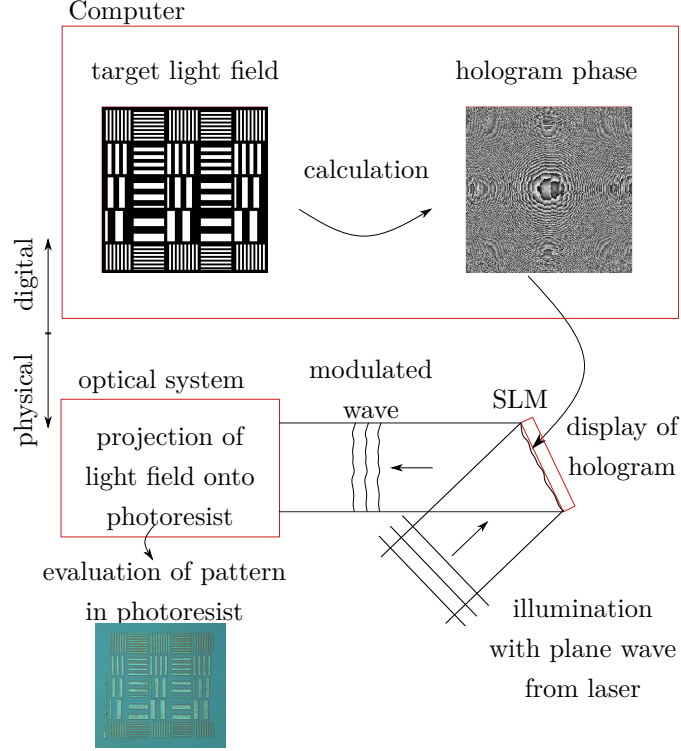


Figure 2.1: CGH projection schematic - Schematic of the components for CGH projection of patterns on photoresist. SLM, spatial light modulator.

2.1 Lithography considerations

In this section, the depth of focus problem in lithography is described, which is the main motivation for this work. Furthermore, an overview is given of lithographic methods that use spatial light modulators (SLM) and computer generated holograms (CGH) to implement a parallelized patterning on planar or nonplanar surfaces to place this work in the context of similar designs from literature.

2.1.1 Depth of focus in lithography

The depth of focus (DOF) is an important factor in lithography, because it is connected to the resolution via the numerical aperture (NA) and the wavelength. Generally, to achieve better resolution, the wavelength can be decreased or the NA can be increased, both of which decrease the available DOF. For patterning of especially small structures the DOF will also be small, increasing the probability that parts of the lithographic pattern are projected out of focus.

In more detail, for the structuring of small feature sizes R , according to the Rayleigh criterion

$$R = k_1 \cdot \frac{\lambda}{\text{NA}}, \quad (2.1)$$

a large NA is required. Even though the depth of focus (DOF) is application dependent, the Rayleigh DOF [1]

$$\text{DOF} = k_2 \cdot \frac{\lambda}{\text{NA}^2} \quad (2.2)$$

can be used as a first estimate, showing that the DOF decreases rapidly as the numerical aperture (NA) increases. k_1 and k_2 are process dependent factors. In projection setups the effective NA may be lower than the nominal NA of the objective in use if its entrance pupil is underfilled.

The usable DOF can depend on a lot of factors pertaining the desired structure in the photoresist, such as the pattern shape, desired linewidth, and desired sidewall angle [2]. To account for these factors, for lithographic processes the DOF is commonly multiplied with a factor k_2 which results from all process parameters and requirements.

Furthermore, wafer topography, varying exposure dose and optical aberrations may degrade the available DOF. The presence of astigmatism for example causes line patterns of different orientations to have different focal planes [1].

In holographic projection setups, the DOF can also be influenced by the hologram calculation method if the projection phase is restricted.

2.1.2 Maskless optical lithography methods

Optical lithography is a typically contactless pattern transfer step for manufacturing small structures (micro-/nanometer sized).

Lithography processes for maximum throughput are often mask-based. For this, a previously manufactured photomask is brought in close proximity to a photoresist coated substrate or the mask pattern is projected on the substrate. However, this process is relatively inflexible since a new mask is needed for every new illumination step.

Other approaches are electron beam lithography and laser beam lithography, which are scanning a single light or electron beam across a substrate. These are serial processes and have very long processing times for patterning of larger areas.

To decrease processing time, SLM-based maskless lithography was developed, dynamically projecting the amplitude pattern displayed on a micro display (typically DMD or LCoS) onto the photoresist [3]. Since this method is limited to flat projections, considerable effort is required to allow the structuring of non-flat surfaces [4].

2.1.3 Holographic lithography

Since a high NA is necessary for the projection of single micrometer/submicrometer structures in lithography, the depth of focus is small, which can cause problems with out-of-focus projection, especially when nonplanar surfaces are involved. In serial scanning laser lithography, additional scanning along the optical axis can solve this, but for parallel processing applications this has limited use because segments of the projection are out-of-focus, see Fig. 2.2. Usage of z -scanning and disabling the projection in out-of-focus regions can prevent exposure of defocused structures at the cost of increased processing time [4].

Holographic 3D projection with CGHs can improve on this, enabling flexible parallel patterning on nonplanar surfaces by compensating for the defocus blur on nonplanar surfaces when using high-NA demagnification/structuring. And with the potential for controlling the phase of the projected pattern, additional degrees of freedom beneficial for lithography may be obtained.

The usage of high degrees of freedom for light shaping available with CGHs in combination with the dynamic hologram display with SLMs for patterning of small structures has been demonstrated in literature [5–10].

The publications most relevant to this work are summarized in the following:

- Structure sizes of $\approx 4\mu\text{m}$ were achieved on a planar substrate with an LCoS-SLM and a projection setup [6].
- Structure sizes of $\approx 1\mu\text{m}$ were achieved on a planar substrate with an LCD-SLM and a projection setup with multi-photon polymerization processes [7].
- Structure sizes of $\approx 500\text{nm}$ were achieved on a planar substrate with an LCoS-SLM and a projection setup with an immersion objective [8].
- Structure sizes of $\approx 10\mu\text{m}$ were achieved on a nonplanar surface with an LCoS-SLM without an additional optical projection setup [9].

Furthermore, patterning on nonplanar substrates has been achieved with CGHs that have been manufactured instead of displayed on an SLM [11, 12] with structure sizes of $100\mu\text{m}$ and $66\mu\text{m}$, respectively.

In conclusion, holographic lithography on nonplanar surfaces has not been achieved with single micrometer or submicrometer structure sizes, which is attempted in this work.

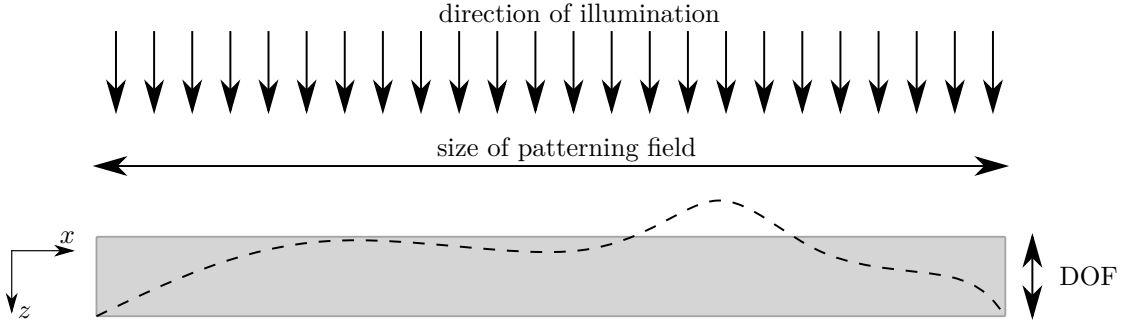


Figure 2.2: Schematic of the DOF for parallel patterning on nonplanar surfaces - When patterning a larger field on nonplanar surfaces (dashed line), the local surface height difference may exceed the depth of focus (DOF), marked by the grey rectangle.

2.2 Fundamentals of computer generated holograms (CGH)

The main tool for light shaping used in this work is computer generated holograms (CGH). This section serves as an overview of the characteristics and applications of CGHs.

In general, a hologram is a recording of an interference pattern of a reference beam with light that has been reflected off or transmitted by an object. Monochromatic coherent light and a suitable recording material are required for this. When the recorded hologram is illuminated by coherent light with the correct parameters, a 3D image of the object is reconstructed.

The main difference of computer generated holograms compared to other types of holograms is that CGHs do not require a real object to be recorded for generation of the hologram. The hologram parameters and the desired projected patterns are generated completely digitally in a computer.

Generally, holographic optical elements modulate the phase or amplitude (or both) of the incident light pixelwise, aiming to create a target (2D or 3D) intensity distribution at a certain distance to the element.

The main advantage is the extremely high flexibility for light shaping in amplitude and phase, limited only by the degrees of freedom of the hologram display method and the computing power for hologram calculation. The disadvantages are that standard configurations require a coherent monochromatic laser light source, and that standard iterative hologram calculation methods cause high speckle contrast. Additionally, for many applications the phase calculation can be simplified drastically by analytic calculation methods, not requiring the methods of CGH.

The procedure for generating CGHs is the following:

1. A target light field for a given application is calculated.
2. Hologram calculation algorithms optimize hologram characteristics.
3. The hologram is implemented with an appropriate manufacturing/display technology.

2.2.1 Thin phase-only computer generated holograms

A hologram is classified as thin when the so called Q factor is

$$Q = \frac{2\pi\lambda_0 d}{n\Lambda^2} < 2\pi \quad (2.3)$$

with λ_0 wavelength in vacuum, d layer thickness, n refractive index, Λ grating period [13]. This condition is usually true for surface relief holograms manufactured by photolithography and for holograms displayed on liquid crystal on silicon spatial light modulator (LCoS-SLM) devices. CGH manufacturing/display methods are described in more detail in section 2.5.

Compared to other types of holograms, thin phase-only CGHs have the advantages of

- ease of calculation with plane-to-plane propagation algorithms
- parallelized manufacturing with established lithography processes
- availability of phase-only SLMs for dynamic hologram display

Compared to amplitude holograms the main advantage of phase-only holograms is the higher efficiency because no light is blocked by the hologram. Manufacturing of phase-only holograms however is more difficult due to the height of the phase levels having relatively strict tolerances ($\ll \lambda$) to prevent loss of efficiency. Complex modulation of both phase and amplitude independently, while possible, decreases efficiency because of the amplitude modulation and also imposes further restrictions on the manufacturing process. SLMs for uncoupled phase and amplitude modulation are not available.

With phase-only holograms, a direct wave optical propagation to the hologram is not sufficient because both the hologram phase and the projection phase are unknown. Section 2.4 describes several of the algorithms that have been developed to numerically optimize the hologram phase distribution to achieve high projection quality.

2.2.2 Phase wrapping

Due to the limited phase shift achievable with lithographic structuring and LCoS technology, the displayable continuous phase distributions are greatly limited. However, due to usage of coherent monochromatic light, phase wrapping can be used, taking advantage of the constructive interference when two beams are phase shifted by 2π (one wavelength). As an example, a lens phase is displayed in Fig. 2.3 wrapped and unwrapped, demonstrating that without phase wrapping, a much larger phase modulation would be required than with phase wrapping.

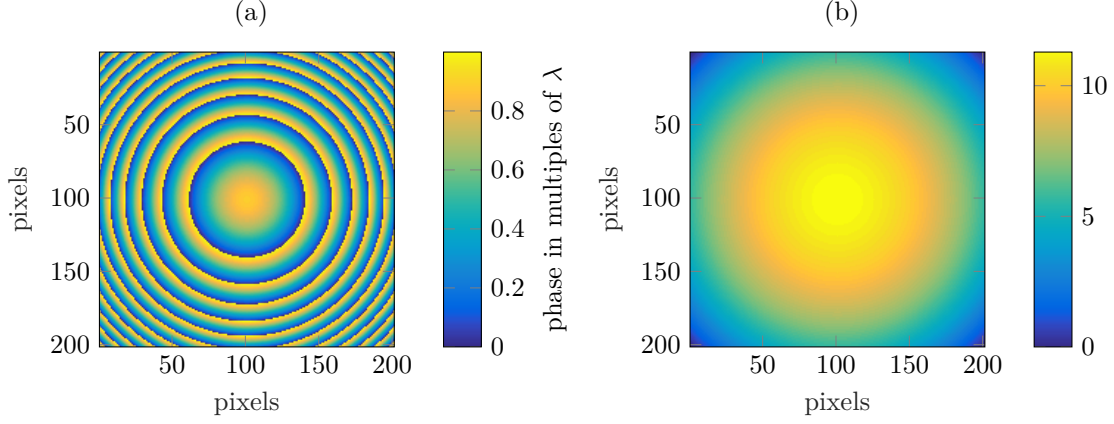


Figure 2.3: Wrapped and unwrapped lens phase - (a) A maximum phase difference of λ is sufficient for display of the wrapped lens. (b) A phase difference of $>10\cdot\lambda$ would be required for display of the same lens phase unwrapped.

2.2.3 Applications of computer generated holograms (CGH)

Because of the high flexibility of light shaping with CGH, many different applications exist which may require vastly different hologram calculation approaches. An overview of common applications is given in the following, along with some target patterns.

1. Holographic image projection. The holographic projection of images or video frames to be viewed by human eyes. Speckle-reduced, multi-color projection is desired. Test images from image processing, such as "Mandrill, Peppers, Cameraman" are often used as target patterns for the optimization of hologram calculation algorithms. Examples in Fig. 2.4 (a),(b),(c).
2. Holographic lithography. The holographic projection of patterns to selectively cure photoresist in photolithography. Targets are usually binary intensity patterns consisting of small shapes and contain a significant number of zero intensity pixels. Example in Fig. 2.4 (d).
3. Holographic beam splitters. Periodic phase profiles are used to create the interference pattern of a grating, consisting of multiple diffraction orders. The design of the phase profile along each period can be optimized with holographic methods to influence the intensity distribution of the diffraction orders.

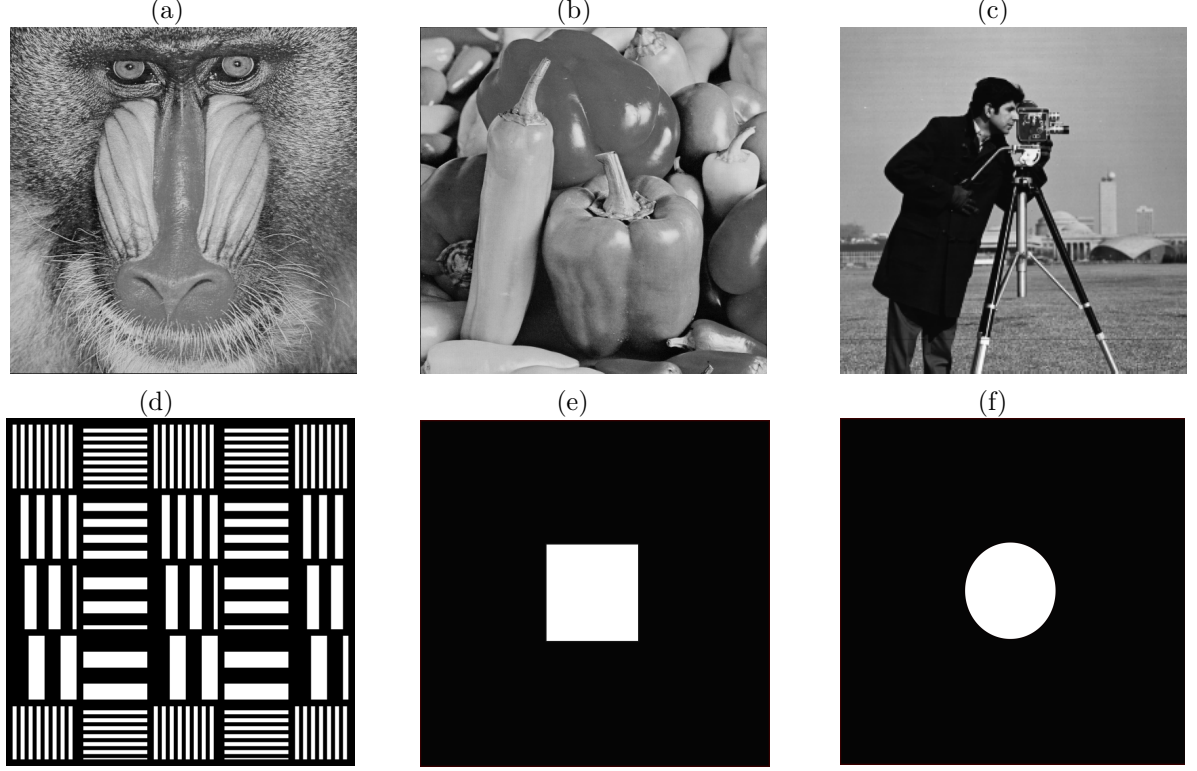


Figure 2.4: Examples of target patterns for hologram calculation [14, 15].

4. Holographic beam shapers are used e.g. in laser materials processing, or for illumination applications. The target intensity pattern is usually a large, uniform illumination area surrounded by a zero intensity frame. Figure 2.4 (e),(f) show the target image for a gaussian to square/circular tophat beam shaper.
5. Null test CGH. In interferometry the measurement of wavefronts is done by evaluation of the interference pattern of a test wave with a reference wave. For more complex surface shapes such as aspheres, the distorted test wave may have to be adjusted to the planar reference wave in order to obtain an interference pattern. This can be done with a CGH that transforms the test wavefront that would be reflected from the ideal surface into a plane wave, allowing to evaluate the difference from the ideal surface with interferometry. These CGHs are optimized for a defined wavefront with constant intensity.

2.3 Wave optics and propagation algorithms

For hologram calculation algorithms, an accurate calculation of the wave field is necessary. This section deals with wave optics and includes the validity regions of the propagation algorithms used in this work. The Fraunhofer propagation and the angular spectrum propagation, which are used in this work, are described, and an overview of commonly used propagation algorithms follows to give context to the choice of propagation algorithms in this work. Moreover, the sampling conditions for implementation of the propagation algorithms on a computer is discussed.

2.3.1 Electromagnetic waves

Electromagnetic radiation is fully described by Maxwell's equations. Several simplifications are typically made in optics, whereas light propagates in a homogenic, dielectric, and isotropic medium [16]. Furthermore, in this work, light fields are calculated with scalar diffraction theory. The major conditions for the validity of scalar diffraction theory are minimum structure sizes that are large compared to the wavelength [13], and numerical apertures (NA) smaller than 0.6 [17].

Further assuming time invariance and monochromatic light, and neglecting polarization, the Helmholtz equation results as the basis for scalar diffraction theory:

$$(\nabla^2 + k^2) U = 0 \quad (2.4)$$

with ∇^2 the laplace operator, U complex amplitude as a function of position and the wave number $k = 2\pi/\lambda$.

Based on diffraction integrals that fulfill the Helmholtz equation for certain validity regions, propagation algorithms can be derived for description of more intricate wave fields, with different approximations used for simplification of the calculation. Section 2.3.4 provides an overview of common propagation algorithms. Commonly, propagation algorithms are used for description of the propagation of coherent monochromatic electromagnetic waves from one transversal plane to another, whereas the complex amplitude consisting of phase ϕ and amplitude A_0 in one plane z_0

$$A(x', y', z_0) = A_0(x', y', z_0) \cdot \exp(i \cdot \phi(x', y', z_0)) \quad (2.5)$$

with $i^2 = -1$ is sufficient to calculate the complex amplitude in another plane z_1 , visualized in Fig. 2.5.

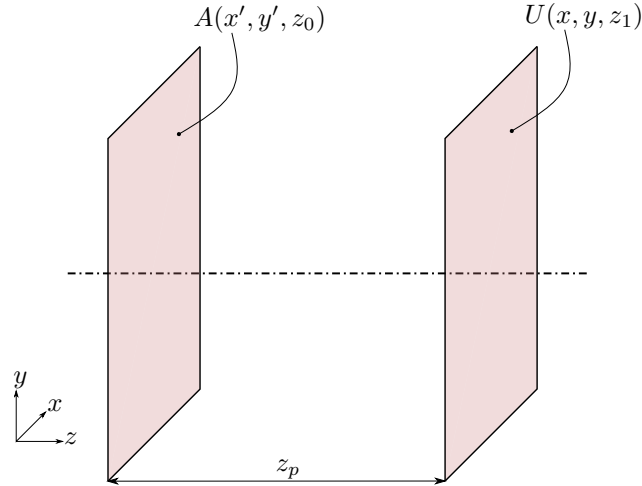


Figure 2.5: Propagation between transversal planes: left: source plane; right: target plane; z_p , propagation distance; x, y , transversal plane coordinates. A , complex amplitude in source plane; U , complex amplitude in target plane.

A major approximation is made when Fresnel- or Fraunhofer diffraction is calculated: The paraxial approximation, which assumes that the field component along the optical z -axis can

be neglected ($k_z \ll k$) and decreases the accuracy for regions that are not close to the optical axis.

2.3.2 Fraunhofer (far field) propagation

A strong approximation for the calculation of optical fields is the Fraunhofer approximation. It is valid for paraxial systems in the far field for very long propagation distances [13]

$$z_p > \frac{2D^2}{\lambda} \quad (2.6)$$

with D aperture dimension, λ wavelength. Caused by the paraxial approximation included with it, for higher diffraction angles ($> 10^\circ$ [18]) the calculation becomes inaccurate. The Fraunhofer approximation diffraction integral is [13]

$$U(x, y, z_1) = \frac{e^{(-ikz_p)} e^{\left[-\frac{i\pi}{\lambda z_p}(x^2+y^2)\right]}}{i\lambda z_p} \iint_{\infty} A(x', y', z_0) e^{\left[-\frac{i2\pi}{\lambda z_p}(xx'+yy')\right]} dx' dy' \quad (2.7)$$

with a quadratic phase factor before the integral. The integral is a two-dimensional Fourier transform, so if just the intensity of the result is needed, the calculation can be simplified to

$$U(x, y, z_1) = \mathcal{F}[A(x', y', z_0)] \quad (2.8)$$

with \mathcal{F} two-dimensional Fourier transform, A and U complex amplitude in the source plane and target plane, respectively, see Fig. 2.5.

It is especially useful in the field of Fourier optics, because the far field is often imaged at a finite distance with an optical Fourier transform by a converging lens. Because the far field amplitude is the same as the spectral amplitude, the numerical implementation can be done with one two-dimensional Fourier transform and multiplication with a phase factor. When using a converging lens to perform the optical Fourier transform, the phase factor disappears if the input plane coincides with the front focal plane of the lens, thus the relation can be described by just the Fourier transform [13]. With FFT-based numerical implementation of the lens Fourier transform, the sampling in the target plane Δ_x is dependent on λ , the focal length f , and the spatial extent s_h of the signal in the source plane

$$\Delta_x = \frac{\lambda \cdot f}{s_h}. \quad (2.9)$$

2.3.3 Angular spectrum propagation

The angular spectrum propagation is used in this work because it is the least computationally costly algorithm capable of short distance propagation, as it can be implemented with two Fast Fourier Transforms (FFT). Its limitations are the scalar diffraction approximation and a maximum propagation distance, discussed later in this section. The AS propagation will be used in section 4.3 for calculation of the holograms for the projection of 3D patterns. It approximates the light field as the interference of a large number of plane waves with different propagation directions and amplitudes. The spectral representation of the wave in a plane

$z = z_1$ relates with the spectral representation of the wave in plane $z = z_0$ by the propagator in reciprocal space \hat{H} that can also be described as the Fourier transform of the response function of free space, equivalent to the field at z caused by a point source at $z = z_0$.

The angular spectrum propagation integral with complex amplitude in the source plane A and in the target plane U can be formulated for implementation on a computer as

$$U(x, y, z_1) = \mathcal{F}^{-1} \left\{ \mathcal{F} [A(x', y', z_0)] \cdot \hat{H}(u, v) \right\} \quad (2.10)$$

with the Fourier transform \mathcal{F} , the spatial coordinates x, y, x', y' , the propagation distance $z_p = z_1 - z_0$, the spatial frequency coordinates u, v and the propagator

$$\hat{H}(u, v) = \exp \left(i \frac{2\pi z_p}{\lambda} \sqrt{1 - u^2 \lambda^2 - v^2 \lambda^2} \right). \quad (2.11)$$

For numerical implementation of the AS method, a spatial sampling of the light field is necessary. The source plane, target plane, and the angular spectrum all have the same pixel array size. This limits the validity of the method to propagation distances

$$z_p \leq \frac{M_x \Delta_x^2}{\lambda} \sqrt{1 - \frac{\lambda^2}{4\Delta_x^2}} \quad (2.12)$$

with λ wavelength, M number of sampling points, Δ_x distance of sampling points [18, 19].

If the method is implemented using FFT, aliasing will occur at larger distances due to the implied periodic boundary conditions of the FFT, decreasing the accuracy drastically. Eq. (2.12) shows that a larger number of sampling points allows for larger propagation distances, thus a zero padding of the source plane can increase the validity region of the method, however the greatly increased computational cost restricts its usage. Recent efforts attempt to extend the validity region, for example by limiting the spectrum with a filter [20], by extending the available spectrum with resampling [21], or by calculating the minimum necessary zero padding and evaluation of only nonzero sampling points [22].

2.3.4 Overview of propagation algorithms

The choice of a suitable propagation algorithm depends on the application and therefore on the following relevant parameters: wavelength λ , spatial sampling Δ_x , propagation distance, feature size, source phase profile $\phi(x, y)$ and other factors, such as whether a focusing or defocusing effect occurs.

The Rayleigh-Sommerfeld (RS) diffraction integral when solved by direct integration can solve the Helmholtz equation without further approximations. However, the implementation of this algorithm on a computer is computationally expensive. To reduce the computational load, the lower computational complexity of the Fast Fourier Transform (FFT) was utilized to implement the integration [23].

To formulate a propagation algorithm with decreased computational cost, depending on the application, further approximations can be used, an overview is given in Table 2.1, the commonly used algorithms are usually implemented with FFT to reduce computational load. The least computationally expensive propagation algorithms are the near-field propagation

with Fresnel approximation and the far-field propagation with Fraunhofer approximation, which both require the paraxial approximation and can both be calculated with a single FFT and a multiplication with a phase term.

Table 2.1: Overview of propagation algorithms - An overview comparison of common propagation algorithms, the approximations used, the validity range if applicable, and the scaling of computational cost in terms of the number of FFTs necessary for implementation on a computer [20, 23]. It is noted that there are more implementations based the Fresnel- and Rayleigh-Sommerfeld diffraction integrals that are not included here. Also, any near field propagation is often called 'Fresnel propagation', regardless of the propagation algorithm used.

Method	computational cost	paraxial only	near field only	far field only
Rayleigh-Sommerfeld (RS) direct integration	3FFT			
angular spectrum (AS) propagation	2FFT		X	
Fresnel propagation	1FFT	X		
Fraunhofer propagation	1FFT	X		X

2.3.5 Spatial sampling

For implementation of propagation algorithms on a computer, as with any digital signal processing, sampling intervals must be chosen carefully, so the resulting digital representation adequately represents the actual signal. In case the sampling intervals are too large, aliasing may occur due to the Nyquist-Shannon sampling theorem being violated [13]. While the sampling theorem is commonly used for time domain sampling, it is equally valid for spatial domain sampling: The spatial sampling rate has to be at least two times higher than the highest spatial frequencies in the system. Furthermore, many propagation algorithms use multiplication or convolution with an additional term that may contain high spatial frequencies, for example in Fresnel propagation a quadratic phase term is present in the diffraction integral, which further increases the required number of samples [13].

When propagation algorithms are implemented on a computer, the pixel count resulting from the spatial discretization of the light fields has a very large effect on the computational load, therefore it is of interest to determine the minimum sampling rate for achieving the desired calculation accuracy. This is especially important for iterative hologram calculation algorithms, described in section 2.4, which potentially have to perform a large number of propagation calculations.

An inadequate choice of the sampling interval can lead to propagation errors even for the RS propagation [24]. The sampling intervals in both the source plane and target plane has to fulfill the requirements, however the sampling interval in the target plane depends on the propagation algorithm, the source plane sampling, and for some algorithms also on the propagation distance. Thus, determining the correct choice of the sampling interval can require considerable effort. Fig. 2.6 shows the effect of spatial discretization on an example source field.

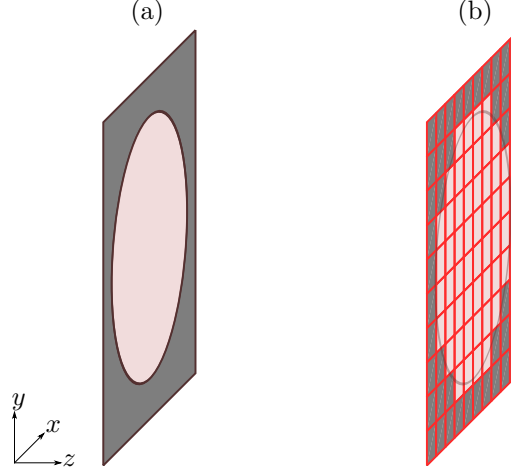


Figure 2.6: Effect of spatial discretization: (a) circular aperture; (b) circular aperture when discretized; z , propagation direction; x, y , transversal plane coordinates.

2.4 Hologram calculation methods and considerations

This section describes hologram calculation methods, their structure and variations. First the general parameters are introduced. Then, an overview of hologram calculation methods is given to give context on the choice of hologram calculation algorithms for this work. Finally, the two methods iterative Fourier transform algorithm (IFTA) and error diffusion (ED) algorithm that are primarily used in this work are described in more detail.

Table 2.2 gives an overview on the important parameters of CGHs which are relevant for the choice of a hologram calculation method.

Table 2.2: Parameters for categorization of common computer generated holograms
- Overview on the most important input parameters for calculation of CGHs.

Propagation method:	near field	far field
Modulation:	phase	amplitude
Projection phase:	constrained	unconstrained
Degrees of freedom projection:	# of sampling points	# of intensity levels
Degrees of freedom hologram:	# of pixels	binary/multilevel

Evaluation of hologram calculation methods is commonly done with three target parameters

- projection quality
- diffraction efficiency
- computational cost

whereas their definition and weighting depends on the application. The three target parameters are conflicting, so in most cases, a trade off is necessary.

However, the technology used to create the hologram also has to be taken into account, since it puts boundaries on pixel size and pixel count (total number of pixels, commonly arranged on a rectangular grid), also called space-bandwidth product (SBP) [13]. The phase or amplitude quantization of the holographic optical element (number of available phase/amplitude levels, limited by the technology) has to be considered as well, for example the optimization of

a binary phase hologram differs greatly from the optimization of a quasi-continuous phase hologram with hundreds of available phase levels. The influence of pixel count, pixel size, and number of phase levels is discussed in more detail in chapter 2.5.

A propagation algorithm is necessary for hologram calculation: In general, holograms are categorized in Fresnel holograms (near field), and Fourier holograms (far field). The choice of an appropriate propagation method is substantial for hologram calculation due to the different approximations that can be made which have a large influence on calculation time and resulting projection quality, this is elaborated in section 2.3.4. Further, each propagation algorithm has multiple input parameters which can also greatly influence the calculation time and resulting quality. Thus, a hologram calculation algorithm can only be evaluated in conjunction with the available degrees of freedom given by the physical implementation method of the hologram and the propagation algorithm used with its parameters.

2.4.1 Overview of hologram calculation algorithms

In addition to the error diffusion and iterative Fourier transform algorithm that are used in this work, this subsection gives an overview of further hologram calculation methods from literature.

Direct binary search algorithm

The direct binary search (DBS) algorithm [25, 26] has originally been designed to calculate binary Fourier amplitude holograms. It operates by scanning the hologram pixelwise, switching the phase value, propagating to the target plane and evaluating the error function. If the error is decreased, the new pixel value is kept, if it is increased, the pixel is reverted to its original value. Simulated annealing can be used to prevent convergence to local minima. Variations include the usage of near field propagation [27], or calculation of multi-level phase holograms [28]. The quality of the calculated holograms can be very good but computational complexity is extremely high, especially for holograms with high pixel count and multi-level holograms. The gradient-descent direct search [29] was introduced to decrease the computational load for holograms for a high number of phase levels.

Optimum rotation angle algorithm

The optimal-rotation-angle (ORA) [30] algorithm works similarly to the DBS algorithm, first Fourier transforming the initial hologram phase distribution, calculating the target complex amplitude. It is then scanning the hologram pixelwise, but is using the geometrical optical relations from the hologram pixel to all target pixels, optimizing the phase value of the hologram pixel so that the target complex amplitude distribution approaches the desired values. After scanning all hologram pixels, the next iteration is started: The new target complex amplitude distribution is calculated with Fourier transform and the hologram is again scanned pixelwise. A few hundred iterations are typically used.

Analytic calculation

The very computationally costly hologram calculation is not required for many applications of diffractive phase elements. When an analytic calculation of the propagation from hologram to target is available, or the calculation can be simplified significantly, a much faster calculation of the light fields with diffractive optical elements (DOE) is possible.

As a simple example, for generation of focal spot the phase function of a lens can be calculated directly and quantized if necessary instead of a time consuming hologram calculation. For diffractive beam splitters, gratings with equal efficiencies can also be calculated as Dammann gratings [31]. For the design of diffractive lenses as Fresnel zone plates, calculations can also be simplified considerably [32].

2.4.2 Iterative Fourier transform algorithm

The iterative Fourier transform algorithm (IFTA) was demonstrated by Gerchberg and Saxton [33] as a method of phase retrieval from two measured Fourier-conjugated intensity images. This algorithm can iteratively come to a solution for the inverse problem of unknown phase in two planes transversal to propagation if the intensities in both planes are known. The method is the same for calculation of phase-only holograms, only the intensities are not measured but defined as input requirements for the algorithm. This method can be used to calculate holograms in the Fourier [34] and Fresnel [35] regime.

The basic working principle is:

1. Set the phase of the projection to an appropriate starting distribution
2. Set the projection amplitude to the target amplitude
3. Calculate the hologram wavefront with Fourier transform
4. Set the hologram amplitude to a constant value (in case of uniform illumination) and keep the phase
5. Calculate the target wavefront with inverse Fourier transform, return to 2.

The algorithm may evaluate the difference between target and actual intensity and stop if it is below a certain threshold or run for a predetermined number of iterations. It is illustrated in Fig. 2.7.

Based on this principle, a large number of modified algorithms has been suggested [36–40]; an overview for beam shaping applications can be found in Ripoll et al. [41]. The modifications aim to increase efficiency and/or uniformity, reduce speckle contrast or to optimize the result for a specific application and/or hologram manufacturing method.

2.4.3 Error diffusion algorithm

The error diffusion (ED) algorithm is a recursive algorithm for down-conversion of pixelized information to a lower number of discretized height levels, used initially for image compression [42]. The algorithm has also been adapted for calculation of multi-level phase-only holograms [43] and for calculation of binary phase holograms [44]. Phase-only holograms are generated

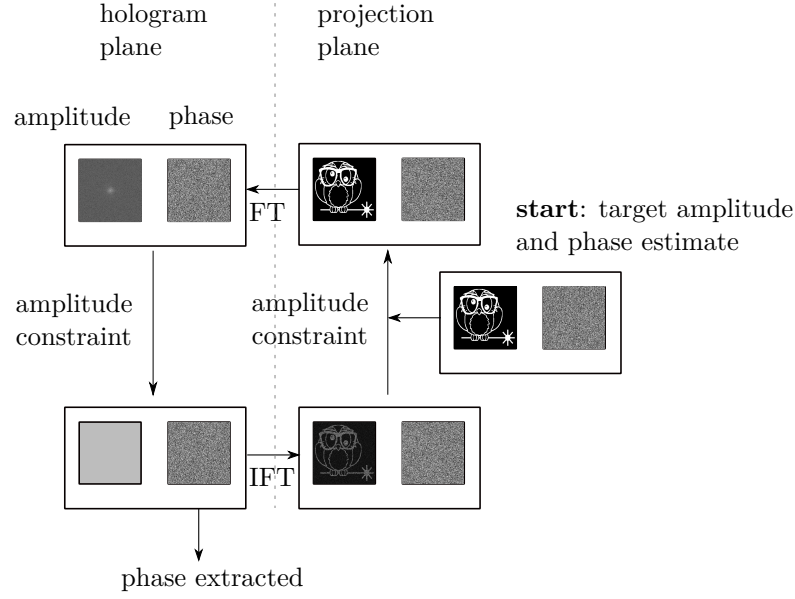


Figure 2.7: Schematic of the IFTA - The iterative Fourier transform algorithm constrains the amplitude of the hologram and the projection in every iteration. The phase is a free parameter, allowing the convergence of the algorithm. FT, Fourier transform. IFT, inverse Fourier transform.

by input of the complex hologram wavefront and discretization of the amplitude to a constant level, then distributing the complex error into neighboring pixels.

The important input parameters are

- the image or array to be processed,
- the number and magnitude of output levels to be discretized to,
- the scanning method, and
- the coefficients used for diffusion of the error into neighboring pixels.

As visualized in Fig. 2.8, in ED an image (or rasterized complex wavefront) is scanned line by line and pixel by pixel, discretizing the pixel value to the nearest available level, then calculating the error caused by the discretization

$$q(m, n) = a(m, n) - b(m, n) \quad (2.13)$$

with q error, a original pixel value, b discretized pixel value, and m, n pixel coordinates. Then the error is diffused into neighboring unprocessed pixels according to the weighing coefficients.

$$a(m+1, n) = a(m+1, n) + 7/16 \cdot q(m, n) \quad (2.14)$$

$$a(m+1, n+1) = a(m+1, n+1) + 1/16 \cdot q(m, n) \quad (2.15)$$

$$a(m, n+1) = a(m, n+1) + 5/16 \cdot q(m, n) \quad (2.16)$$

$$a(m-1, n+1) = a(m-1, n+1) + 3/16 \cdot q(m, n) \quad (2.17)$$

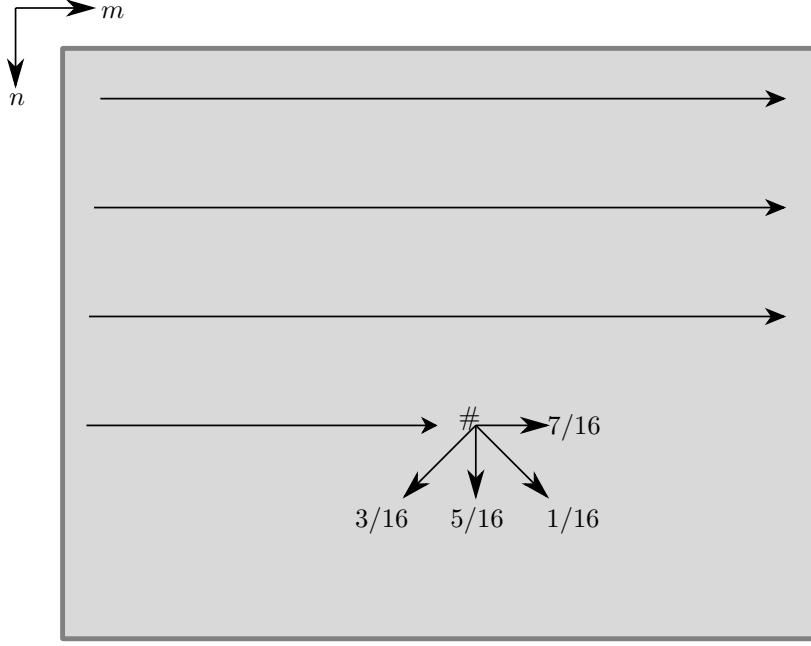


Figure 2.8: Schematic of error diffusion algorithm - A pixelized image (grey) is scanned line by line, each pixel is discretized and then the discretization error is distributed into neighboring unprocessed pixels according to the weighing coefficients. '#' : pixel to be processed.

The standard coefficients used for weighing the diffusion are the Floyd-Steinberg error diffusion coefficients [42]

$$\frac{1}{16} \begin{bmatrix} - & \# & 7 \\ 3 & 5 & 1 \end{bmatrix} \quad (2.18)$$

with # the pixel to be processed. Other coefficients have been investigated [44, 45], but have minor influence on the projection quality of quasi-continuous phase holograms that are used in this work. The algorithm can also be integrated into other hologram calculation algorithms [46, 47]. In Chapter 4 it is used for converseion of complex holograms into phase-only holograms. To increase efficiency, they are then used as an initial phase distribution for an iterative hologram calculation algorithm.

2.4.4 The noise problem in CGH: Speckle reduction

In many common hologram calculation algorithms the phase distribution of the target pattern is not controlled. This random phase distribution then causes random interference of neighboring sampling points and can also cause phase vortices which have zero intensity in their center. The additional contrast caused by this is called speckle. The speckle contrast is a main source of decreased projection quality, as shown in Fig. 2.9 (a) and (b).

In projector applications additional speckle contrast can be caused by a scattering screen. Speckle contrast can be reduced by using a light source with lower temporal and spatial coherence than a laser, such as a light emitting diode (LED) [48, 49]. However, in holographic projection the reduced temporal and spatial coherence of an LED causes an increase of image blur [49], making this approach unsuitable for projection of intricate patterns with clearly defined edges. Another approach uses an echelon (staircase-like structure) to increase the

optical path difference of beam sections beyond the coherence length of a laser diode and then uses a static diffuser to mix the beam sections [50].

Temporal averaging is another option to reduce speckle contrast, whereby a large number of differently speckled patterns is incident on the observer/sensor during its integration time. Temporal averaging is often done using a moving diffuser, which has been implemented for laser projectors [51, 52], or for observation of fast processes in microscopy [53]. Its usage has also been attempted in holographic pattern projection [54], however the method also decreases the spatial coherence, leading to blurred edges in the projected image. When a dynamic display of holograms is possible (e.g. when a SLM is used), and the switching frequency of the hologram display is faster than necessary for the application, temporal averaging of uncorrelated or negatively correlated holograms can be used to decrease speckle contrast [55–60].

Another option to reduce speckle contrast is to obtain full control of both amplitude and phase of the projection by complex modulation of phase and amplitude of the hologram. However, currently no device is capable of independent modulation of phase and amplitude, so an elaborate and sensitive optical setup with multiple modulation areas is required [61].

There are also ways to achieve reduction of speckle within the hologram calculation algorithm, commonly by implementing some restriction of the target phase to prevent phase vortices. It is noted that this significantly reduces the degrees of freedom for the hologram calculation and due to the limited SBP of holograms, reduction of diffraction efficiency and/or number of addressable target pixels. The double constraint Gerchberg-Saxton algorithm (GSA) [37, 62] which restricts the amplitude and phase distribution of the target pattern was developed. This decreases the degrees of freedom for the hologram calculation, so a noise window around the target pattern with unrestricted phase and amplitude is necessary, see Fig. 2.9 (c).

To illuminate an object larger than the hologram or for far field projection, redistribution of light without usage of random phase as a diffuser is required. For this, a defocusing lens phase can be used, implemented in the paraxial approximation as a quadratic phase distribution. Due to this controlled quadratic phase distribution of the projection, no random phase interference or phase vortices can occur. [63] among others calculate a quadratic phase distribution by including the optical setup parameters in the calculation. The specific quadratic phase distribution then ensures that the hologram fully illuminates the projection without requiring a random phase distribution. This method will be applied and its variations analyzed in detail in section 4.1 for speckle reduced hologram calculation.

2.4.5 Hologram calculation for 3D projections

For projection of a pattern that does not completely coincide with a plane orthogonal to the optical axis, modifications to the common hologram calculation methods described in Chapter 2.4 are required. An overview of common methods is given in Fig. 2.10. Multi-plane propagation [9, 35, 37, 58, 64–66] is a commonly used method because of the flexibility and relative ease of integration into hologram calculation methods, however the additional constraints in more planes may decrease projection quality and for stitching of continuous patterns in multiple planes for projection on a nonplanar surface, the distance between the planes must be carefully chosen [9].

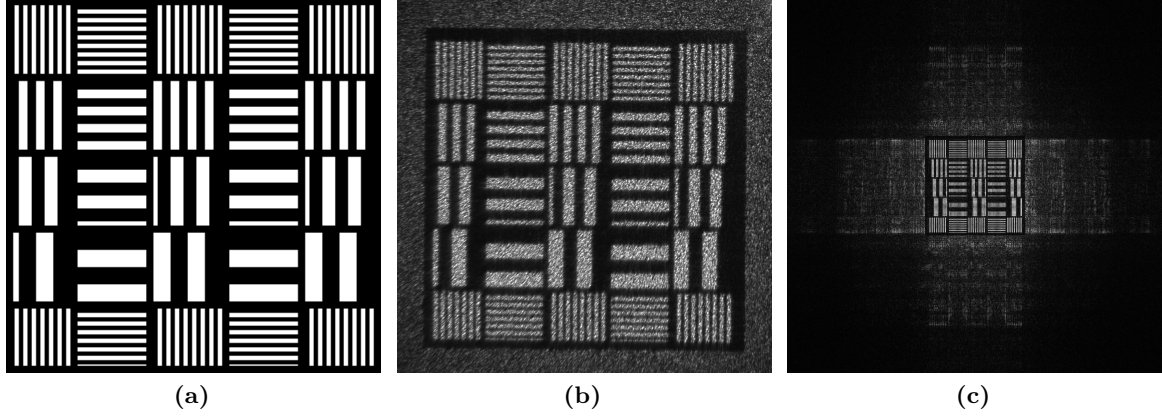


Figure 2.9: Example for speckle contrast and noise window for double constraint GSA - (a) target projection pattern; (b) speckled projection caused by random phase interference; (c) noise window in double constraint GSA.

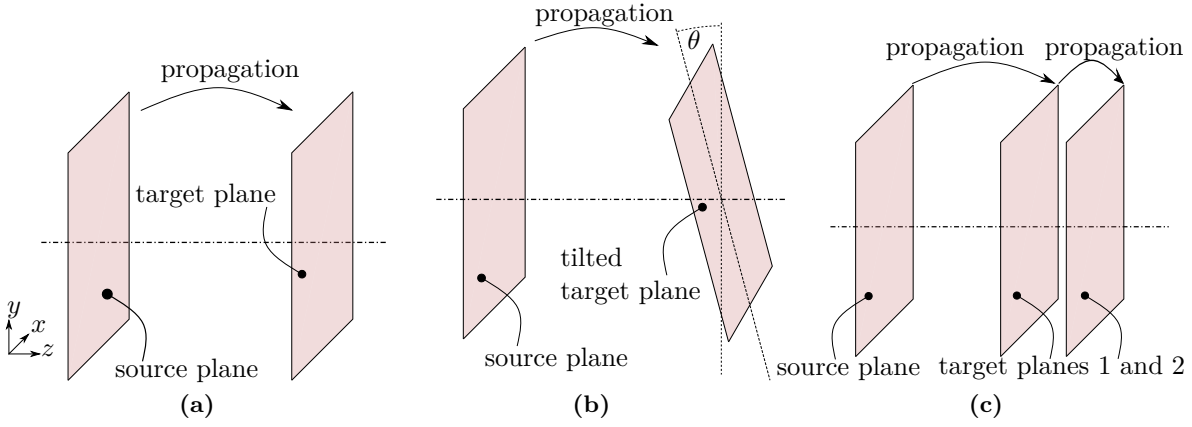


Figure 2.10: Schematic of hologram calculation for 2D and 3D projections - (a) Standard 2D hologram calculation, (b) Tilted plane hologram calculation, (c) Multi-plane hologram calculation.

As an overview into further methods for calculation of 3D holograms, two categories are established: Projection on a surface and projection in a volume. For the former, looking from the hologram no projection areas are obstructed by other projections. For the latter, obstructions may occur.

1. In surface projection, the target plane is tilted/distorted or a projection to multiple planes with spatial separation of the signals in the different planes is used. The tilted plane propagation [67–70] can be used to adapt a hologram calculation method for projection on a plane tilted with respect to the plane orthogonal to the optical axis. The algorithm described in [71] was designed for projection of a pattern on a spherical surface.
2. In volumetric projection, a target volume is considered as the target for projection, for example with a 3D Gerchberg-Saxton algorithm [72] or by using interference of three orthogonal beams [10].

In the following, the focus is on multi-plane 3D projection, since it is most suitable for projections on differently shaped surfaces, while the other previously mentioned methods are more restricted to certain special surface shapes.

Multiple approaches to multi-plane 3D projection have been published. The global 3D GSA consists of iterations of

- parallel propagation to the target planes,
- restriction of amplitude (sometimes also phase),
- backpropagation from all planes to hologram,
- addition of all complex amplitudes,

then conversion to phase-only hologram. It is described e.g. in [65] for Fourier holograms and [37] for Fresnel holograms with phase restriction. Zhang et al. [73] provided an overview of 3D Gerchberg-Saxton algorithms.

The double-constraint 3D Gerchberg-Saxton algorithms uses the wavefront information from multiple planes to calculate the complex amplitude in one plane, then calculate the hologram to reconstruct this complex amplitude. Implementations may sum up the complex amplitude in one plane, then iteratively construct the hologram [74], or iteratively reconstruct the complex amplitude in one plane, then calculate the hologram [35].

2.5 Physical realization of computer generated holograms

This section serves as an overview of the methods available for physical realization of CGH. Two categories are presented. Static holograms are manufactured once and then used for an application. On the other hand, the dynamic hologram display allows for a quick, flexible and immediate way for usage of different holograms.

2.5.1 Technologies for manufacturing of computer generated holograms

Although this work focuses on dynamic holographic projection, an overview of the manufacturing methods for static phase holograms is given in this section. For manufacturing of static holograms by changing the surface topography of a material, technologies that allow for high spatial resolution and a minimum of 2π phase difference can be used, e.g.

- diamond turning,
- laser ablation, or
- lithography.

Generally, the smaller the structures, the larger the diffraction angles that can be achieved. The grating equation for light incident orthogonally on a structure is

$$\sin(\theta) = m \cdot \frac{\lambda}{\Lambda} \quad (2.19)$$

with θ diffraction angle, m diffraction order, λ wavelength of light, and Λ periodicity of the diffracting structure. Smaller structure sizes allow smaller Λ and thus larger diffraction angles θ .

For CGHs made from quartz glass and visible light applications, relatively small surface heights

$$\frac{\lambda}{(n_{\text{material}} - 1)} = \frac{700\text{nm}}{(1.45 - 1)} \approx 1.5\mu\text{m} \quad (2.20)$$

are required to achieve phase wrapping with 2π phase modulation, thus lithographic manufacturing methods are commonly used because these can achieve such surface heights with good tolerances.

2.5.2 Technologies for dynamic display of computer generated holograms

This section gives an overview of hologram display device technology and the critical parameters, which is important for the correct choice of a device for a given application. In general, the dynamic display of a CGH has limitations that are imposed by the device that is used, the most important parameters are

- pixel size,
- pixel count, also called space-bandwidth product (SBP),
- available number of phase / amplitude levels, and
- operating speed.

These parameters define the degrees of freedom of the light distribution shaped by the hologram. The fill factor is an additional parameter that limits the efficiency of the displayed holograms. The projection quality may decrease caused by tolerances, imperfect pixel shape, or temporal fluctuations. For the LCoS technology, these effects are discussed in more detail in section 3.2. Table 2.3 compares the main technologies available for dynamic hologram display. It is noted that for display of holograms, the digital micromirror device (DMD) technology is restricted to binary amplitude modulation. Furthermore, LCD are transmissive devices, while LCoS and DMD are reflective devices.

Table 2.3: Overview of technology for dynamic display of holograms - Shows the best values achieved with commercial devices (note that no single device achieves all these values, for example the wavelength range for one device is always smaller than the full wavelength range achievable with the technology), as of 2020. MP, Megapixel; DMD, digital micromirror display; LCD, liquid crystal display; LCoS, liquid crystal on silicon. [75–81]

Technology:	LCoS	LCD	DMD
pixel pitch (down to):	3.74 μm	36 μm	5.4 μm
operating speed (up to):	360Hz	60Hz	>10kHz
fill factor (up to):	96%	58%	93%
pixel count (up to):	8MP	0.8MP	4MP
wavelength (down to):	350nm	450nm	355nm
wavelength (up to):	1700nm	800nm	2500nm

2.6 Summary of Chapter 2

In this chapter, an overview of the aspects of holography-based lithography and related methods is given. Then, computer generated holography is described, and its key aspects, which are propagation algorithms, hologram calculation algorithms, and the physical implementation of holograms.

For propagation algorithms, their properties, approximations, and limitations for implementation on a computer are described. For the fundamentals of hologram calculation, first the input and target parameters are laid out, an overview of methods is given and also speckle problem and 3D projection algorithms are described. Finally, technologies for physical realization of holograms are described, whereas static and dynamic holograms are differentiated.

To conclude, this chapter introduces the main motivation for this work (parallelized maskless holographic lithography) and also CGH as the main tool used. It also includes fundamentals on the important aspects of CGH.

3

LCoS technology aspects for holographic projection

For the dynamic display of CGHs, the competing technologies are LCoS, DMD, and LCD, as outlined in section 2.5. LCoS is chosen as the SLM technology because of the high space-bandwidth product (SBP), the large number of 255 available phase levels for quasi-continuous phase modulation, the sufficient switching frequency at around 60Hz for standard devices and the small pixel size. However, a number of effects associated with LCoS based phase modulation can occur, which have to be considered to achieve adequate device performance.

In this section, the basic technological structure of LCoS and the working principle of parallel aligned nematic (PAN) LCoS to realize phase modulation are described. The various technological effects that can be detrimental to the quality of displayed holograms are listed and explained. Compensation of the effects may be necessary depending on the requirements of the application and the quality of the LCoS device in use. Furthermore, the steps required for the characterization and calibration of the LCoS used in this work are described.

3.1 LCoS technology

The liquid crystal on silicon spatial light modulators (LCoS-SLMs) are built similar to LCD technology, but the liquid crystal layer is placed on a reflective surface. This allows for smaller pixels and a much larger fill factor, since the electronics for pixel control can be placed behind the reflective surface. Light passes the liquid crystal layer twice, which doubles the maximum phase shift. The liquid crystal layer is sandwiched between two alignment layers which define the liquid crystal molecule orientation while no voltage is applied, see Fig. 3.1. The orientation of the alignment layers define the LC cell structure.

Different types of LC cell orientation and driving schemes are used in LCoS devices, however most are less suitable for phase-only modulation, for example, the twisted nematic orientation always causes a polarization rotation, and ferroelectric LCoS are limited to binary phase modulation. A comprehensive overview on the LCoS technology for phase modulation

and its various implementations can be found in [82] and in particular the effect of different LC layer orientations are detailed in [83].

For phase-only modulation, the parallel aligned nematic (PAN) liquid crystal configuration is commonly used, also called zero-twist configuration. The alignment layer structure acts like a boundary condition, so the LC molecules nearby align their orientation parallel to each other, causing the molecules inbetween to align as well. This results in an electrically controlled birefringence (ECB) effect of the liquid crystal (LC) layer, allowing for phase-only light modulation for linearly polarized input light, Fig. 3.2 details the effect. The liquid crystal molecules have different refractive indices along their axes. With voltage applied to a pixelized electrode, the liquid crystal molecules rotate, changing the effective refractive index of the liquid crystal layer locally, therefore modulating the phase of the reflected light. Further processing steps can be made at the cover glass and pixelized electrode to increase the reflectivity.

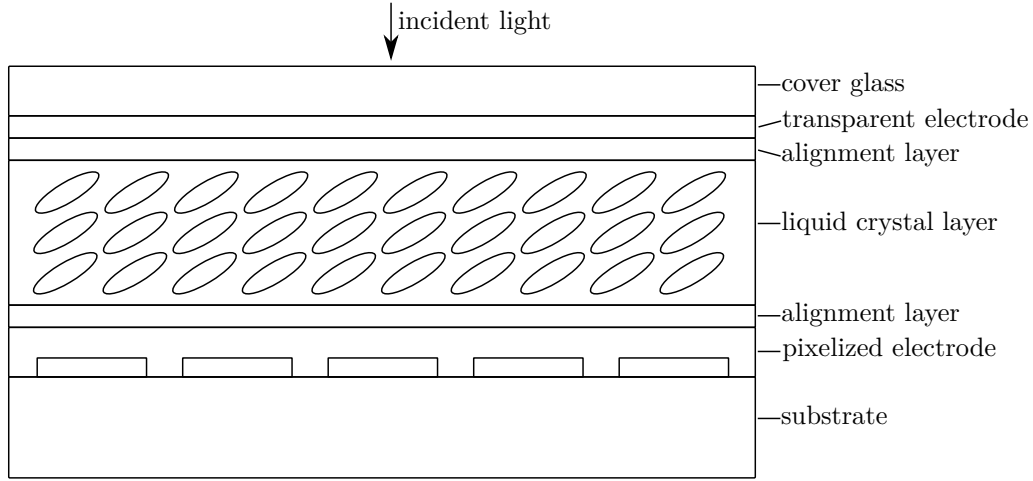


Figure 3.1: Simplified LCoS structure

3.2 Fundamental LCoS phase effects

The following effects occur in hologram display with a LCoS that may degrade projection quality, each one will be explained in this section.

- Pixel crosstalk
- Zero order light
- Spatially varying phase response
- Flicker
- Aberrations from LCoS backplane
- Spatial frequency response
- Tilt angle dependency

It is noted that zero order light and spatial frequency response are present in all methods of CGH physical representation.

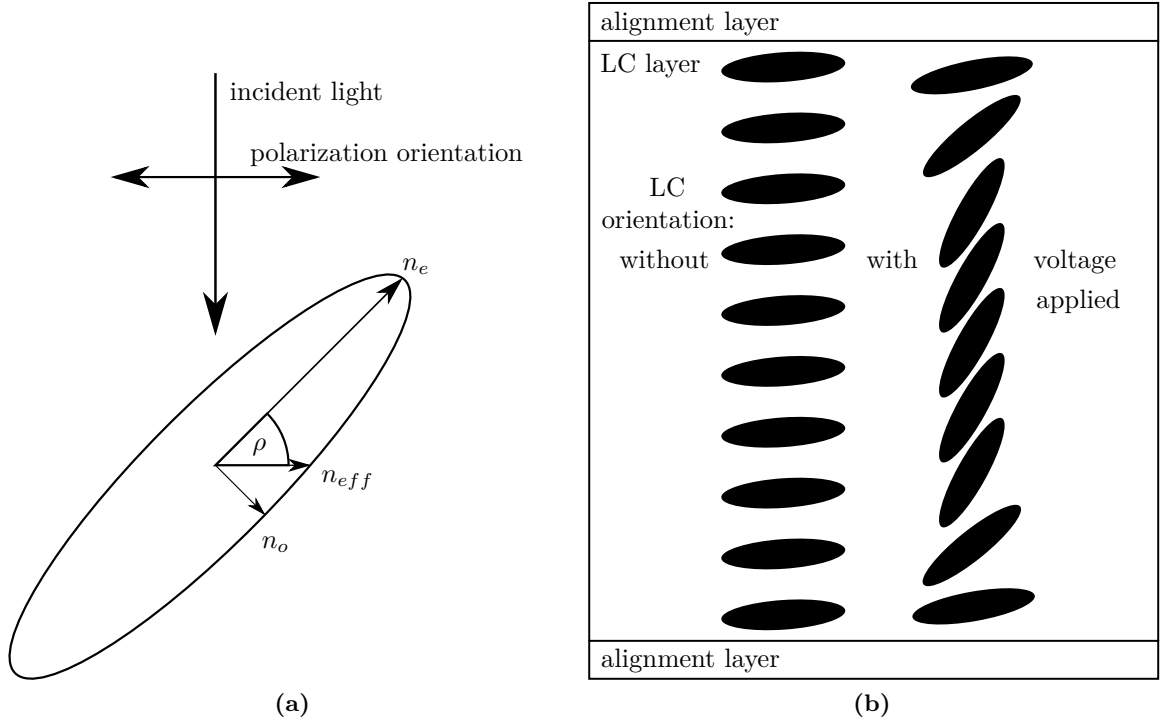


Figure 3.2: Phase modulation with liquid crystals - (a) ordinary n_o and extraordinary n_e refractive indices of a liquid crystal, the incident polarized light sees n_{eff} when the liquid crystal is rotated by ρ ; (b) liquid crystal configuration in PAN devices, left: without voltage applied, $n_{eff} \approx n_e$ right: with voltage applied, $n_{eff} \approx n_o$.

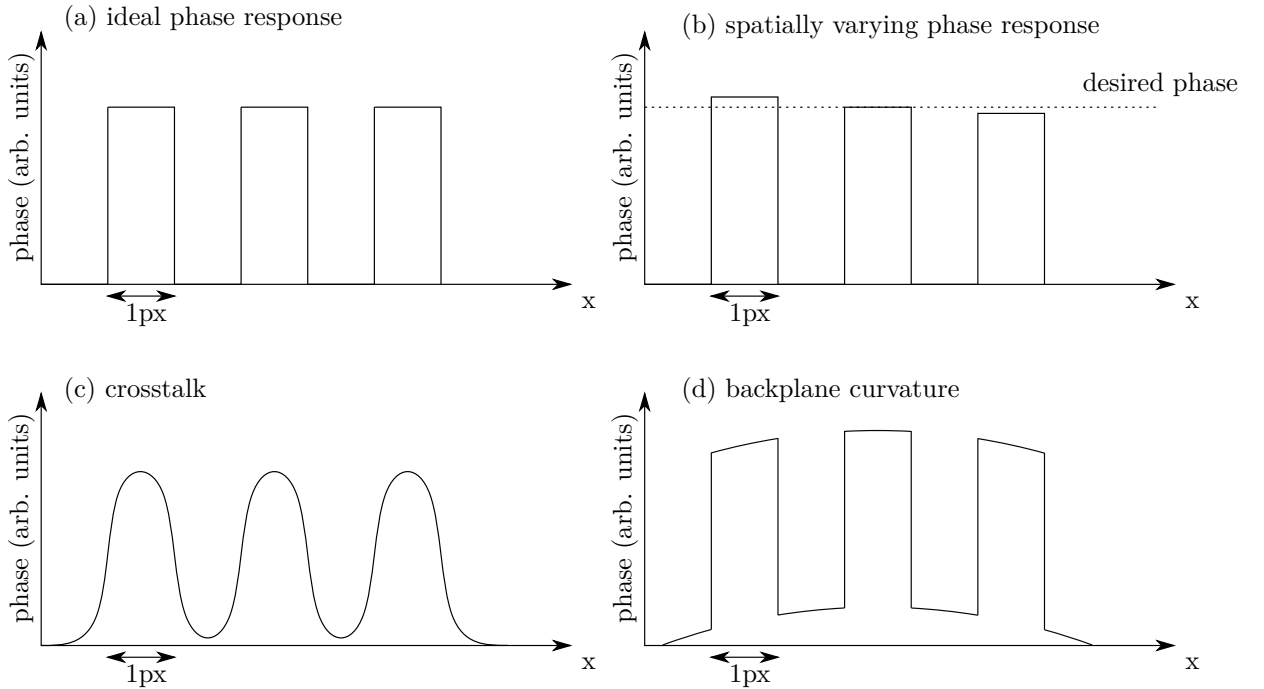


Figure 3.3: LCoS time invariant phase imperfections - Effects are differently pronounced for different LCoS models. (a) ideal phase response, (b) spatially varying phase response, (c) pixel crosstalk effect: phase modulation is affected by neighboring pixels, (d) backplane curvature effect.

3.2.1 Pixel crosstalk

The effect that significant pixel crosstalk can have on first order diffraction efficiency and zero order intensity has been measured and methods were proposed for compensation of the effect

[84, 85]. Whether compensation of this effect is required depends on the LCoS model, its calibration, and the requirements of the application. Generally, the effect is more pronounced the smaller the LCoS pixels and the larger the voltage differences of neighboring pixels are. Fig. 3.3 (c) shows the resulting phase response of a displayed binary grating when strong crosstalk is present.

3.2.2 Unmodulated zero order light

LCoS devices typically have a cover glass that also reflects light. Additionally, some light is reflected unmodulated due to the limited fill factor of the devices, which is typically around 90...95%. Both effects result in a zero order beam which manifests as a bright spot when displaying Fourier holograms, see Fig. 3.4. The intensity of the zero order beam is also influenced by the phase distribution displayed on the LCoS, measured in Fig. 3.9. Compensation of this effect can be achieved by shifting the hologram along the x, y and/or

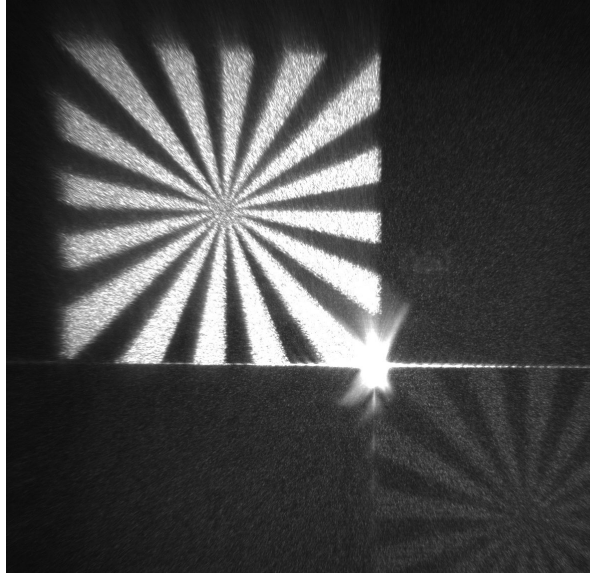


Figure 3.4: Projection of Siemens star with zero order spot - The bright spot is the zero order light, the decreasing projection intensity with increased distance to the zero order can be observed.

z axis with the addition of a blazed phase or lens phase [86]. This spatially separates the projection from the zero order beam, which can then be filtered by an aperture. Alternatively, a central spot can be iteratively designed in phase and amplitude to destructively interfere with the zero order spot [87]. It is noted that this iterative process of measuring the zero order intensity and correcting it would be required for every hologram to be displayed because the zero order intensity is not constant due to the pixel crosstalk effect.

3.2.3 Spatially varying phase response

LCoS devices have a spatially varying phase response, caused by an uneven thickness of the liquid crystal layer. In some devices this effect is significant, meaning that a calibration of the phase response has to be conducted for multiple smaller sections of the display [88–91] to achieve satisfactory device performance. The effect is illustrated in Fig. 3.3 (b). The section

with the smallest maximum phase retardance then limits the usage of the device, because for projection with CGHs a minimum of 2π phase retardance has to be achieved for the wavelength in use to allow phase wrapping, see section 2.2.2.

3.2.4 Flicker

Most LCoS displays are equipped with digital voltage control. This includes a high frequency carrier signal which commonly leads to a high frequency flicker of the phase response [92], Fig. 3.5 shows a schematic visualization. The amplitude of the phase flicker depends on the voltage levels used for calibration, the currently displayed phase value and on the temperature of the LCoS display [93].

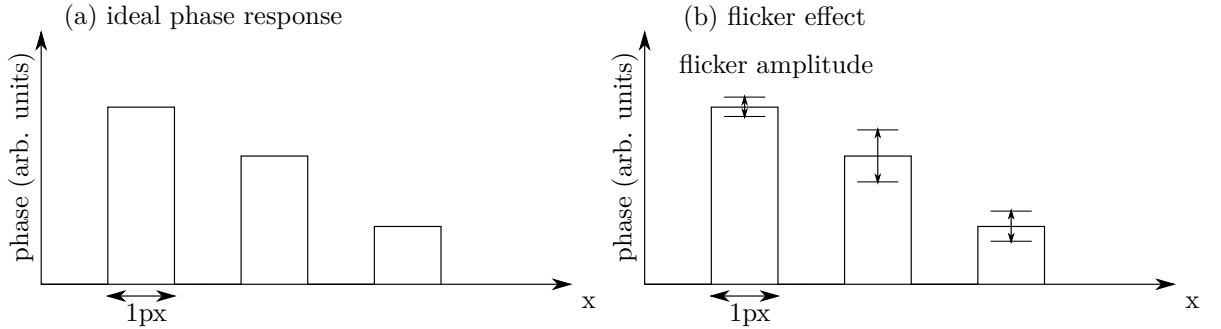


Figure 3.5: Schematic of LCoS flicker effect - The flicker amplitude depends on the displayed phase value. (a) ideal phase response, (b) corresponding exemplary flicker amplitude.

3.2.5 Aberrations caused by backplane curvature

Caused by the manufacturing process, the reflecting backplane of the LCoS-SLM usually is curved to some degree. The effect on the phase modulation for a backplane with constant curvature is illustrated in Fig. 3.3 (d). This effect induces some aberrations to the reflected light which can be compensated for the wavelength in use by measuring the aberrations and calculating a phasemap to compensate for them. This phasemap is then added to the holograms or diffractive elements displayed on the LCoS. Aside from standard wavefront measurement setups, such as interferometry and Shack-Hartmann sensors, it is also possible to use the phase modulation of the LCoS-SLM to measure the wavefront, for example by displaying the phase of micro lenses [94] or by phase shifting the interference pattern caused by cover glass reflections and backplane reflections [95].

3.2.6 Spatial frequency response

A sinc^2 shaped intensity modulation is present for all methods for display/manufacturing of far field CGHs and is related to the pixel size. For the display of Fourier holograms, the maximum off-axis intensity is multiplied by a 2D sinc^2 function (the Fourier transform of the pixel size and shape) [96, 97]. Compensation of the effect can be included in the hologram design by calculating the parameters of the sinc^2 function, then multiplying the target intensity distribution with the inverted sinc^2 function, this is described in more detail in section 5.2. Doing so slightly reduces the diffraction efficiency [96].

3.2.7 Tilt angle dependency

The reflective nature of the LCoS requires additional effort for the separation of incident and reflected light. One method is the usage of a 50:50 beam splitter as in Fig. 3.6 (a), which reduces the light intensity by 75% (using a polarizing beam splitter and a $\lambda/4$ plate is not possible since only linear polarized light is modulated by the LCoS). The alternative is tilting the LCoS along the x - or y -axis to separate the incident and reflected light, see Fig. 3.6 (b). While this can affect the device performance, it has been reported that an angle of 3° for a parallel aligned nematic LCoS [92] and 10° for a twisted nematic LCoS [98] is not significantly detrimental to the phase modulation performance.

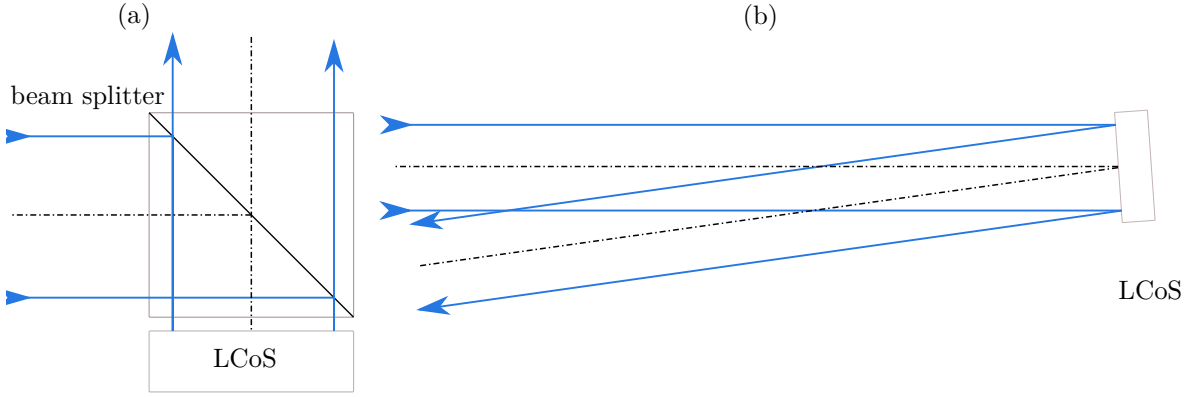


Figure 3.6: Incorporation of LCoS in optical setups - (a) with and (b) without beam splitter.

3.3 LCoS-SLM characterization and calibration

The phase-only model "Holoeye Pluto-2-VIS-016" has 1920×1080 pixels, a pixel size of $8\mu\text{m}$, and is capable of displaying 256 different phase levels with a maximum phase retardance exceeding 2π at 633nm. This section describes the steps taken to calibrate and characterize the LCoS for the desired lithographic application, which are the phase response calibration, the pixel crosstalk measurement, and the backplane aberration measurement and correction.

3.3.1 Phase response calibration

Calibration of the SLM to achieve a linear phase shift from zero to 2π for the wavelength in use is done with a two-beam interference setup [99].

In this setup, two parallel planar beams from the two halves of the LCoS display are focused on one spot with a lens, creating an interference pattern which is then magnified and imaged on a camera sensor, see Fig. 3.7 (a).

A cross section of the interference pattern on the camera sensor is displayed in Fig. 3.7 (b). The overexposure is not a problem here because only the periodicity of the pattern is needed. Then the driving voltage for one half of the display is changed in small steps and the resulting shifted interference pattern is saved. To achieve approximately 2π (or multiples of 2π , if the maximum phase shift is sufficient) phase modulation, the minimum and maximum voltages are adjusted. Then, with a fine scan of the voltage, the nonlinear phase response is

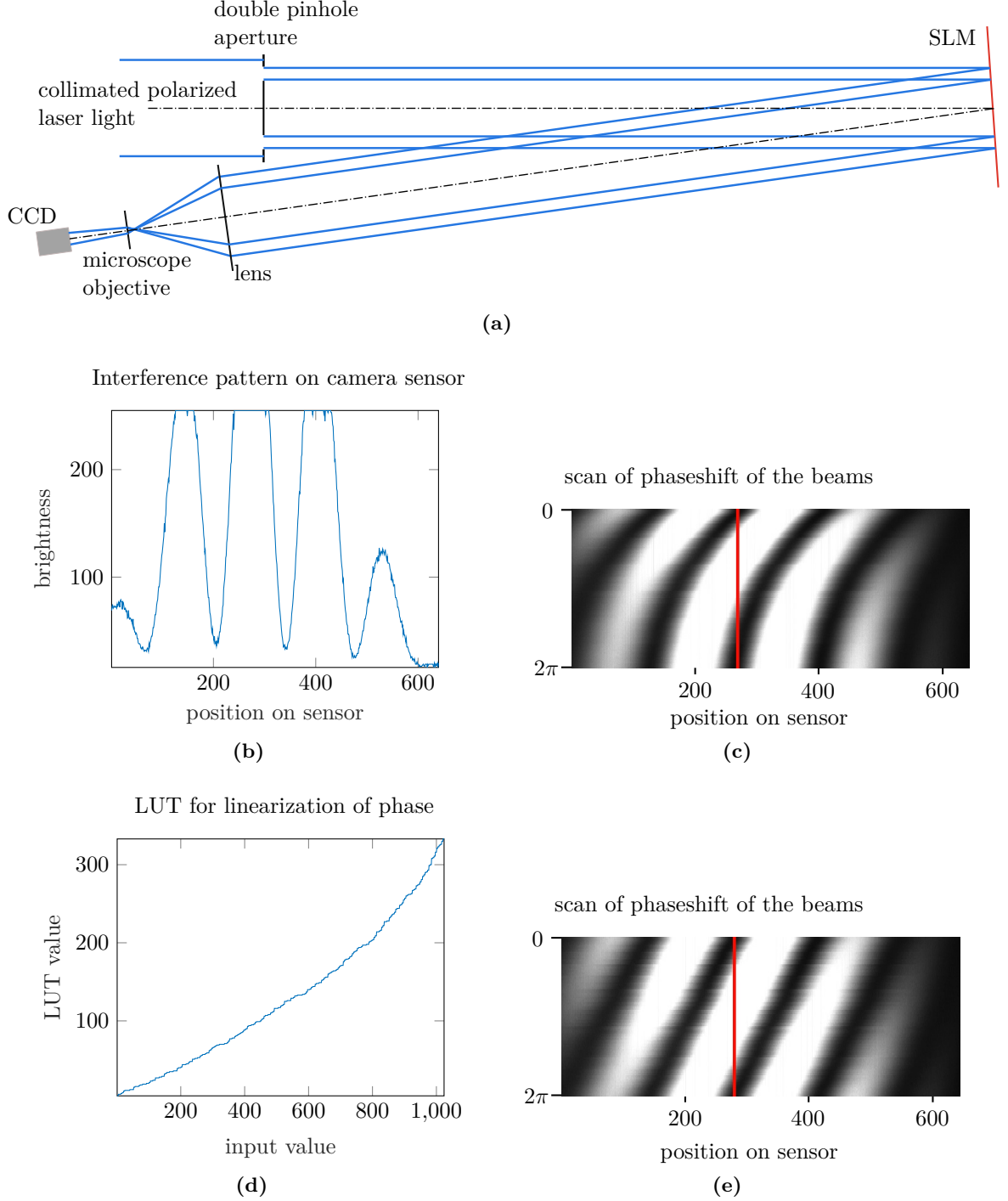


Figure 3.7: Calibration of phase response - (a) Optical setup. Each of the two beams are incident on one half of the SLM display. The interference pattern is magnified with the microscope objective and observed with the camera sensor. (b) Interference pattern on the camera sensor (CCD). (c) The voltage for one of the beams is changed in small increments and the resulting lateral movement of the interference pattern is recorded. The red line visualizes the maximum phase shift of 2π when the pattern is moved laterally by one period. (d) Look-up table (LUT) created from nonlinearity in (c) for linearization of phase response. (e) Linearized phase response when LUT was applied. [99]

measured in Fig. 3.7 (c), and inverted to serve as a look-up table (LUT) for linearization of the phase response in Fig. 3.7 (d) and a final scan is done with the LUT applied, the linear phase response from 0 to 2π is demonstrated in Fig. 3.7 (e).

The two-beam setup does not account for a spatially varying phase response (described in section 3.2.3), however phase modulation uniformity was measured for a Holoeye Pluto LCoS display with a relative standard deviation (RSD) of 0.83% [91], therefore the calibration of the phase response at two points of the display is considered sufficient here.

3.3.2 Pixel crosstalk measurement

In this section, the maximum effect of pixel crosstalk is imposed with the smallest grating periodicity and the highest phase separation that the Pluto-2 LCoS is capable of in its current configuration. Its effect on the diffraction efficiencies is then investigated, whereas the efficiency of the +1. diffraction order is of interest because it is used to form the pattern in holographic projection. The pixel crosstalk can decrease the hologram efficiency, as described in section 3.2.1. To determine the significance of the pixel crosstalk of the Pluto-2 LCoS at 405nm wavelength, power measurements of diffraction orders are conducted for displayed binary gratings with a grating duty cycle of 50% at two and four pixels periodicity. The shorter periods should correspond to a larger crosstalk effect, due to more pixel boundaries affected. Then, the phase level of one of the grating halves is shifted from $0 - 2\pi$ and the power in the 0., +1., and +2. diffraction orders is measured. For this, the intensity sensor "Coherent PM USB UV/VIS" and the pinhole are moved laterally, as illustrated in Fig. 3.8.

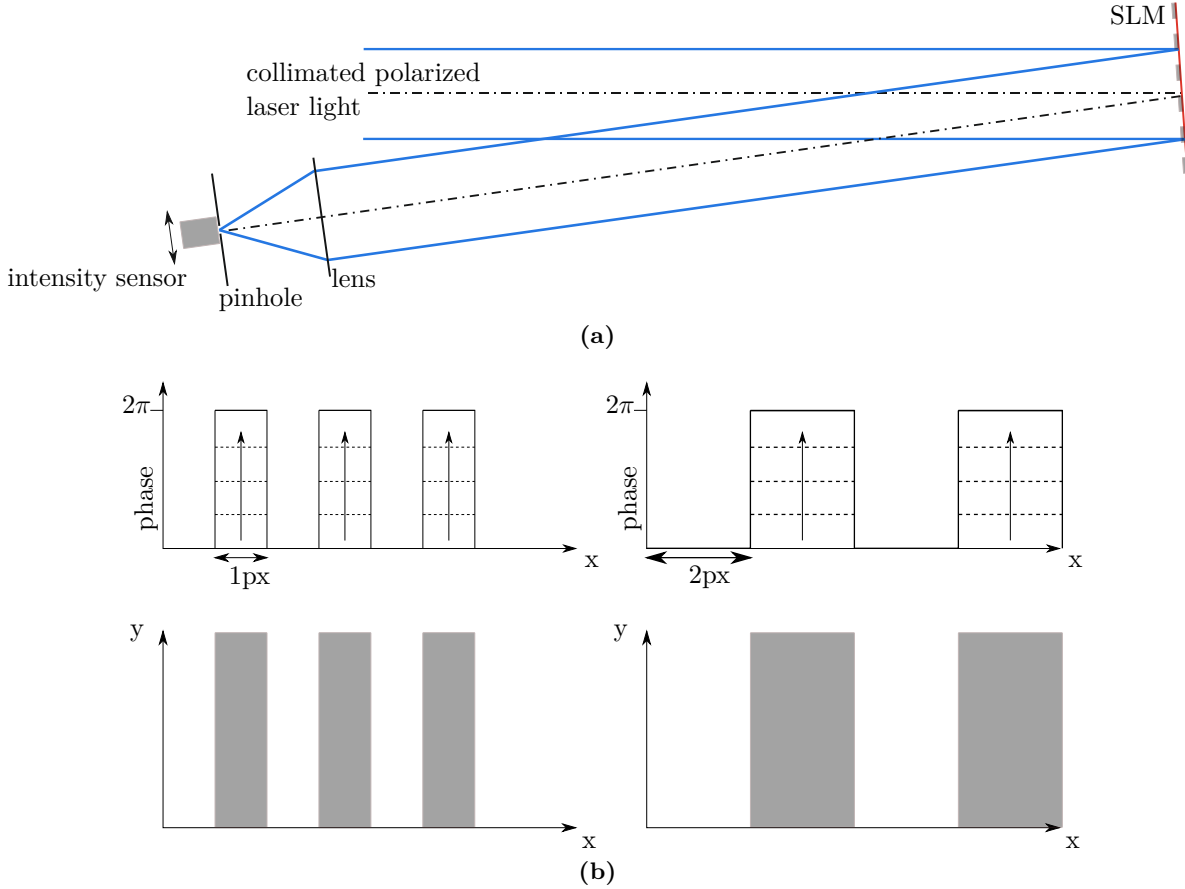


Figure 3.8: Setup for measurement of diffraction orders - (a) Experimental setup (b) Schematic of the grating phase shift, which is increased in small increments from 0 to 2π . Two gratings are used with a periodicity of 2 pixels and 4 pixels, corresponding to a periodicity of 16μm and 32μm, respectively.

The detrimental effect of crosstalk shows as a shift of the maximum power in the +1. diffraction order to higher phase levels [84]. The crosstalk effect is expected to be most significant when the phase separation is close to 2π because then the voltage difference between the phase levels is at its highest. The resulting efficiencies displayed in Fig. 3.9 show that the LCoS device in use does have a small crosstalk effect, however it mostly affects the zero order intensity. For hologram projection, only the intensity in the 1+. diffraction order is important, which does show some asymmetry for the smallest grating period, but the maximum power in the +1. diffraction order, which is expected at π phase shift or a phase level of 127, does not shift significantly towards higher phase levels even for the smallest grating that can be displayed on the SLM. To conclude, some crosstalk is present for structures at the limit of performance of the device, but it is not expected to significantly impair the holographic projection quality.

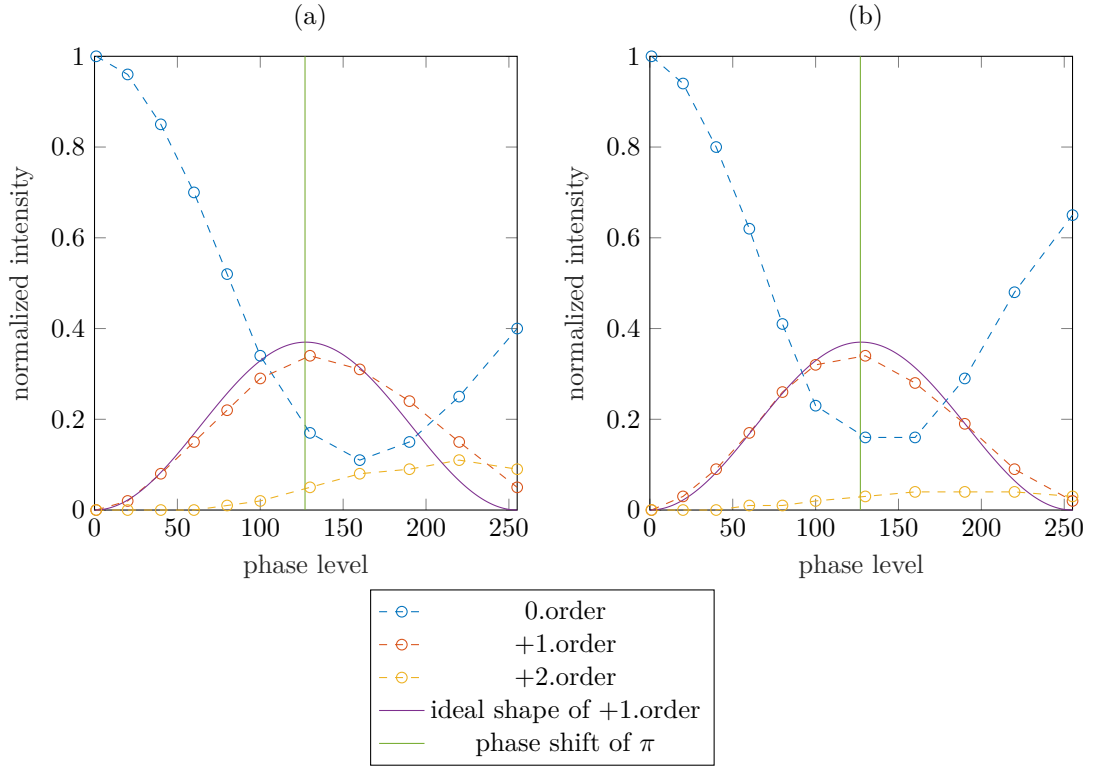


Figure 3.9: Results for measurement of diffraction orders - The measured power in different diffraction orders for (a) grating with two pixels periodicity, (b) grating with four pixels periodicity. Phase level $0 \dots 2\pi$ is $0 \dots 255$.

3.3.3 Aberration measurement and correction

In this section, a method for wavefront measurement with the LCoS is described and then applied for the measurement and compensation of the static aberrations induced by the LCoS backplane. This is necessary because the backplane aberrations have a negative impact on projection quality. To achieve aberration compensation, first the effect of constant curvature of the backplane is compensated for by defocusing of the light illuminating the LCoS, then a Shack-Hartmann-based method with microlenses displayed on the LCoS is implemented and used for measurement of the residual aberrations. Finally, the quality of the calculated

phasemap for aberration compensation is validated by measurements with a commercial Shack-Hartmann sensor (SHS).

It is common for LCoS-SLMs to induce static aberrations to the reflected light, which degrade performance and projection quality, as described in section 3.2.5. For the device in use, the effect causes a distorted holographic projection, see Fig. 3.10. Because of this, a wavefront measurement is required. To achieve a phase measurement with good spatial and phase resolution and a straightforward calculation of a phasemap for aberration compensation, an appropriate wavefront measurement method is required. Due to the phase modulating nature of the LCoS-SLM, the optical phase structures displayed on the SLM can be leveraged for wavefront measurement. The method described in this section uses a Shack-Hartmann-based setup by displaying micro lenses on the SLM and evaluating the resulting focal spot array with a digital camera sensor [94, 100]. In the following, the implementation and improvement of this method is described.

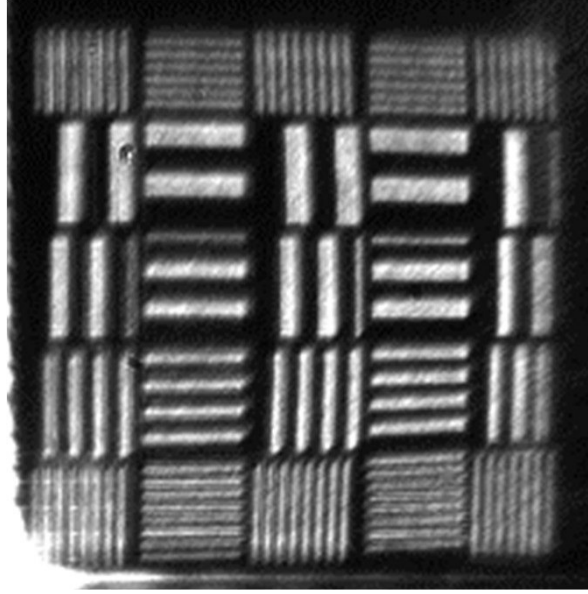


Figure 3.10: Effect of backplane aberrations - Pattern projection with the quadratic phase method from section 4.1.2 demonstrates the distorting and defocusing effect of LCoS backplane curvature on projection quality.

Through preliminary measurements of the wavefront error with a Michelson interferometer setup, the wavefront peak-to-valley error induced by the LCoS backplane curvature can be estimated to about four wavelengths at 633nm with a mostly constant curvature, see Fig. 3.11.

For the actual phase measurement, first the constant curvature of the LCoS-SLM backplane is compensated by targeted defocussing of the collimator module illuminating the SLM. This is possible as long as the setup does not include multiple SLMs in parallel or multiple passes on one SLM and has the advantage of decreasing the required dynamic range for the following phase measurement. The algorithms for the design of micro lenses and for spot detection are described in detail in the following subsections.

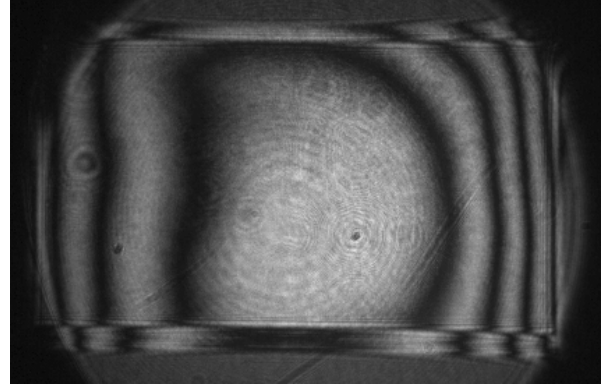
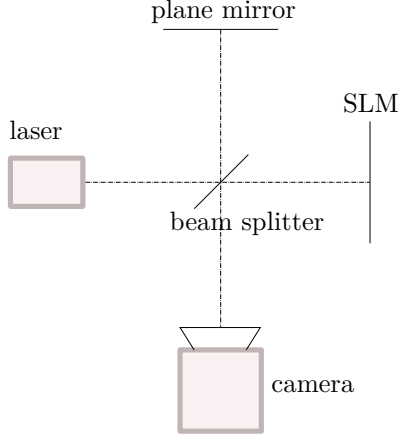


Figure 3.11: Preliminary SLM aberration measurement with Michelson setup - left: schematic of the setup, right: resulting interference pattern. Display size is 15.36mm×8.64mm.

Micro lens design for Shack-Hartmann based optical setup with SLM

The micro lens array design for phase measurements with a SHS based setup is described and how the critical parameters influence the resolution and dynamic range of the measurement system.

The optical setup consists of the microlenses displayed on the SLM "Holoeye Pluto-2", a collimated laser illuminating the SLM at wavelength 405nm, and a camera sensor "Imperx IGV-B2020M-KF000" with 7.4μm pixel size and a resolution of 2048 × 2048 pixels for capturing the focal array images.

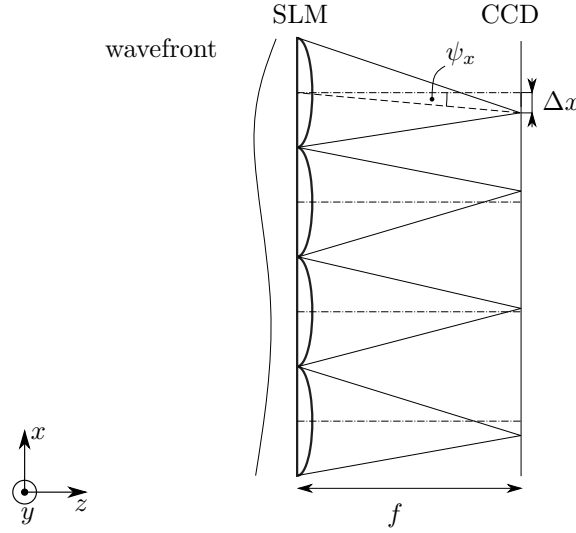


Figure 3.12: Shack-Hartmann principle - An array of micro lenses displayed on the phase-only SLM and a camera sensor in the focal plane are used to measure the local displacement of the focal spots, from which the wavefront tilt can be calculated. The spot displacement Δx corresponds to an average wavefront tilt ψ_x over a micro lens aperture. The spot displacement is zero for a plane wavefront.

The two critical parameters for the design of an appropriate microlens array are the focal length and the lens diameter, as shown in Fig. 3.12. In the setup used here, a lower boundary is placed on the focal length due to the tilted incidence angle on the SLM, requiring a minimum

distance of SLM and camera chip for separation of the incident and reflected light see Fig. 3.13.

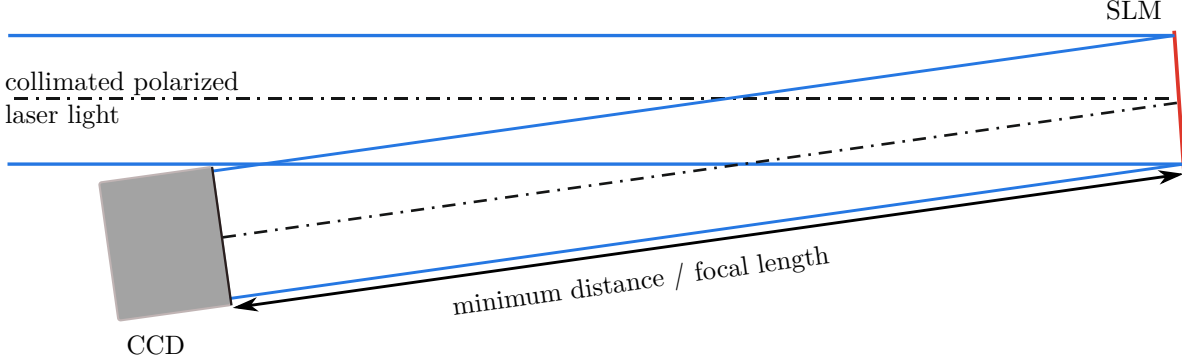


Figure 3.13: Schematic of optical setup for wavefront measurement

Generally, lower focal lengths increase the dynamic range for wavefront measurements but decrease the sensitivity for small phase changes. Furthermore, in this setup the wavefront is measured at the location of the camera chip which does not coincide with the SLM location, so if large deviations/aberrations from a collimated beam are present, the wavefront may have changed over this propagation distance.

Smaller lens diameters allow for higher spatial resolution but decrease the dynamic range in terms of maximum reliably detectable wavefront tilt, a lower boundary is caused by the pixelation of the SLM, which will decrease the focal spot quality for the microlenses if the number of pixels forming the micro lens is too low.

The setup demonstrated in [94] uses an array of two by four large micro lenses (400×400 pixels) and spatially shifts them for a sequential scanning of the wavefront, resulting in a large number of spatial sampling points, but without sampling points near the display edge. This design is improved here to allow for a single-shot measurement with good spatial resolution, with sampling points as close to the SLM display edge as possible. With the method from [94], the distance of the sampling points to the outer boundary of the SLM is relatively high, requiring extrapolation of the wavefront for a phasemap of the full LCoS display. With the improved micro lens design, the focal points can be measured much closer to the display boundary, see Fig. 3.15 (d).

For easier conversion of the focal spot array from the pixel array of the SLM to the pixel array of the camera sensor, and to have the evaluation grid align with the pixel grid of the camera sensor, the distance between two focal spots (here also named micro lens diameter) should be chosen so that it is a full multiple of each pixel size. Given the pixel size of the SLM of $8\mu\text{m}$ and the pixel size of the camera chip of $7.4\mu\text{m}$, an appropriate micro lens size of 98 pixels on the SLM is chosen, resulting in a grid of

$$98\text{px} \cdot \frac{8\mu\text{m}}{7.4\mu\text{m}} = 105.95\text{px} \quad (3.1)$$

on the camera sensor.

Preliminary tests show that micro lenses sized 98×98 pixels are large enough to achieve usable focus spot quality, see Fig. 3.14. The larger size of the focal spots does not significantly

decrease the measurement accuracy, as long as their center of gravity can be reliably detected and as long as they do not overlap. Fig. 3.14 also shows that while the spatial sampling distance is decreased with the new design, the spatial averaging area is also decreased, so the detection of higher spatial frequencies in the wavefront should not be impaired.

Also, ideally the full SLM display should be covered with micro lenses. The micro lenses are positioned on a rectangular grid and each micro lens phase fills its full square shaped aperture to increase the efficiency. The resulting phase profile is shown in 3.15 (a) and (c).

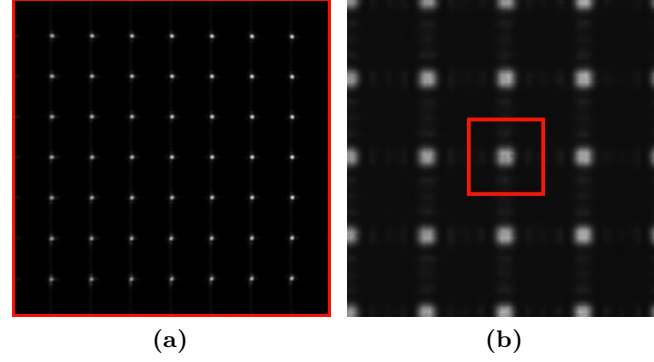


Figure 3.14: Focal spots from different micro lens arrays - Image size is $3.2\text{mm} \times 3.2\text{mm}$ (a) focal spots from array of 400×400 pixels sized microlenses, sequentially scanned and stitched. (b) focal spots from array of 98×98 pixels sized microlenses. Red frame: size of the micro lens aperture of the middle focal spot.

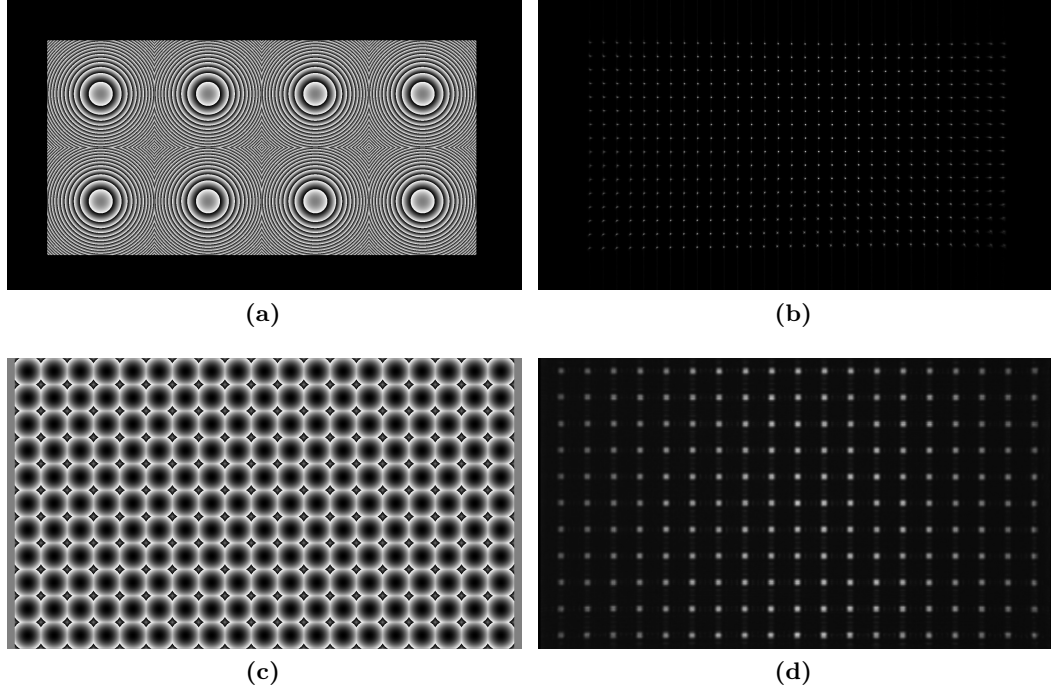


Figure 3.15: Micro lens designs and resulting focal spot arrays on camera sensor - Image size is $15.36\text{mm} \times 8.64\text{mm}$, which is the full size of the LCoS display. (a) Design from [94] and (b) corresponding focal spot array (computed from 64 images of laterally shifted micro lens arrays) (c) Improved design for single-shot measurement and (d) corresponding focal spot array.

Algorithm for spot detection and wavefront calculation

This section describes the evaluation of the focal spot array image captured with the camera when the SLM displays the micro lens array. First, the evaluation grid is overlaid with the spot array, then within each spot region, the focal spot location is first approximately determined by the pixel with the highest intensity, then, in a defined region around it, the weighted centroids method is used to calculate the focal spot location with subpixel accuracy by calculating the center of mass for the intensity of the focal spot

$$x_c = \frac{\sum [I(x) \cdot x]}{\sum I(x)} \quad (3.2)$$

$$y_c = \frac{\sum [I(y) \cdot y]}{\sum I(y)}. \quad (3.3)$$

The focal spot position relative to the grid

$$\Delta x = x_c - x_r \quad (3.4)$$

and

$$\Delta y = y_c - y_r \quad (3.5)$$

is the spot displacement, see Fig. 3.16.

The result of this are two maps of spot displacements in x - and y -direction which can then be converted into local wavefront tilts with the geometric relations

$$\frac{\partial \phi}{\partial x} = \psi_x = \arctan \left(\frac{\Delta x}{f} \right) \quad (3.6)$$

and

$$\frac{\partial \phi}{\partial y} = \psi_y = \arctan \left(\frac{\Delta y}{f} \right) \quad (3.7)$$

according to the schematic in Fig. 3.12. The wavefront can then be calculated by numerical integration of the wavefront tilts with the zonal method [101], taking into account the pixel size and number of pixels. The calculated phase map is inverted to compensate the measured aberration. The algorithm is summarized in a block diagram in Fig. 3.17.

Validation of aberration correction

First, the phase map calculated in the previous section according to Fig. 3.17 is added to the micro lens array phase, then an image of the focal spot array is taken with the camera sensor. The phase map generated from this measurement would ideally be planar compared to the previously measured phase map. Fig. 3.18 shows the measured wavefront with and without the aberration compensating phase map.

However, systematic errors can be present in the measurement, for example, a relative rotation of the camera sensor with respect to the SLM can make the correct alignment of the spot array to the evaluation grid difficult or impossible, especially rotation around the z -axis. Thus, a validation of the method is done with a Shack-Hartmann sensor (SHS) Optocraft SHSLab BR-110-GE-STD. With the SHS, the phase is measured for the middle section of the

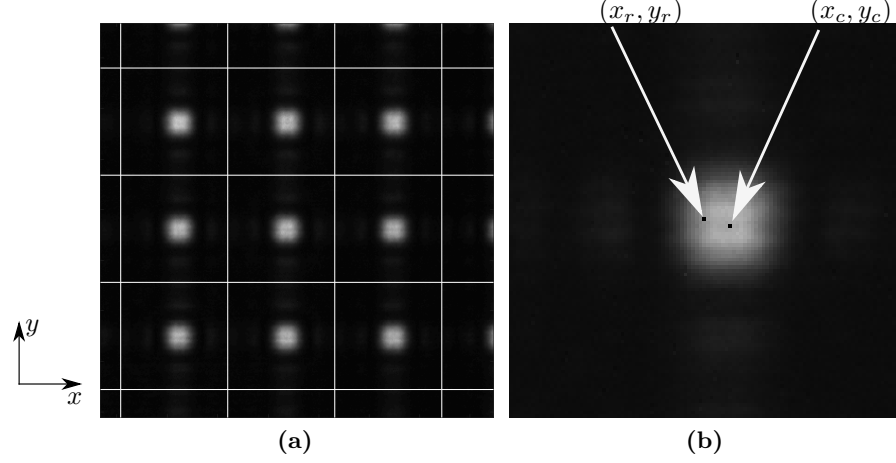


Figure 3.16: Focal spot displacement - (a) zoomed in view of focal spot array overlaid with evaluation grid, (b) view of one detection area, x_r, y_r reference grid position, x_c, y_c center of focal spot. The spot is detected with subpixel accuracy by the weighted centroids method and the x - and y - distances to the middle are then calculated.

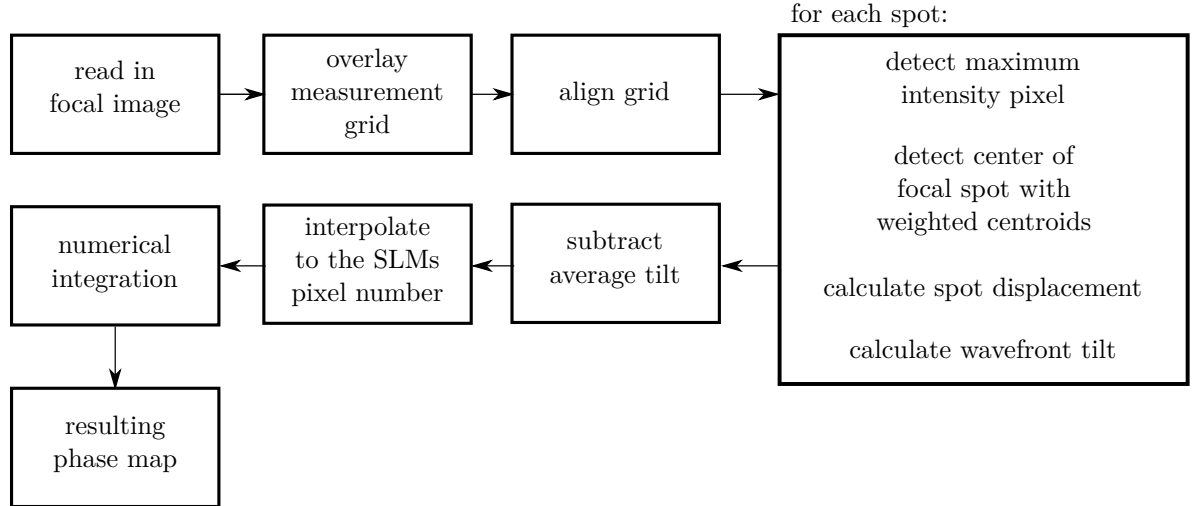


Figure 3.17: Block diagram of spot detection and wavefront calculation - The pre-alignment of the grid and the subtraction of average tilt are done to remove wavefront tilt from the result, which does not decrease the projection quality.

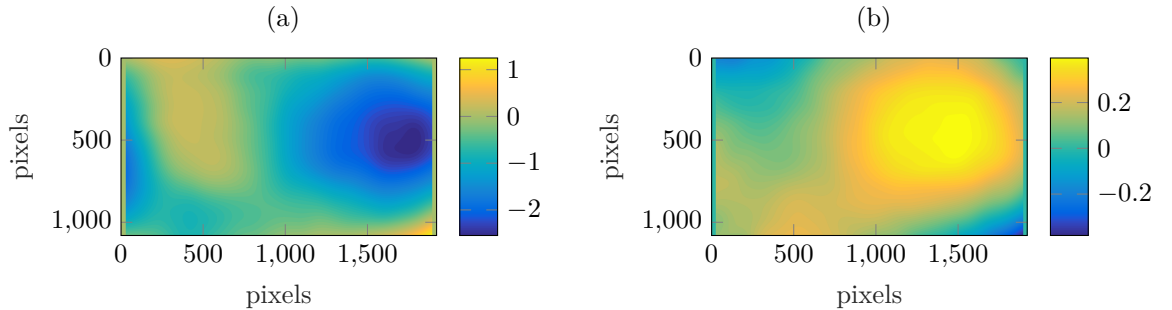


Figure 3.18: Measurement with aberration compensation phasemap. - Phases are plotted in multiples of λ , scale bars are different. (a) initially measured phasemap, peak-to-valley error 3.80λ (b) result measured with compensation phasemap, peak-to-valley error 0.78λ . Phasemaps are displayed for the full LCoS display.

display, see Fig. 3.19 (a). Tilt and defocus terms are subtracted because they do not contribute to decreased projection quality (defocus can be compensated by refocusing). Quantitative comparison of the algorithm from [94] with the modified version from section 3.3.3 is shown in Fig. 3.19 (b), (c), and (d), demonstrating the aberration reduction with the calculated phasemap. The improved method with smaller micro lenses and without sequential imaging has comparable performance to before.

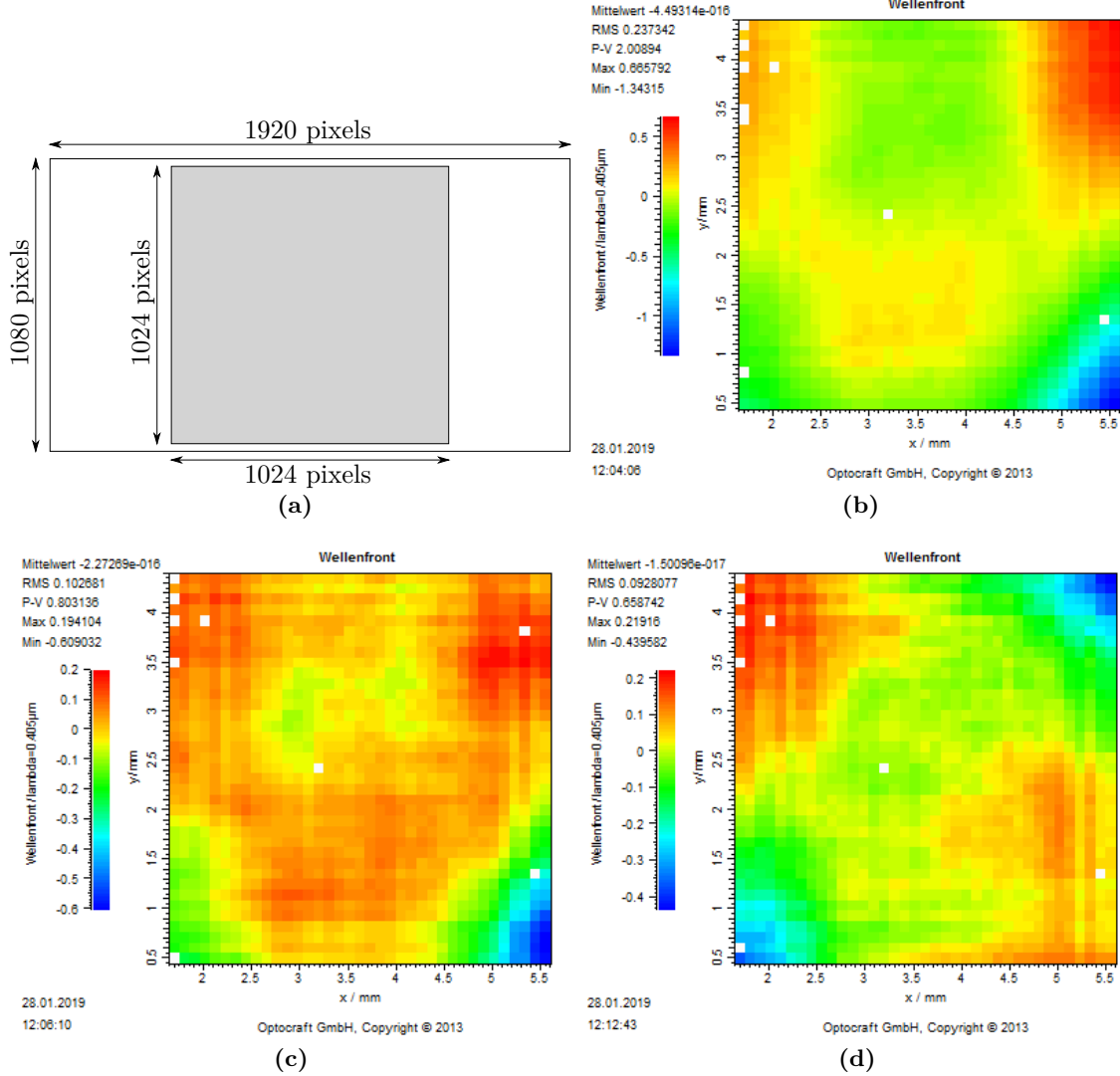


Figure 3.19: Wavefront measurements with Shack-Hartmann-Sensor - (a) location of the measured area on the SLM display, coinciding with the location used for hologram display in the following sections. (b) phase measured with SHS without aberration compensation, peak-to-valley error 2λ . (c) phase measured with SHS with aberration compensation method from [94], peak-to-valley error 0.8λ . (d) phase measured with SHS with improved aberration compensation method, peak-to-valley error 0.66λ .

To conclude, a reduction of the aberrations caused by the LCoS backplane to a root mean square (RMS) error of 0.092λ at 405nm is achieved by first compensating the constant curvature portion by refocusing with the collimator module, then using the SHS principle to capture a spot array from a micro lens array displayed on the SLM and calculating an aberration correction phasemap from it.

3.4 Summary of Chapter 3

In this chapter, the LCoS-SLM technology for phase-only light modulation is described. First, the PAN cell structure is described, which is how pixelized pure phase modulation is achieved with a liquid crystal layer. Then, the various unwanted effects of LCoS devices on the phase modulation and projection quality are described. Included are two effects (zero order, spatial frequency response) that are affected by LCoS device properties, but are present in every type of hologram display (not exclusive to LCoS). Furthermore, the steps taken for the characterization and calibration of the LCoS device used in this work is described. For this, the phase response is calibrated to 2π linear phase shift, the pixel crosstalk effect is measured, and the compensation of system aberrations is achieved with a compensation phase map calculated from measurements with an improved Shack-Hartmann setup that uses micro lenses displayed on the LCoS device.

4

Optimization of Hologram calculation

One of the greatest challenges in holographic projection is speckle contrast, thus its reduction is an important aspect, especially for lithographic applications that are susceptible to intensity variations. Furthermore, a fast calculation of holograms can allow for integrated readjustment of projections to nonplanar surfaces. The quadratic phase method is chosen for this work because direct search methods are very computationally costly, analytic calculation methods are not flexible enough for maskless microstructuring, and the random-phase IFTA causes high speckle contrast, recalling section 2.4.

This chapter describes the optimization of iterative and noniterative hologram calculation approaches that use a predetermined quadratic phase from the geometric optical layout for initialization. This allows for fast convergence and reduction of speckle contrast. An optimization of the algorithm and its variations is done with simulations that are validated by experiments. This approach includes a restriction of projection phase and a spatial coupling of hologram and projection, and both aspects can be leveraged for extension of the algorithm to 3D holographic projection in order to project patterns on nonplanar surfaces. A concept based on additional propagation steps is introduced to the hologram calculation algorithm and validated by simulation and experiment. The algorithms for far field projection described in this section are based on the error diffusion (ED) and iterative Fourier transform algorithms (IFTA), which are described in sections 2.4.2 and 2.4.3, respectively.

4.1 Quadratic phase hologram calculation

This section describes the structure of quadratic phase based hologram calculation algorithms. First, as a general introduction the hologram calculation schematic is described for near field projection, and then the far field quadratic phase hologram calculation used in this work is described in detail, including its advantages and drawbacks.

For the calculation of phase-only holographic elements, the usage of a predetermined quadratic or spherical phase for initialization of an iterative phase retrieval algorithm has been demonstrated for different applications, such as beam splitters [102], beam shapers [36] and projection of video frames [63]. The basic setup can be lensless (Fresnel hologram) or

with a Fourier transform lens (Fraunhofer/Fourier hologram). In both cases, the quadratic phase is calculated in such a way that the light reflected or transmitted by the hologram is redistributed so that it illuminates the projection area.

4.1.1 Near field projection

Summarizing [103], lensless quadratic phase hologram calculation was achieved with Fresnel shifted and scaled propagation. While this optical setup is not used in this work, its schematic setup is described to provide an introduction to quadratic phase based hologram calculation. As seen in Fig. 4.1, a CGH sized s_h is illuminated with collimated light of constant intensity, and a projection area sized s_p (larger than the CGH) is set at a distance z_p to the CGH. For the CGH to illuminate the full projection area, a defocusing lens phase is used. As the hologram is illuminated with collimated light, the location of a virtual point source can be calculated from the geometric parameters with

$$\frac{s_p}{s_h} = \frac{(z_p + z_f)}{z_f} \implies z_f = \frac{z_p}{\frac{s_p}{s_h} - 1}. \quad (4.1)$$

The phase profiles of the hologram and the projection can then be determined, and the hologram calculation algorithm is initialized with the lens phase of the projection. Further constraints of projection distance and size are placed by the hologram display method, the propagation algorithm, and the sampling intervals.

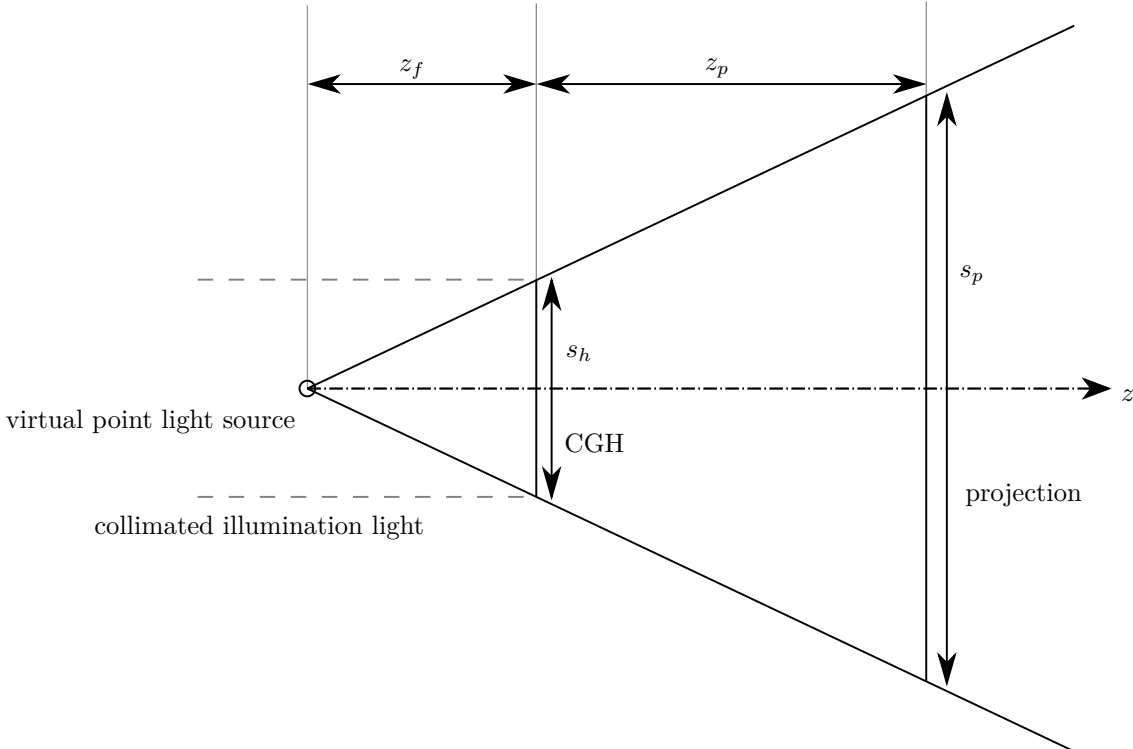


Figure 4.1: Schematic of quadratic phase Fresnel hologram calculation - z , optical axis; s_h , spatial extent of hologram; s_p , spatial extent of projection.

4.1.2 Far field projection

In far field projection, the phase restricted method [40], the non-iterative error diffusion method [47], and the iterative error diffusion method [46] are the available implementations of quadratic phase based hologram calculation. [46] also includes a detailed evaluation of the different implementations. The schematic of the three algorithms is shown in Fig. 4.3. The algorithms are based on the iterative Fourier transform algorithm (IFTA) and/or the error diffusion (ED) algorithm, which are detailed in sections 2.4.2 and 2.4.3, respectively.

The schematic of the quadratic phase calculation with a Fourier transform lens is shown in Fig. 4.2, which demonstrates the geometrical optical relation, which causes that the projection is fully illuminated only when the hologram imprints an appropriate quadratic phase on the collimated light. In the following, we derive the analytical calculation of the quadratic phase in pixel coordinates from the system parameters defined in Fig. 4.2. This approach to calculate the quadratic projection phase ϕ from the system parameters is based on [46] and [47].

The complex wavefront of the projection is calculated

$$A(x, y) = \sqrt{D(x, y)} \exp(-i\phi(x, y)) \quad (4.2)$$

with D target intensity pattern, ϕ projection phase and x, y spatial coordinates. For simplicity, we first consider the one-dimensional case. When the Fourier transform is performed with a lens, the sampling interval in the projection plane

$$\Delta_x = \frac{\lambda f}{s_h} \quad (4.3)$$

and the maximum usable size of the projection

$$s_p = \frac{M\lambda f}{s_h} \quad (4.4)$$

can be calculated from focal length f , wavelength λ , size of the hologram in spatial coordinates s_h , and the size of the projection in pixel coordinates M . Here, M is a positive integer variable depicting the projection size in pixel coordinates, and therefore can not be larger than the hologram size in pixel coordinates.

Considering Fig. 4.2, a' can be calculated from the geometric relations

$$s_p/h = (a' - f')/a', \quad (4.5)$$

$$s_h/h = (a - f)/a, \quad (4.6)$$

the lens equation

$$1/a + 1/a' = 1/f, \quad (4.7)$$

and Eq. (4.4). With $f = f'$ the projection focal length is thus

$$a' = \frac{s_p + s_h}{s_h} f = \frac{(\frac{M\lambda f}{s_h} + s_h) f}{s_h} = \frac{M\lambda f^2}{s_h^2} + f. \quad (4.8)$$

4. Optimization of Hologram calculation

With the focal length determined, the complex wavefront in the projection plane can be described with a quadratic phase

$$A(x, y) = \sqrt{D(x, y)} \exp(-i \frac{\pi}{\lambda(a' - f)}(x^2 + y^2)). \quad (4.9)$$

Combining Eq. (4.9) with Eq. (4.2), the quadratic phase in spatial coordinates

$$\phi(x, y) = \frac{\pi}{\lambda(a' - f)}(x^2 + y^2) \quad (4.10)$$

can be calculated.

The quadratic phase in pixel coordinates in the projection plane

$$\phi(m, n) = \frac{\pi}{\lambda(a' - f)} \Delta_x^2 (m^2 + n^2) \quad (4.11)$$

with pixel coordinates m, n is of interest for the hologram calculation. By inserting Eq. (4.8) and Eq. (4.3) into Eq. (4.11) the quadratic phase factor can be calculated. With

$$\phi(m, n) = \frac{\pi}{\lambda(\frac{M\lambda f^2}{s_h^2} + f - f)} \frac{\lambda^2 f^2}{s_h^2} (m^2 + n^2) = \frac{\pi}{M} (m^2 + n^2), \quad (4.12)$$

π/M results as the quadratic phase factor in pixel coordinates. We note that the factor is independent of λ , f , and s_h and can be calculated just from the projection size in pixel coordinates M .

While this was calculated for square projections, extension to rectangular projections is possible. Then the quadratic phase factor along one axis is then dependent on the size of the projection in pixel coordinates along the respective axis

$$\phi(m, n) = \frac{\pi}{M} m^2 + \frac{\pi}{N} n^2 \quad (4.13)$$

with M projection size along the m axis and N projection size along the n axis.

Advantages

The most prominent advantage of this method is the well-defined quadratic phase of the pattern in the projection plane. This prevents random interference of sampling points, which is the main source of unwanted speckle contrast in CGH projection, see also section 2.4.4. Projected light patterns in a plane calculated with the algorithm have increased depth of focus compared to the Gerchberg-Saxton algorithm, which is a disadvantage in projection of patterns to be viewed with the human eye because the depth perception of 3D hologram projection relies on low depth of focus [104]. However, this is an advantage in pattern projection for lithography on curved surfaces, allowing the structuring of areas with greater height differences. Moreover, in case of height differences exceeding the depth of focus, a multi-plane hologram calculation algorithm for 3D projection (see section 4.3) can use larger propagation distances between segmented planes, which decreases the number of propagation steps and thus the computational load.

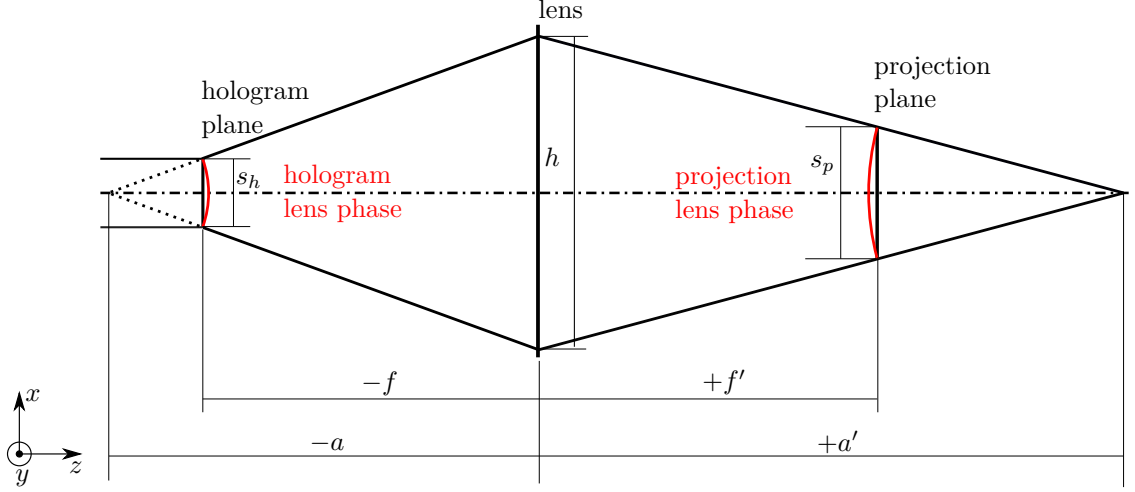


Figure 4.2: Optical setup for far field quadratic phase factor calculation - Schematic of optical setup as used in far field quadratic phase hologram projection. $f = f'$ focal length, h aperture at lens, s_h hologram size, s_p projection size, $-a$ and a' object distance and image distance for imaging of the virtual point source.

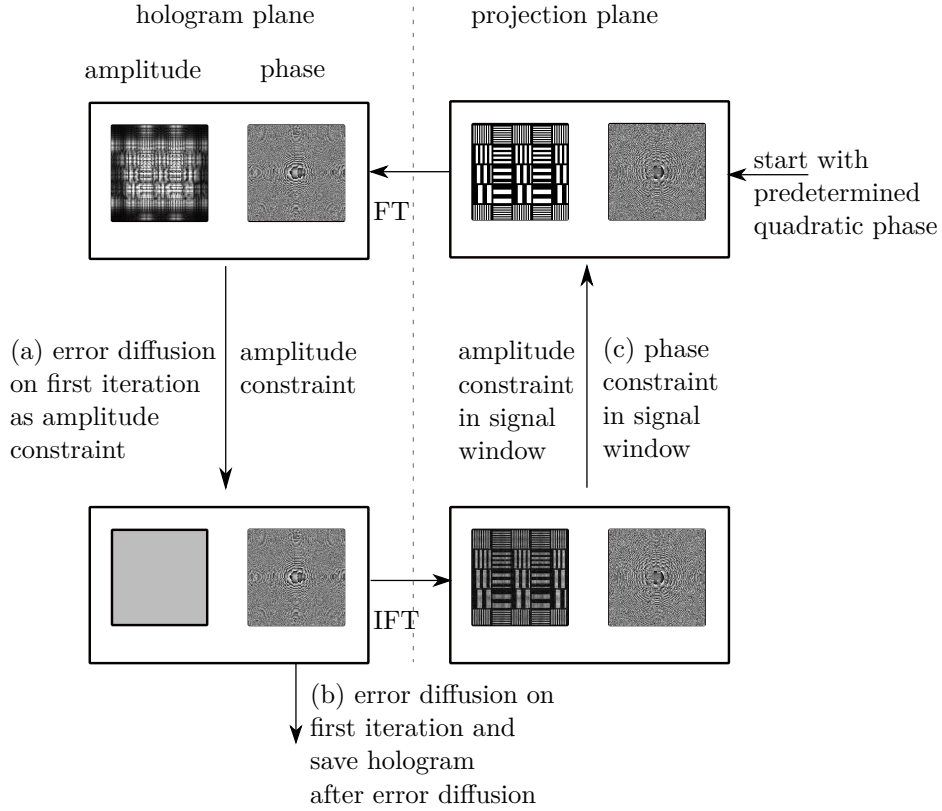


Figure 4.3: Schematic of far field quadratic phase hologram calculation algorithms - (a) is the iterative error diffusion algorithm, (b) generate the non-iterative error diffusion algorithm, modification, and (c) generates the phase restricted algorithm. The iterative algorithms run for a predetermined number of iterations. FT, Fourier transform; IFT, inverse Fourier transform. In the projection plane, the noise window surrounding the signal window is not depicted.

Drawbacks

The main disadvantage of this method is the reduction of the patterning area and sampling points available to the projection because of the usage of a noise window, see section 4.2.2. This decreases the available area that can be patterned in parallel potentially by a large factor,

depending on the size of the noise window. Furthermore, compared to the GSA, the resulting projection is more sensitive to local defects or obstructions of the hologram.

Also, due to intensity being redirected to the noise window, less light is available for the projection, decreasing the diffraction efficiency, see also Eq. (4.14).

4.2 Optimization of 2D projection algorithm and input parameters

To optimize the projection quality and diffraction efficiency, simulations and experiments with test images are conducted in this section. Variations of the algorithm are evaluated and compared, and for optimization of the algorithms, parameter variations of the most important input parameters are conducted, in particular of the scaling factor (SF), which greatly influences the trade-off between diffraction efficiency and projection quality.

4.2.1 Test images, quality criteria, and target parameters

Two very different test images are chosen to allow a broader evaluation, displayed in Fig. 4.4: The grayscale 'cameraman' test image [15] and an image consisting of binary gratings of different orientations and linewidths.

The primary target parameters are projection quality and diffraction efficiency. The hologram diffraction efficiency is defined here as the ratio of intensity in the signal window over the total intensity

$$\eta_{hologram} = \frac{I_{signal}}{I_{signal} + I_{noise}} \quad (4.14)$$

with intensity in the signal window I_{signal} and intensity in the noise window I_{noise} . The projection quality can be defined suitable to the given application. For the 'grating pattern' image, the relative standard deviation

$$RSD = \frac{S}{\bar{x}}, \quad (4.15)$$

is used, which denotes the intensity uniformity with S standard deviation and \bar{x} mean and is a relevant parameter in lithographic illumination.

For the greyscale 'cameraman' image the uniformity is not a suitable quality criterium because its target intensity distribution is not uniform. Therefore, the peak signal-noise ratio (PSNR) is used, which is common in evaluation of video or image quality.

4.2.2 Simulation

In this section, the effect of the various input parameters and the influence of a local obstruction of the hologram is investigated via simulations for the three quadratic phase-based algorithms described in Fig. 4.3. This is done to evaluate and optimize the hologram calculation, to achieve a good compromise of projection quality and uniformity for lithography tests in Chapter 6.

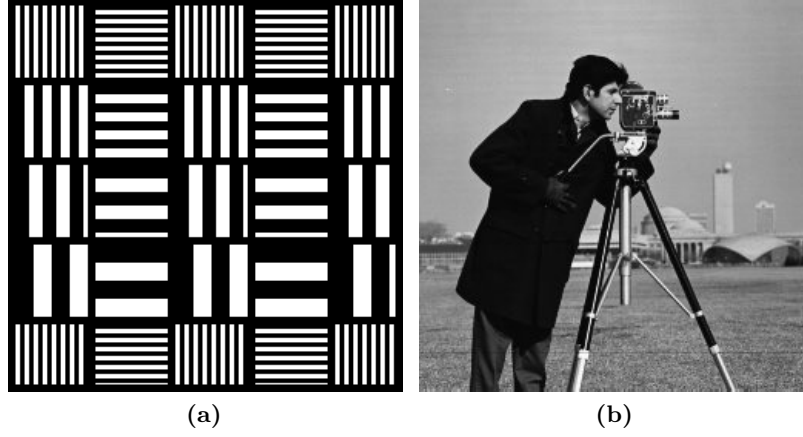


Figure 4.4: Test images for evaluation of hologram calculation algorithms - (a) 'grating pattern' test image, (b) 'cameraman' test image [15].

The various input parameters to the hologram calculation algorithm each affect the projection quality. To optimize the hologram calculation for given applications, simulations can be conducted to determine the influence of the parameters.

Noise window

Due to the phase being predetermined, the iterative algorithm has less degrees of freedom to work with, and so convergence of the algorithm can be slow and the algorithm may achieve suboptimal results. It is similar to the double constraint Gerchberg-Saxton algorithm, which restricts phase and amplitude of the projection in every iteration, described in section 2.4.4.

Thus, to increase projection quality it is necessary to introduce a noise window unrestricted in phase and amplitude, however this decreases the hologram diffraction efficiency and the number of available sampling points for the projection (when the hologram size is constant).

Quadratic Phase Factor

The quadratic phase factor, as described and calculated in section 4.1.2, plays an important role in projection quality. By conducting simulations and analysis of the projection quality, a parameter variation of the quadratic phase factor allows for a more accurate adjustment of the factor to the projection pattern in use that also takes into account the diffraction effects near the edges of the hologram. As described in section 4.1.2 the factor needs to be chosen in a way that the light incident on the projection comes from the fully illuminated hologram. Fig. 4.6 shows the increasing area of the hologram that is illuminated with an increasing quadratic phase factor, and the aliasing caused by the periodic boundary conditions of the FFT when the quadratic phase factor is too large. Fig. 4.5 shows the corresponding significant drop in projection quality measured in PSNR at that point.

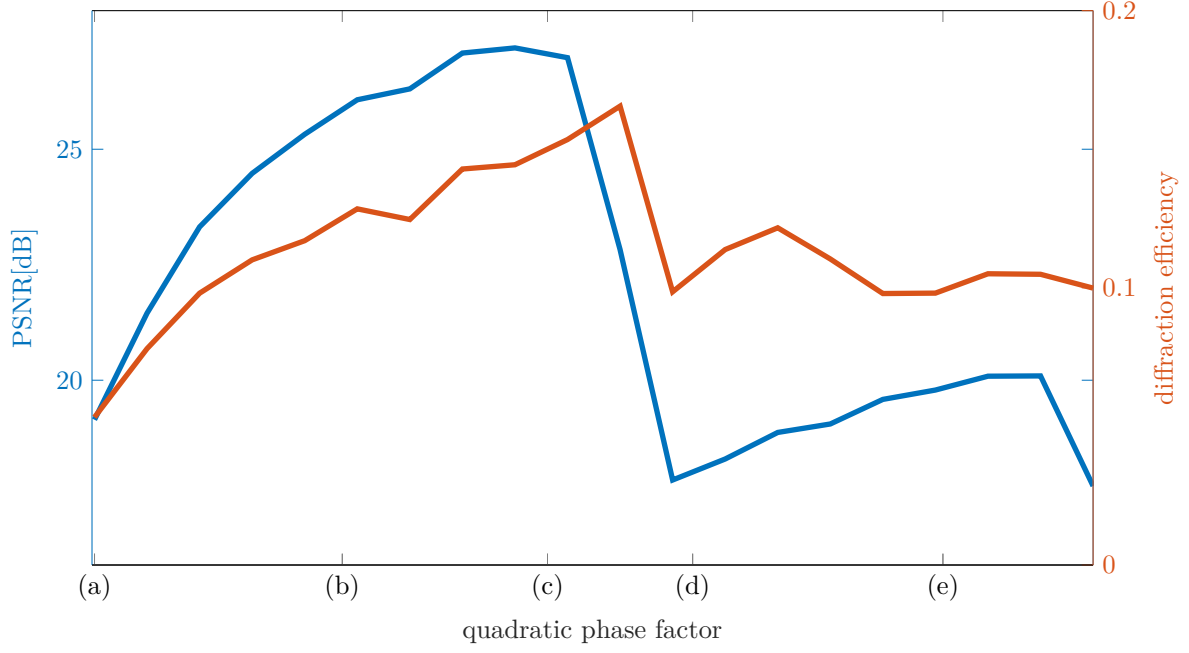


Figure 4.5: Parameter variation of quadratic phase factor with simulation - The quadratic phase factor π/M is varied for the error diffusion algorithm with the 'cameraman' image. The projection quality drops at higher quadratic phase factors than $\pi/M = 0.01$ because the hologram plane is no longer band-limited, as illustrated in Fig. 4.6 (d) and (e). Aliasing in the hologram plane is caused by the implied periodic boundary conditions of the FFT [46]. Note: x-axis is scaled quadratically.

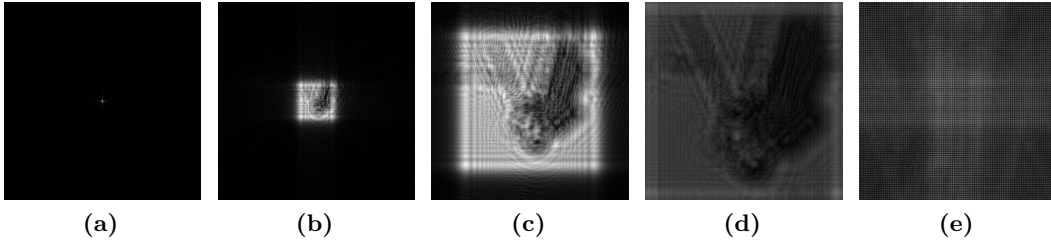


Figure 4.6: Simulated parameter variation of quadratic phase factor: initial hologram amplitude - Visualizes the initial hologram amplitude when the quadratic phase factor is varied. Quadratic phase factors are (a) 0.0001 (b) 0.0025 (c) 0.0091 (d) 0.0144 (e) 0.0289. The maximum projection quality is achieved in Fig. 4.5 when the initial hologram amplitude slightly underfills the full SLM aperture, as in (c). The occurrence of aliasing in (d) and (e) corresponds with the drop in projection quality in Fig. 4.5 [46].

Scaling Factor

The scaling factor (SF) is used to scale the magnitude of the amplitude for the desired projection pattern for iterative algorithms

$$A_c(m, n) = \text{SF} \cdot A_n(m, n) \quad (4.16)$$

with A_c amplitude level used as constraint in the algorithm and A_n normalized amplitude. Due to this nature, in iterative hologram calculation with a noise window, it influences the ratio of signal and noise intensity. This ratio is equivalent to the hologram diffraction efficiency, see Eq. (4.14), and it also greatly influences the projection quality: Only a specific scaling factor

causes the optimum projection quality. With higher scaling factors the available light that can be redirected to the noise window decreases, further constraining the algorithm and thus worsening the convergence of the iterative algorithm and lowering the achievable projection quality. With lower scaling factors the contrast decreases and the effect of random noise increases.

Fig. 4.7 shows the resulting projection quality over diffraction efficiency for the four different implementations of the quadratic phase hologram calculation with variation of the scaling factor. For the noniterative error diffusion algorithm the scaling factor has no effect, resulting in just one data point.

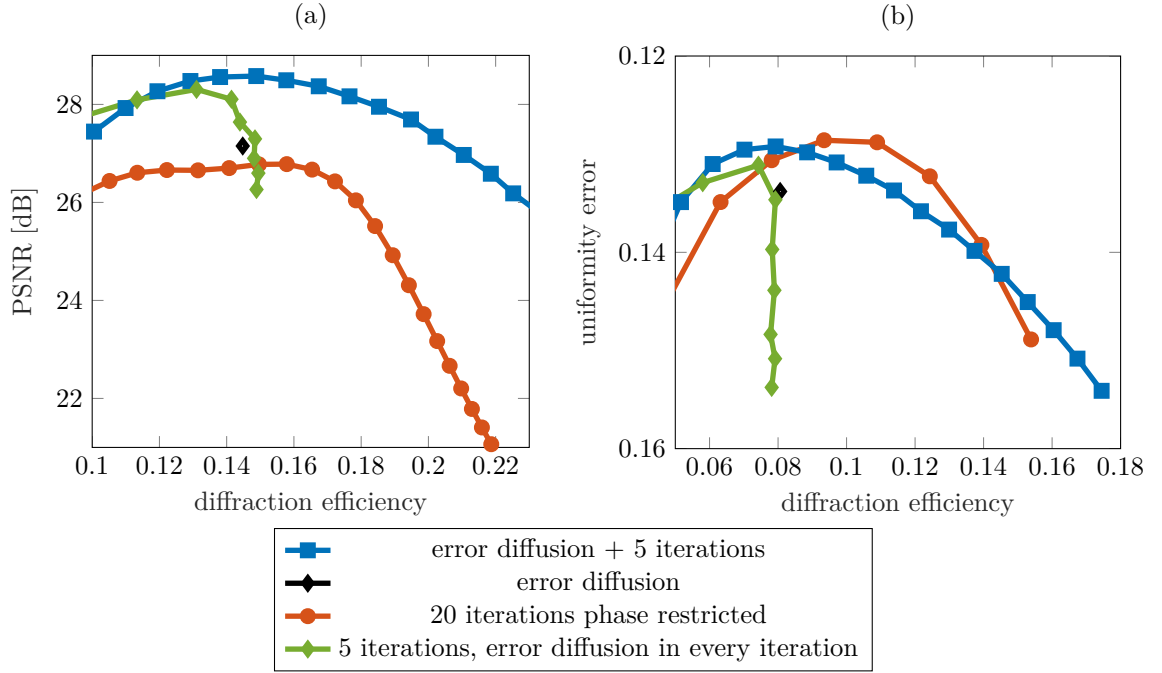


Figure 4.7: Parameter variation of scaling factor for comparison of algorithm variations - (a) Comparison for the 'cameraman' image. (b) Comparison for the 'grating pattern' image. The projection quality criteria are plotted over the resulting diffraction efficiency, which is more relevant for the evaluation of the methods than the scaling factor causing the efficiency and quality [46] because the connection between scaling factor and diffraction efficiency is highly dependent on the pattern that is to be projected. The choice of test images and quality criteria is elaborated in section 4.2.1.

The scaling factors optimum value for the best projection quality depends on the projection pattern itself, for example a sparse pattern with a lot of zero intensity pixels requires a higher scaling factor than a fully illuminated image.

Zero Intensity Frame

In case the error diffusion is not used in the hologram calculation algorithm, most of the intensity in the noise window is distributed adjacent to the projection, see Fig. 4.8 (a). In the simulation it can be observed that this leads to interference effects at the boundary between signal and noise window, decreasing the projection quality. For an exemplary binary grating pattern image sized 256×256 pixels and a hologram sized 1024×1024 pixels the uniformity of the illuminated areas is analyzed for hologram calculation with the phase restricted algorithm. Through variation of the width of a frame with zero intensity around the projected pattern,

4. Optimization of Hologram calculation

the influence on the uniformity of the bright areas of the projection can be discerned, see Fig. 4.8 (b) and (c).

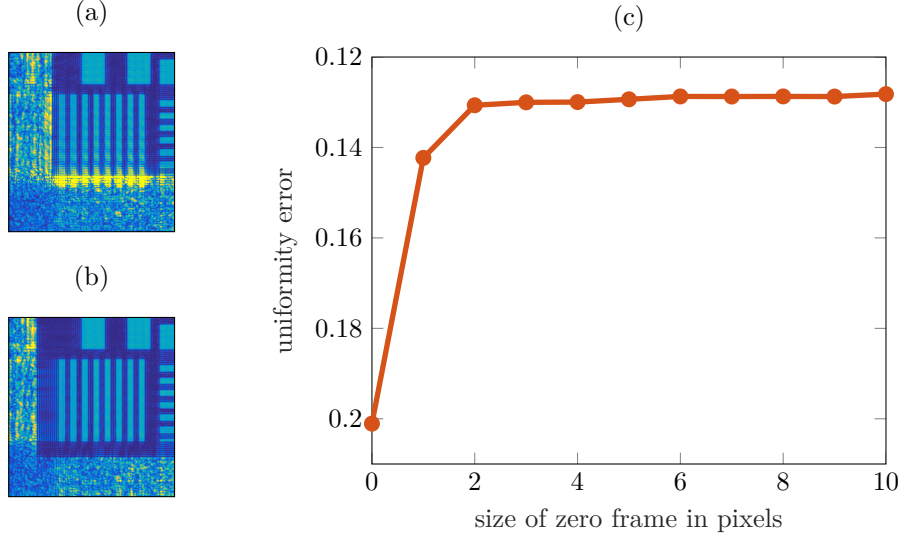


Figure 4.8: Parameter variation of zero intensity frame - For the phase restricted algorithm, the width of a zero pixel frame surrounding the signal window is varied. (a) Detailed view of projection border without zero frame (b) Detailed view of projection border with a zero frame 8 pixels wide (c) Uniformity error of the projection plotted over the width of the zero frame [46].

Simulation of local hologram obstruction

For quadratic phase holograms, in case parts of the hologram are obstructed or unusable for other reasons, for example dead pixels, the local projection quality is expected to decrease. Compensation of this effect is desired since this is a major drawback compared to the standard iterative Fourier transform algorithm, as described in section 4.1.2, if it can be measured and included in the hologram calculation algorithm. To evaluate the capability of this, a local obstruction is placed on the hologram, decreasing the local intensity to zero, displayed in Fig. 4.9 (a). Assuming the obstruction can be measured/determined, the three algorithms get this as the input brightness distribution. The resulting projection intensity is displayed in Fig. 4.9 (b)-(d). The noniterative error diffusion algorithm is not able to compensate for the obstruction due to the error diffusion algorithm only affecting neighboring pixels, the iterative phase restricted algorithm can not redistribute the intensity due to the restriction of phase. Only the iterative error diffusion can redistribute the intensity, preserving some contrast for the full projection even as one quarter of the hologram is obstructed. This flexibility is a distinct advantage over the other algorithms.

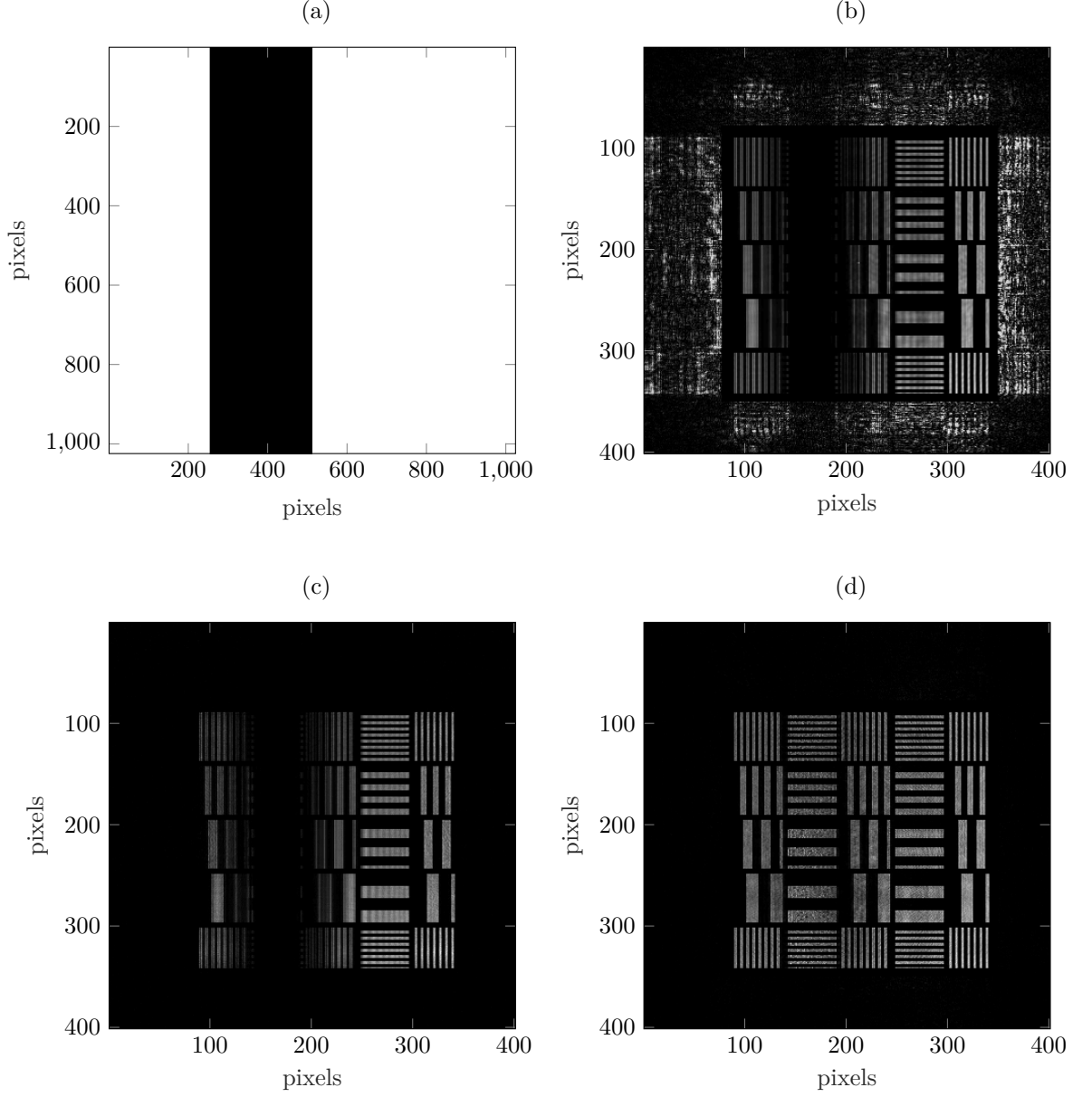


Figure 4.9: Simulation of obstructed hologram - (a) obstruction of hologram (black). Simulated projections with obstruction on hologram with (b) phase restricted iterative algorithm [40], (c) noniterative error diffusion [47], (d) iterative error diffusion [46]. Normalized intensity in arbitrary units.

4.2.3 Experimental validation

Validation of the simulation results is done with a far field projection setup, depicted in Fig. 4.10. The main components are

- SLM "Holoeye Pluto-2-VIS-016",
- camera "uEye UI 1492LE-M",
- laser "Thorlabs LDM405",
- Fourier lens focal length 140mm.

A qualitative validation is performed by calculating holograms for the projection of test images with three different methods, see section 4.1.2, and by parameter variation of the

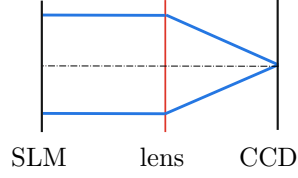


Figure 4.10: Schematic of optical system: The SLM is illuminated with a collimated plane wave (not displayed), the far field is projected on a camera sensor (CCD) with a Fourier transform lens with $f=140\text{mm}$.

scaling factor for the iterative variants. Fig. 4.11 shows the comparison of the three variations of the quadratic phase algorithm. The simulations are validated by the experiments, showing that the error diffusion algorithm is limited to a lower diffraction efficiency than the other algorithms at the same projection quality. For the other two algorithms, the projection quality and efficiency are similar, however, some artifacts occur for the phase restricted algorithm with the cameraman image. This conforms with the simulation in Fig. 4.7 (a), which shows higher projection quality for error diffusion-based algorithms.

Fig. 4.12 shows the results for parameter variation of the scaling factor with the phase restricted algorithm. The increased efficiency with higher scaling factor is confirmed, and the decreased uniformity can also be seen as darker vertical lines in the image. The scaling factor should thus be set so that the desired projection quality is met with the efficiency as high as possible.

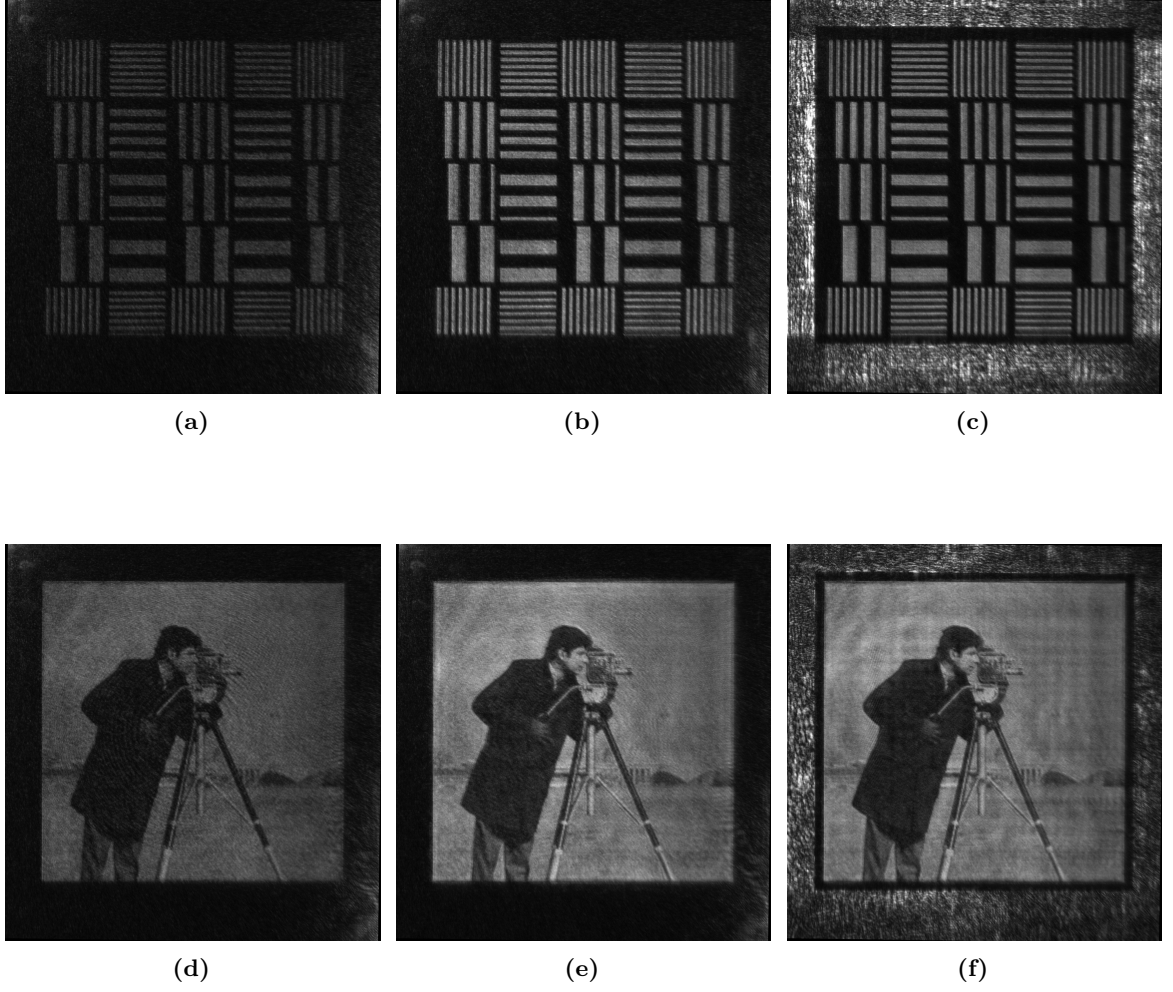


Figure 4.11: Comparison of algorithm variations with experiments - (a),(d) error diffusion. (b),(e) error diffusion plus five iterations. (c),(f) phase restricted iterative algorithm. Two patterns are used for the comparison, and the scaling factor of the iterative methods was set so that the projection quality of the error diffusion method was matched with the highest possible diffraction efficiency [46].

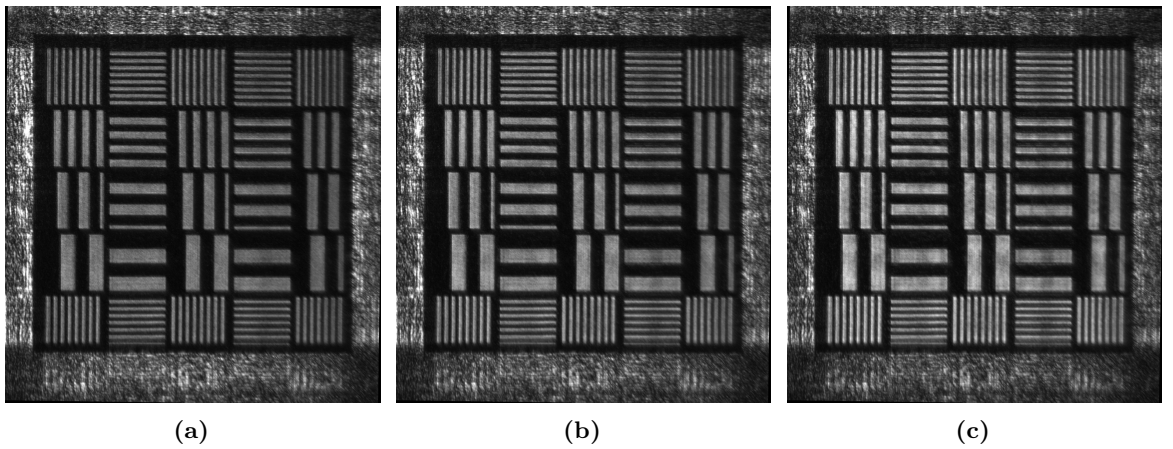


Figure 4.12: Experimental evaluation of parameter variation of scaling factor - The phase restricted algorithm is used with increasing scaling factor from (a) to (c), the uniformity decreases as efficiency increases [46].

4.2.4 Inverted quadratic phase factor

When the quadratic phase of the projection is calculated, the quadratic phase factor can be inverted, and still causes the band-limited intensity in the hologram plane as seen in Fig. 4.6 (c). The optical beam path then changes and the location of the focal spot caused by the projection as well, this is illustrated in Fig. 4.13 which also shows the inversion of the hologram phase from defocusing to focusing. Since the hologram can be calculated in the same manner as before and the simulated projection quality and diffraction efficiency also are the same as before, the sign of the quadratic phase factor can simply be changed in the hologram calculation for adjustment of the beam path to the requirements of the application.

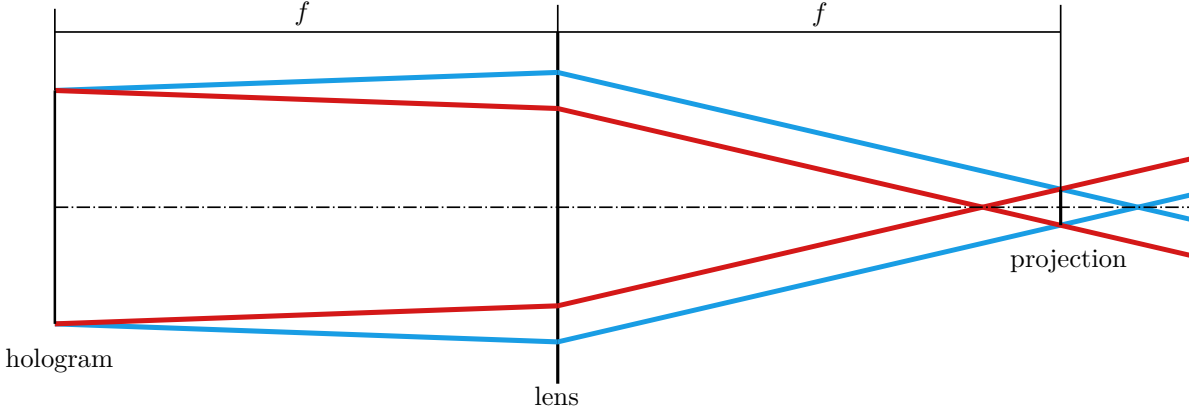


Figure 4.13: Schematic of inverted quadratic phase - Beam paths for regular quadratic phase (light blue), and inverted quadratic phase (red). As the quadratic projection phase gets inverted, the focal point shifts to the other side of the projection and the holograms lens phase also is inverted.

4.3 Extension of the algorithm with short distance propagation for 3D projection

To proceed from projection on a 2D plane surface to 3D surfaces, a common method is segmenting the projection area and using short distance propagation algorithms to move segments of the projection along the z -axis, as outlined in chapter 2.4.5. This can be implemented into far field hologram calculation algorithms: Segments of the projection are propagated to a different transversal plane, then restricted to the desired phase and amplitude, then propagated back to the Fourier plane and added to the other segments, then a Fourier transform is performed to calculate the hologram. As long as the segments do not overlap, no major reduction in projection quality is expected. Here, the far field noniterative quadratic phase error diffusion algorithm is extended with a short distance angular spectrum propagation, projecting the two halves of the pattern in two different depth planes, see Fig. 4.14. The iterative phase restricted algorithm can also be extended to multiple planes, according to the schematic in Fig. 4.15.

For correct calculation of the propagation distance, the optical system parameters need to be taken into account. For the far field projection, the projection pixel size is calculated from

Eq. (2.9)

$$\Delta_x = \frac{\lambda \cdot f}{s_h} = \frac{405\text{nm} \cdot 140\text{mm}}{1024 \cdot 8\mu\text{m}} = 6.9\mu\text{m} \quad (4.17)$$

with f Fourier lens focal length and λ and the size of a 1024×1024 pixel hologram displayed on the SLM. Then with the desired propagation distance, the spatial frequency sampling interval $\Delta_u = 1/\Delta_x$ and λ , the propagator for the AS algorithm from Eq. (2.11) can be calculated.

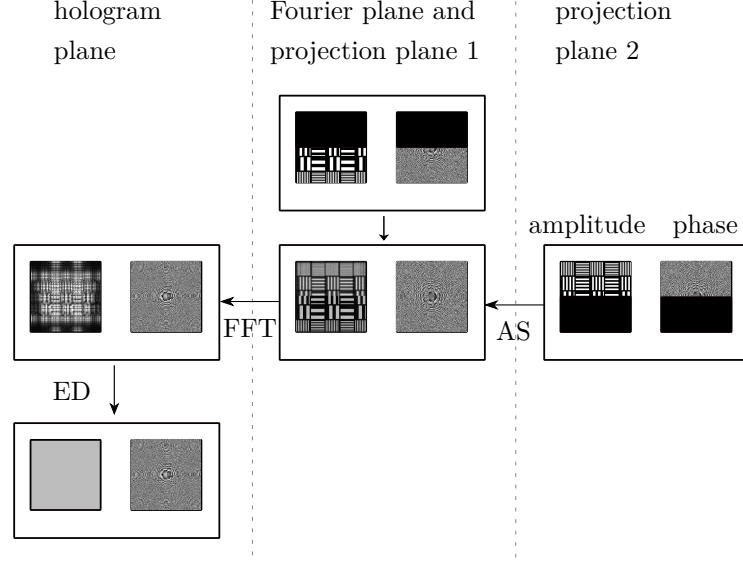


Figure 4.14: Schematic of error diffusion multi plane hologram calculation - The error diffusion algorithm is extended with a short distance propagation, causing half of the projection to be reconstructed in a different plane. FFT, Fast Fourier Transform; AS, angular spectrum algorithm; ED, error diffusion algorithm. Black areas are unrestricted in phase/amplitude. In the projection planes, the noise window surrounding the signal window is not depicted.

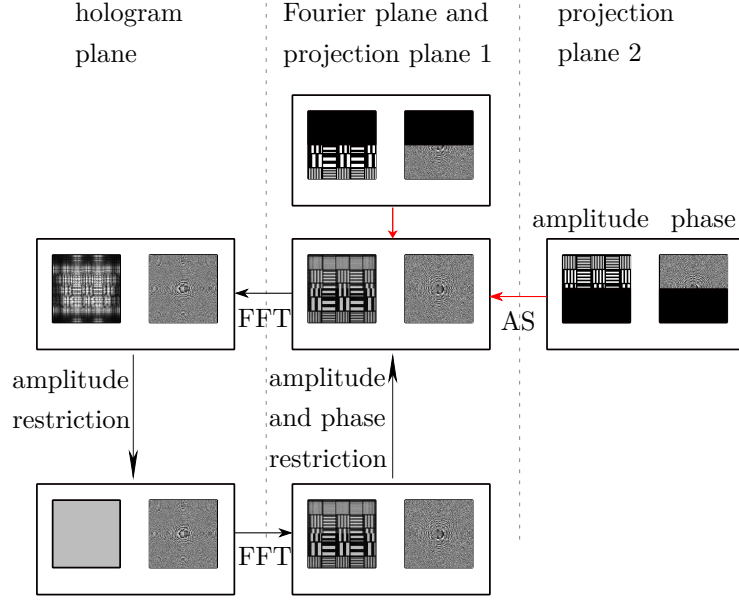


Figure 4.15: Schematic of multi plane hologram calculation - The phase restricted algorithm is extended with a short distance propagation, in this schematic each half of the projection is to be reconstructed in a different plane. Red arrows are initialization steps. Due to the phase restriction it is sufficient to perform the more computationally intensive AS propagation only as initialization before the IFTA. FFT, Fast Fourier Transform; AS, angular spectrum algorithm. Black areas are unrestricted in phase/amplitude. In the projection planes and in the Fourier plane, the noise window surrounding the signal window is not depicted.

4.3.1 Simulation

An analysis of the method is performed by simulation, whereas three segments of a line pattern are projected in three different focal planes. The noniterative error diffusion algorithm is used with an input projection consisting of segments that were propagated by a distance larger than the depth of focus, see Fig. 4.14. A distance of 6mm for the top segment and 2mm for the second segment from the top is chosen, leaving the bottom segment in the Fourier plane.

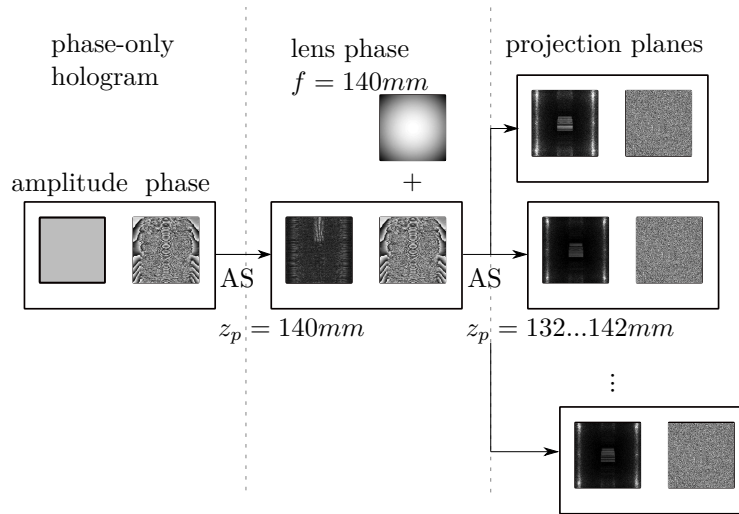


Figure 4.16: Schematic for simulation of multi plane holograms - Hologram was calculated with the error diffusion algorithm, the field size depicted is 8.2mm×8.2mm in every plane. A lens phase is added to the phase-only hologram so far field projection can be simulated. Then different propagation distances are used to evaluate the projection segments in the different transversal planes. AS, angular spectrum propagation algorithm.

The calculated phase-only hologram is propagated by 140mm with the AS algorithm, then a Fourier transform lenses phase profile is added, then a further AS propagation by 132...142mm is done to evaluate the resulting intensity in the different projection planes. The simulation setup is illustrated schematically in Fig. 4.16. Thus, the projection can be evaluated in different distances to the hologram. The 3D hologram calculation methods are validated in that they allow for the projection of patterns with high contrast in multiple focal planes in parallel, results are demonstrated in Fig. 4.17 (a),(c),(f),(i).

4.3.2 Experimental validation

The phase-only hologram calculated in section 4.3.1 is displayed on the SLM. The same optical setup from section 4.2.3 is used, except that the camera sensor is placed on a linear table to allow movement along the z -axis. A blazed phase is added to the hologram for spatial separation from the zero order light. Fig. 4.17 (b),(e),(h) demonstrate the different focal planes for the three segments. The contrast at $x=1\text{mm}$ is compared for simulation and experiment in Fig. 4.17 (d),(g),(j). Apart from the background noise levels in the experiment and minor differences from lateral rescaling, the experimental images are showing a high contrast for the segments in focus and decreased contrast for the out-of-focus segments, same as the simulation. Thus, the 3D hologram calculation methods, which were developed in this section, do allow for a refocusing of projection segments, as desired for 3D holographic projection for lithography.

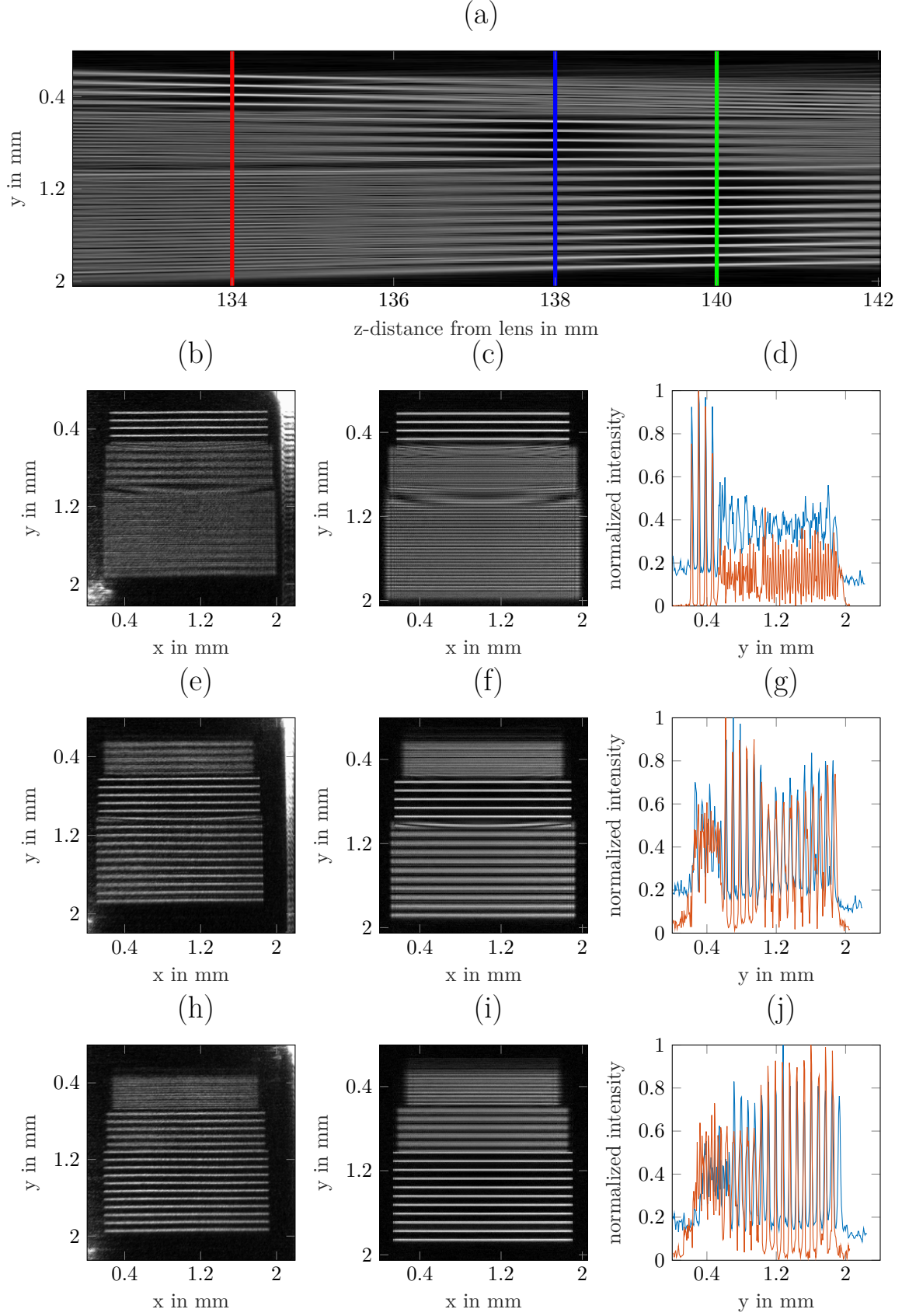


Figure 4.17: Analysis of 3D projection in experiment and simulation by AS propagation - (a) simulated side view of focal planes, the red, blue and green lines mark the three focal planes of the projection; (b),(e),(f) experimental cross section of the focal planes; (c),(f),(i) simulated cross section of the focal planes; (d),(g),(j) sliced view in the three focal planes, comparison of contrast of experimental (light blue) and simulated images (brown).

4.4 Summary of Chapter 4

In this chapter, the aim was to develop a hologram calculation algorithm that allows for speckle-reduced projection of 3D patterns. For this, the quadratic phase hologram calculation methods is used. The fundamental setup is laid out, the calculation of the quadratic phase factor is derived, and the advantages and drawbacks of the method are discussed. For optimization of the algorithm variations and their parameters, test images are chosen, then the input parameters and target criteria are defined, and simulations are conducted for comparison of the algorithm variations and for optimization of the input parameters. The simulations are validated with experiments. The extension of the algorithm to 3D projection with short distance propagation steps is described, and also simulations and experiments are conducted to show the validity of the 3D projection method. In conclusion, the algorithm variations developed in this chapter allow for a speckle-reduced 3D projection of arbitrary pixelated patterns that can be applied for maskless holographic lithography on nonplanar surfaces.

5

Optical setup for lithographic projection and surface measurement

This section contains the optical system design for 3D pattern projection and integrated surface measurement using the SLM described and characterized in Chapter 3 and the CGH calculation methods described in Chapter 4. The system is designed for imaging of the patterns on the photoresist to enable the lithography tests in Chapter 6.

First, the basic required elements are chosen, including the method for separation of the projection from the zero order. Then, the projection system is designed with the aim of submicrometer lateral resolution. The need for a surface measurement method arises because the photoresist layer must be positioned in focus for correct exposure of patterns, which is especially challenging in the case of nonplanar substrates. Thus, an optical surface measurement method that uses the SLMs phase modulation is integrated into the setup and its capabilities are evaluated.

Figure 5.1 shows the final lab setup; its optical subsystems are designed in the following subsections: the light path for structuring in section 5.3, and the measurement light path in section 5.4.

5.1 Fundamental design choices

For the choice and characterization of the SLM, chapter 3 is referenced. In this section, the further basic design choices that influence the rest of the system are elaborated. The light source and the hologram projection method (near-/far field) are important choices for the system, thus the considerations of their relevant parameters and the basic projection setup are explained.

Light source

A laser is chosen as the light source because coherent light is required for holographic projection with high contrast and sharp edges, which is desired in microlithography.

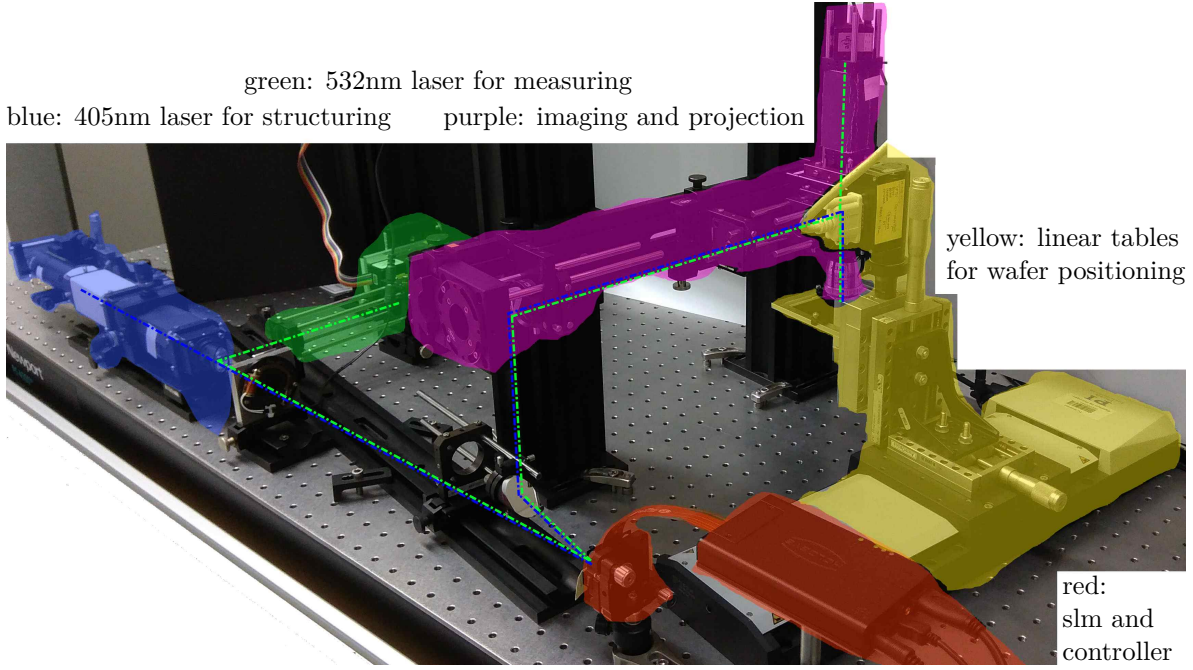


Figure 5.1: Optical laboratory setup Blue dash-dotted line: light path structuring laser; Green dash-dotted line: light path measuring laser. Detailed views of subsystems are available in Fig. 5.4 and Fig. 5.5.

The continuous wave (CW) laser diode "Thorlabs LDM405" is used with an output power of 5mW and a wavelength of 405nm which is in the overlapping region of LCoS starting at around 400nm and higher, and the photoresist sensitivity, which is high at around 400nm (common lithography wavelengths are i-, h-, and g-line at 375, 405, 435nm).

Far field projection

The design choice for the computer generated hologram (CGH) based projection is whether far field (Fraunhofer) or near field (Fresnel) projection is used. For lithographic exposure a high contrast, good uniformity, and no blurred structures are the main demands for the exposure light.

When using a LCoS-SLM for near field holographic projection, the unmodulated light that occurs due to reflections from the cover glass and the interpixel space is a collimated hologram-sized beam. It decreases the available contrast if it overlaps with the projected pattern. Filtering of or compensating for the unmodulated light is very challenging in this case, because of the overlap with the projection, also a live measurement and compensation of the zero order would be required since the zero order intensity depends on the displayed hologram [84].

Thus, to achieve better contrast, far field CGH projection is used, because it allows for filtering of unmodulated zero order light from the SLM with an aperture, see also section 3.2.2.

Because this intermediate projection plane with the aperture can not be directly used for photoresist exposure, the pattern is then reimaged, also allowing for further demagnification of the projection to achieve small feature sizes.

5.2 Off-axis projection and compensation of off-axis intensity gradient

In far field holographic projection, the unmodulated light forms a high intensity focal spot at the location of the projection, see chapter 3.2.2. To spatially separate the projection from the zero order light, a blazed phase profile is added to the hologram phase in order to shift the projection laterally away from the zero order spot. In the lithography experiments, the zero order light is then filtered with an aperture and the projection is reimaged.

Fig. 5.2 illustrates the effect of decreasing off-axis intensity and the further amplification of the effect by off-axis projection for separation of the projection from the zero order light.

Since the projection intensity decreases with increasing distance to the zero order, compensation is required for a constant intensity of the projection. This can be done by multiplication of the target intensity with an inverted sinc^2 function before hologram calculation, see chapter 3.2.6.

The sinc^2 intensity distribution is calculated in pixel coordinates m, n for easier inclusion into hologram calculation algorithms

$$S(m, n) = \text{sinc}^2\left(m \frac{\Delta_x}{s_{hx}}\right) \text{sinc}^2\left(n \frac{\Delta_y}{s_{hy}}\right) \quad (5.1)$$

with the holograms spatial extent s_h and sampling interval Δ_x and the sinc function defined as

$$\text{sinc}(a) = \frac{\sin(\pi \cdot a)}{\pi \cdot a}. \quad (5.2)$$

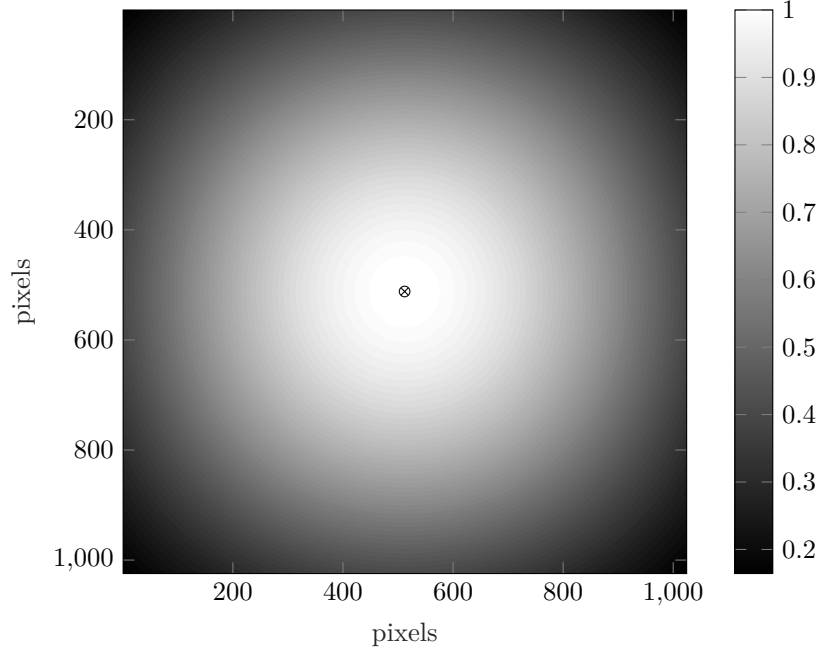


Figure 5.2: Off-axis intensity limited by sinc^2 function - Visualization of the sinc^2 function limiting the intensity of the projection in pixel coordinates for a 1024×1024 pixels sized far field hologram in normalized intensity, \otimes : zero order location.

5.3 Optical system for small feature projection

This section describes the optical system design to achieve the desired demagnification of patterns for the curing of photoresist. Fig. 5.3 shows the basic schematic of far field holographic projection with an aperture for zero order filtering, and a reimaging of the projection with a large demagnification. The aim is to achieve pattern projection at $1\mu\text{m}$ or submicrometer resolution on an area as large as possible. The imaging components are chosen systematically and the performance limits of the system are discussed.

5.3.1 Choice of objective and lenses

The first requirement for the objective is to enable projection at the desired resolution, in order to potentially achieve the structure sizes from literature that are listed in section 2.1.3, a diffraction limited resolution of $<1\mu\text{m}$ is desired. The Rayleigh resolution limit for coherent light [105, 106] can be used to approximately calculate the required NA without requiring the process dependent factor from Eq. (2.1)

$$R = \frac{0.82 \cdot 405\text{nm}}{\text{NA}} \quad (5.3)$$

with R resolvable structure size. A NA of 0.6 results in 554nm diffraction limited resolution which should not impair the writing of structures at $1\mu\text{m}$, thus the numerical aperture of the objective should be around 0.6 or higher.

Further requirements are given by the general settings of the optical setup. In this setup, for projection of small structures on a substrate coated with photoresist, the objective should be corrected for usage without a cover glass covering the projection. The working distance should be at least 1mm, so that nonplanar substrates can be placed in focus without mechanical collision with the objective.

The requirements to the objective are summarized in the following:

- corrected for projection from infinity with no cover glass
- working distance $>1\text{mm}$
- numerical aperture >0.6

The microscope objective "Zeiss LD Plan-Neofluar 63x/0.75" is chosen. Its parameters are the following:

- corrected for imaging to infinity without cover glass
- field of view diameter of $315\mu\text{m}$
- numerical aperture of 0.75
- working distance 2.2mm if used without cover glass

The focal length of the objective f_{obj} is calculated by division of the focal length f_{tl} of the tube lens used for this objective by the nominal magnification of the objective

$$f_{obj} = \frac{f_{tl}}{63} = \frac{165\text{mm}}{63} = 2.619\text{mm} \quad (5.4)$$

For choice of the further lenses f_1 and f_2 , the hologram size and the entrance pupil of the objective have to be matched. The maximum spatial extent of the square hologram is the diagonal w , calculated from the pixel size of $8\mu\text{m}$ and the hologram edge length in pixels of 1024

$$w = \sqrt{2} \cdot 1024 \cdot 8\mu\text{m} = 11.585\text{mm}. \quad (5.5)$$

For illumination with a plane wave (on axis), the usable entrance pupil diameter of the objective can be calculated from the NA and the focal length f_{obj}

$$\theta = \sin^{-1}(\text{NA}) \Rightarrow r_{pupil} = f_{obj} \cdot \tan(\theta) = 2.969\text{mm} \Rightarrow d_{pupil} = 5.939\text{mm}. \quad (5.6)$$

The minimum ratio of f_1 and f_2 can then be determined

$$\frac{w}{d_{pupil}} = 1.95 \leq \frac{f_1}{f_2}. \quad (5.7)$$

For f_2 , a further requirement is to leave enough space for a beam splitter in between the lens and the objective, which will be added in section 5.4. Thus,

- $f_2 = 100\text{mm}$ and
- $f_1 = 200\text{mm}$

are chosen.

The size of the aperture should be chosen so that only the projected pattern passes. Its edge length can be calculated from the wavelength λ , focal length f_1 , the hologram size s_h , and the projection size in pixels M according to Eq. (4.4) for a square projection sized $M = 256$ pixels

$$s_p = \frac{M\lambda f}{s_h} = \frac{256 \cdot 405\text{nm} \cdot 200\text{mm}}{1024 \cdot 8\mu\text{m}} = 2.53\text{mm} \quad (5.8)$$

According to Eq. (2.2), a minimum depth of focus (DOF) of

$$\frac{405\text{nm}}{0.75^2} \approx 720\text{nm} \quad (5.9)$$

is estimated, however it is expected to be larger because the projected structures are larger than the diffraction limit and because the objective aperture is slightly underfilled.

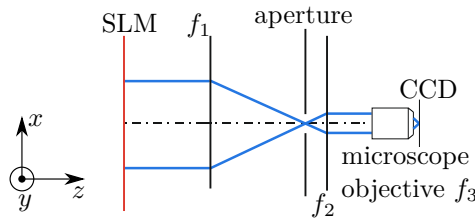


Figure 5.3: Schematic of projection system - The pattern projected by the SLM is imaged in the aperture plane with lens f_1 and is re-imaged and demagnified with lens f_2 and objective f_3 either on a camera sensor (CCD) as depicted or on a substrate coated with photoresist.

5.3.2 Limitations of lateral resolution

In this section, the three different limitations on the lateral projection resolution are identified and addressed. This is done to assess the achievable resolution of the system.

1. Sampling

The sampling interval (pixel size of the projection) for the setup shown in Fig. 5.3 can be calculated according to Eq. (4.3) from the spatial extent of the hologram s_h when displayed on the SLM, the system focal length f_1 for the intermediate projection plane, λ , and additionally f_2, f_3 for the demagnified final projection

$$\Delta_{xproj} = \frac{\lambda \cdot f_1}{s_h} \cdot \frac{f_3}{f_2} = \frac{405\text{nm} \cdot 200\text{mm}}{1024 \cdot 8\mu\text{m}} \cdot \frac{2.619\text{mm}}{100\text{mm}} = 259\text{nm} \quad (5.10)$$

2. Diffraction limit

The Rayleigh resolution limit for coherent light [105, 106] can be calculated

$$R = \frac{0.82 \cdot \lambda}{\text{NA}} = \frac{0.82 \cdot 405\text{nm}}{0.6} = 554\text{nm} \quad (5.11)$$

with λ wavelength and NA effective numerical aperture. It is noted that for projection applications, the effective NA decreases when the designated objective aperture is underfilled by the illuminating light. The value 0.6 is chosen for the NA because the scalar diffraction approximation is valid up to this value, as noted in section 2.3.1.

3. Optical aberrations

The presence of large aberrations can also decrease projection quality by warping the size and/or shape of each focal spot. In this setup, the main source of aberrations is the LCoS-backplane. To quantify the aberrations, measurements with a wavefront sensor were conducted. Using the Maréchal criterion [107], a RMS wavefront error of 0.072λ is small enough to be considered diffraction limited performance. Measurements of the RMS wavefront error to 0.093λ from section 3.3.3 with aberration compensation confirm minor aberration influence on projection quality.

5.4 Integrated optical surface measurement system

In order to conduct a surface measurement for lithography, it is advantageous to be able to measure the surface with the same optical system used for structuring and to require the addition of as few components as necessary. Here, the phase modulating function of the SLM presents an opportunity for flexible projection of patterns that enable surface measurement.

In this section, the design, implementation, and characterization of a surface measurement system into the optical lithography system are described. First, to be able to measure a surface coated with photoresist without curing it, light of a suitable wavelength must be coupled into the system. Then, for signal detection, a sensor is added to the system, in this case the reflected light is coupled onto a camera chip with a beam splitter. Furthermore, an appropriate pattern must be projected by the LCoS to allow for a surface measurement with adequate resolution. Finally, a scanning motion is required to allow the system to find the actual surface

position. For characterization of the measurement system, first the measurement uncertainty for a mechanical scanning and the z -axis offset of the two lasers are determined, then the maximum surface tilt that can be measured is determined.

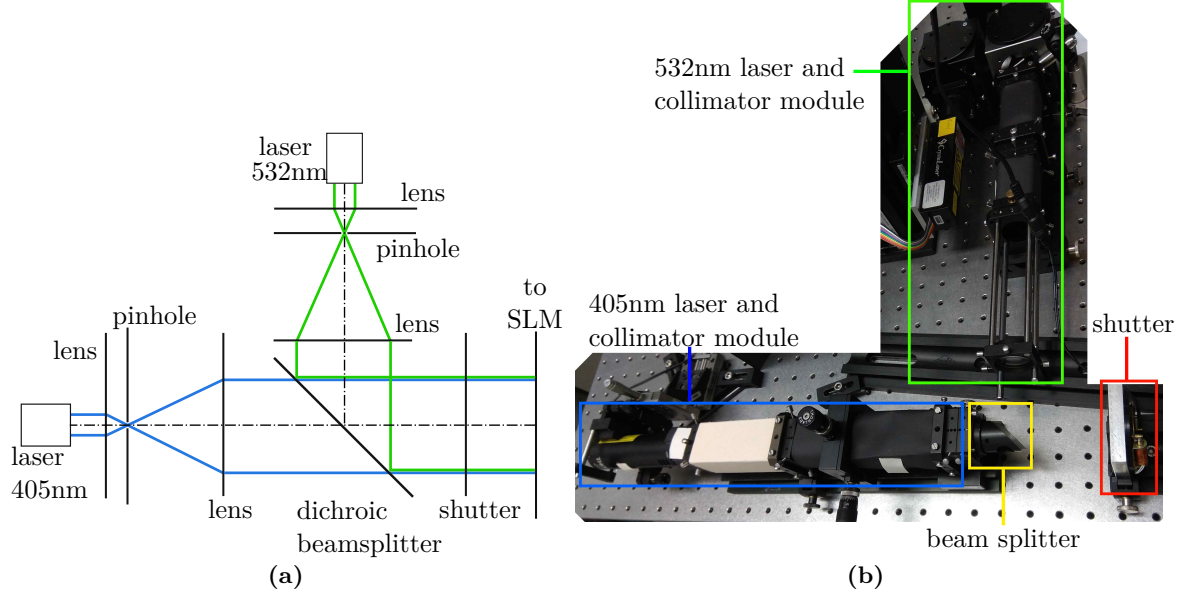


Figure 5.4: Schematic of illumination optical subsystem - (a) Schematic of the illumination system. blue: light path structuring laser, green: light path measuring laser. (b) Photograph of the illumination system. blue: 405nm laser and collimator module, green: 532nm laser and collimator module, yellow: dichroic beamsplitter, red: shutter.

To allow the measurement of the local surface position without curing the photoresist in the process, a second laser ($\lambda=532\text{nm}$, CrystaLaser CL532-005-S) is used to illuminate the SLM, see Fig. 5.4. Commonly used photoresists are much less sensitive to light at this wavelength [1].

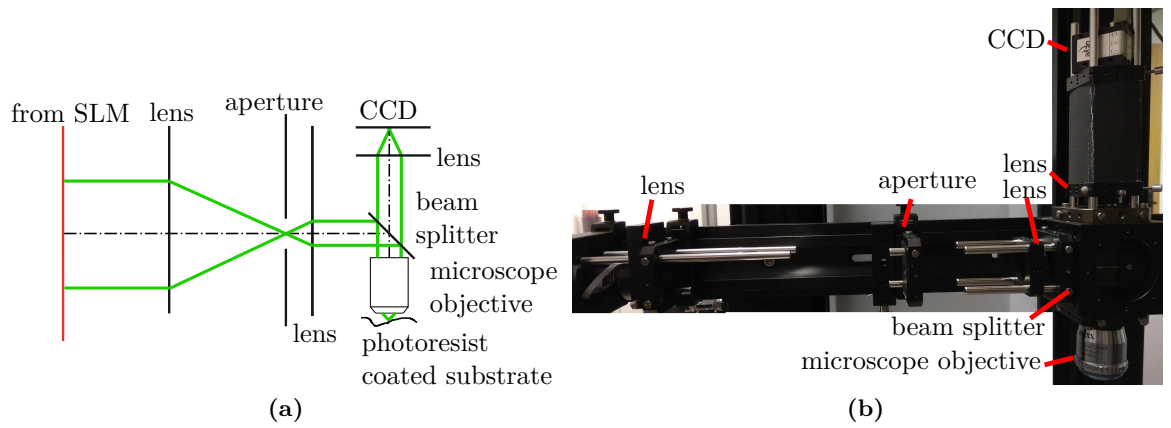


Figure 5.5: Schematic of imaging and measurement subsystem - (a) Schematic. The light path depicted is for projection of one focal spot in order to visualize the re-imaging function from substrate to camera sensor. (b) Photograph.

Additionally, a sensor needs to be added to the system. Fig. 5.5 shows a schematic and a photograph of the system, whereas the projection present on the photoresist is re-imaged on a camera sensor "ids UI1540SE-M-GL" with a beam splitter and a $4f$ -system. Because of the

low surface roughness of photoresists, specular reflection occurs. When the surface is in focus, the projection plane is re-imaged on the camera sensor and the projected pattern is visible on the sensor.

A similar SLM-based setup for surface measurement as an autofocus functionality of a lithography system is demonstrated in [108], however it uses amplitude modulation and instead of holographic projection, thus it works only on plane surfaces, and can measure only an average focal position over the full illuminated field.

5.4.1 Choice of projected pattern and hologram phase for measurement

For projection onto 3D surfaces such as lenses or freeform surfaces with slowly varying surface topography, high lateral resolution of the measurement is not strictly necessary. Thus, an array of focal spots is to be projected on the surface. This allows for a relatively simple detection of absolute surface positions by evaluation of the maximum brightness of the spots during a z -scan. The far field projection setup is used, so various methods for projection of a focal spot array can be used. Several different types of phasemaps that can be considered to be displayed on the SLM are demonstrated in Fig. 5.6.

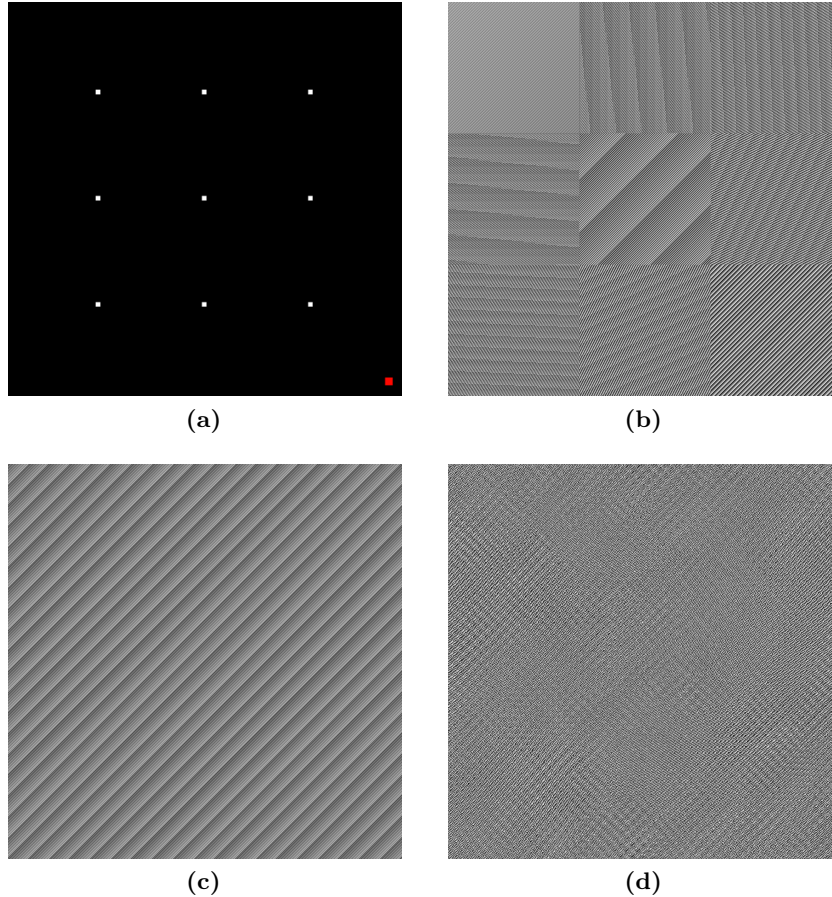


Figure 5.6: Holograms for measurement projection - (a) target projection pattern, zero order location marked in red. Different hologram phases for realization of pattern: (b) array of blaze phases, (c) one blaze phase, sequentially changed, (d) random phase hologram

Segmented blaze phases are influenced by local aberrations and have smaller apertures, decreasing the depth resolution. The high depth of focus of the quadratic phase hologram

makes it unsuitable for this measurement. The sequential display of blazed phases has advantages over the previously mentioned types, but the massively increased time demand due to nonparallelized measurement makes it unsuitable for this task.

A random phase hologram is used because it uses the full aperture to illuminate each focal spot, so a low depth of focus results which increases the depth resolution. It also causes an averaging of local residual aberrations, minimizing their effect. The illumination from the full aperture is also useful for allowing measurements on higher tilted surfaces, this will be described in more detail in section 5.4.4.

5.4.2 Surface scanning methods

To find the location of the surface to be measured, either the focal plane or the surface has to be moved along the z -axis by scanning. For simplicity of the depiction, no tilted surfaces are displayed. The effects of surface tilt are discussed in section 5.4.4.

When mechanically scanning, re-imaging of the focal spot only occurs when the surface coincides with the focal spot, see 5.7. The mechanical movement then directly corresponds to the distance from the surface to the focal plane of the objective. This allows a direct calculation of the surface position from the position of the linear stage.

When optical scanning by shifting the focus with the SLM, it needs to be considered that the focal spot has to be moved twice the distance from the surface to the focal plane to be in focus on the camera, see Fig. 5.8.

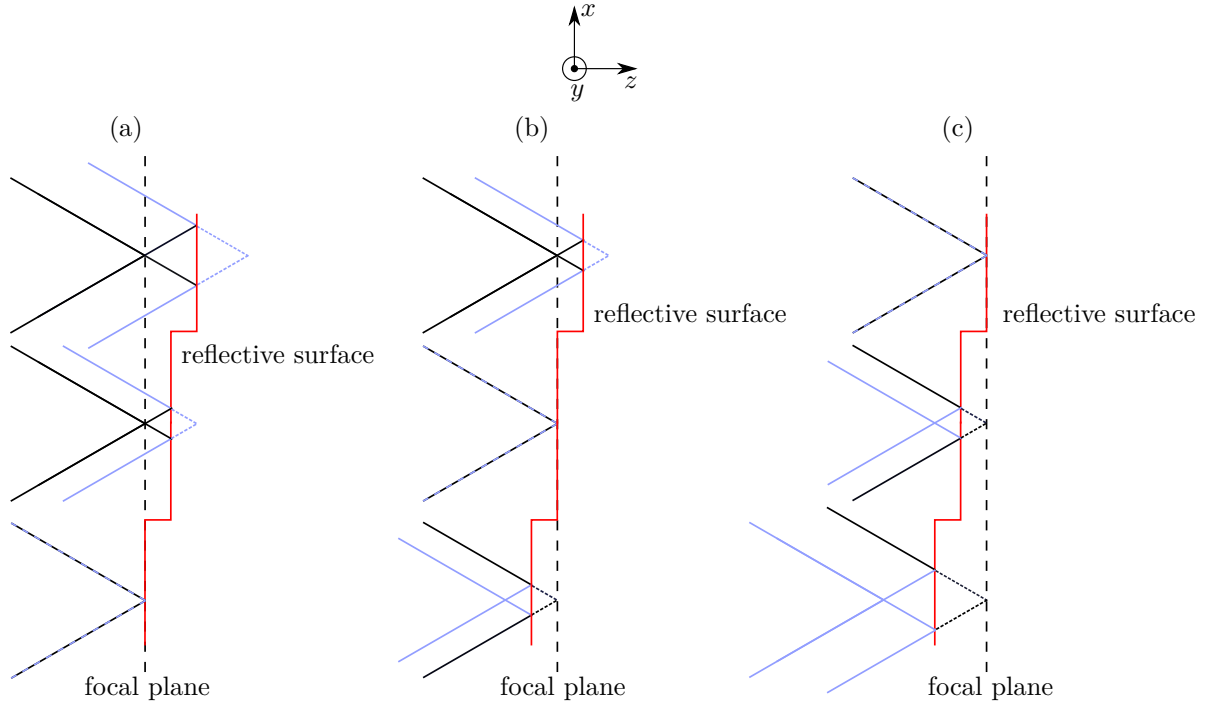


Figure 5.7: Mechanical scanning for surface measurement. (a) bottom spot in focus, (b) middle spot in focus, (c) top spot in focus. red: reflective surface. black: projected light. blue: reflected light. focal plane: plane that is reimaged on the camera sensor.

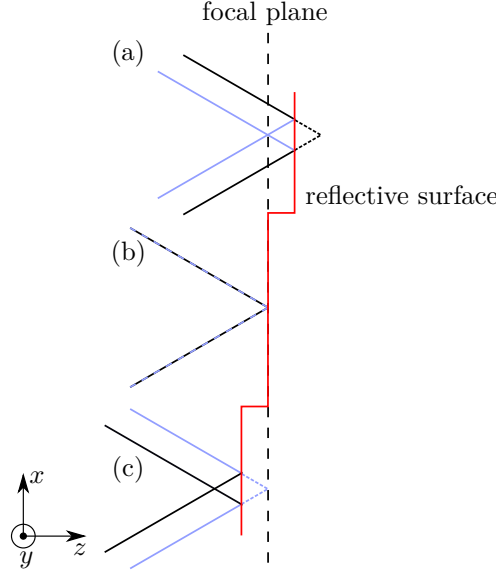


Figure 5.8: Optical scanning for surface measurement. When optically scanning the surface, shifting the focus by twice the distance of the surface to the focal plane is needed for reimagining of the focal spots. (b) surface in focal plane of objective (a), (c) surface out of focus and optically refocused by movement of the focal spot along the z -axis. red: reflective surface. black: projected light. blue: reflected light. focal plane: plane that is reimaged on the camera sensor.

5.4.3 Measurement resolution and axial offset of the lasers

The measurement resolution (z -resolution) is required to be lower than the depth of focus of the lithographic pattern (estimated $\approx 1\mu\text{m}$), so several hundreds of nanometers are estimated to be sufficient.

In principle, the z -resolution is limited by the step size of the linear stage for mechanical scanning, and by the smallest achievable propagation distance for optical scanning.

To determine the focal position measurement uncertainty and the focal plane distance of both lasers, several measurements are conducted with one focal spot on a flat glass surface. The measurement is repeated five times with different step sizes for the linear table and the mean and the standard deviation for the measured focal position are calculated for both lasers, see Fig. 5.9.

5.4.4 System limit: surface tilt

Given that nonplanar surfaces can contain sections that are tilted with respect to a plane transversal to the optical axis, an investigation is conducted to determine the maximum surface tilt that can still be measured. When a tilt is introduced to the surface under test, the efficiency of light coupling back into the objective is decreased. The effect depends on the effective numerical aperture (NA) and the pattern projection method.

The choice of the random phase hologram in section 5.4.1 allows for increased coupling of reflected light from tilted surfaces. Since every pixel of the measurement projection is illuminated by the full hologram, a large proportion of the objective aperture is used. Every spot is thus illuminated with a large effective NA, albeit with decreased efficiency. Light is then reflected from the reflective surface in a wider angle, increasing the range of surface tilt at which light can be coupled back into the objective aperture, see Fig. 5.10. The maximum tilt

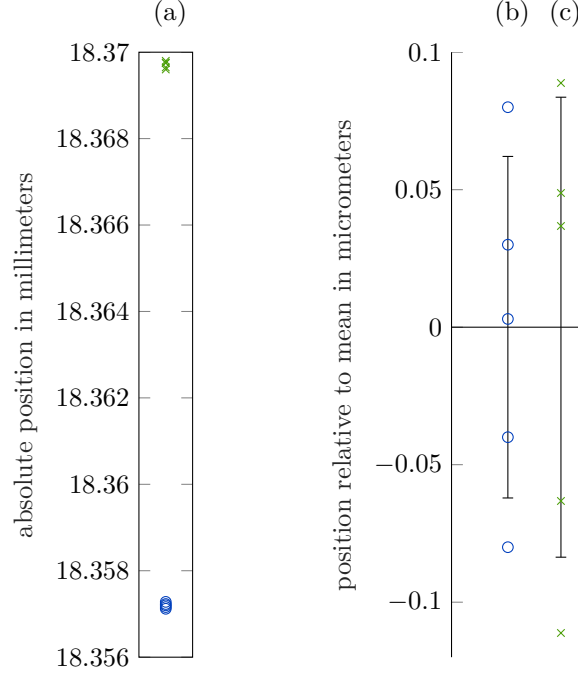


Figure 5.9: Surface measurements by focal spot intensity evaluation (a) absolute positions as measured by mechanical scanning with linear table "PI M-125.11". green 'x': 532nm laser; blue 'o': 405nm laser. (b) measurements relative to the mean with the 405nm laser, standard deviation: 124nm. (c) measurements relative to the mean with the 532nm laser, standard deviation: 167nm. Error bars show the standard deviation. The mean laser offset calculated from the measurements is 12.5 μ m.

angle ψ_s of the surface can not exceed half of the opening angle of the objective θ , however for $\psi_s > \theta/2$ the efficiency decreases drastically due to the lower overlap area of the light cones, thus measurement would require a long integration time or an expensive low light sensor and would thus be unfeasible.

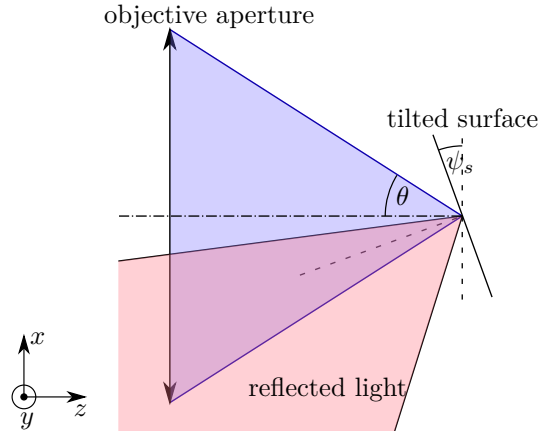


Figure 5.10: Schematic for measurement of tilted surfaces. Surface measurement of locally tilted surface with one focal spot: Loss of reflected light available for the measurement.

5.5 Summary of Chapter 5

In this chapter, an optical system is realized with the goal to design a system capable of projection with submicrometer lateral resolution and an integrated parallelized surface measurement method for in-focus positioning of nonplanar substrates.

First, the basic setup is laid out, then the method for removal of zero order light is described. This is done by laterally shifting the projection and filtering of the zero order light with an aperture, and compensation of the off-axis intensity gradient is done by multiplication of the target intensity with the inverted sinc^2 function. Furthermore, the objective and lenses for the desired demagnification of the pattern are chosen systematically and the limitations of the lateral resolution of the system are discussed.

The surface measurement is required for in-focus projection of patterns. To facilitate this, the projection of an appropriate pattern with the SLM and a scanning of the surface are required. An optical and a mechanical scanning method are discussed. For the measurement pattern, a focal spot array is chosen because it provides a spatially resolved measurement and a high intensity on the sensor. For projection of the focal spot array with the phase-only SLM, a random-phase hologram has major advantages because each focal spot is illuminated from the full hologram, providing less susceptibility to surface tilt and a low depth of focus which is beneficial for the axial measurement resolution.

6

Lithography experiments

The system designed in this work aims to enable holographic maskless lithography of arbitrary pixelized binary structures on nonplanar surfaces with single micrometer / submicrometer resolution. The photoresist exposures are conducted using the LCoS-SLM device for hologram display with the calibrations and corrections done in Chapter 3, the 2D and 3D hologram calculation methods developed in Chapter 4, and the optical system for projection and surface measurement developed in Chapter 5.

The photoresist patterning tests are conducted in order to characterize the patterning performance of the system, and demonstrate surface measurement performance. Unless otherwise noted, the exposures are done with a AZ@ECI 3012 photoresist with a layer thickness of $1\mu\text{m}$ on fused silica wafers.

The linear tables for substrate positioning are "PI M-125.11" for the z -axis and "PI M-521.DD" for the x -axis which have encoders with submicrometer resolution, considered sufficient for in-focus positioning of the patterns which have $\approx 1\mu\text{m}$ DOF.

The full procedure for measurement of the substrate position and exposure of patterns into the resist is described in Fig. 6.1, whereas the preliminary steps for positioning of the substrate in or near the focal plane are already done.

6.1 Determination of correct dose and exposure time

The dose in lithography is the exposure energy per area that a photoresist is subjected to. It can be calculated by multiplication of incident power per area (irradiance, in lithography commonly called intensity) with exposure time. In this section the required dose for correct exposure of the photoresist is determined. First, the intensity is calculated by measurement of power and illuminated area. For this, the off-axis intensity gradient correction from section 5.2 has to be applied for a uniform illumination of the area. Then, an approximate exposure time is calculated with an estimation of the photoresists required dose. Finally, lithographic tests with variation of the exposure time are conducted to find the required exposure time.

In order to determine the necessary exposure time to achieve high contrast in the developed binary photoresist, first a power measurement is conducted with a "Coherent PM USB UV/VIS"

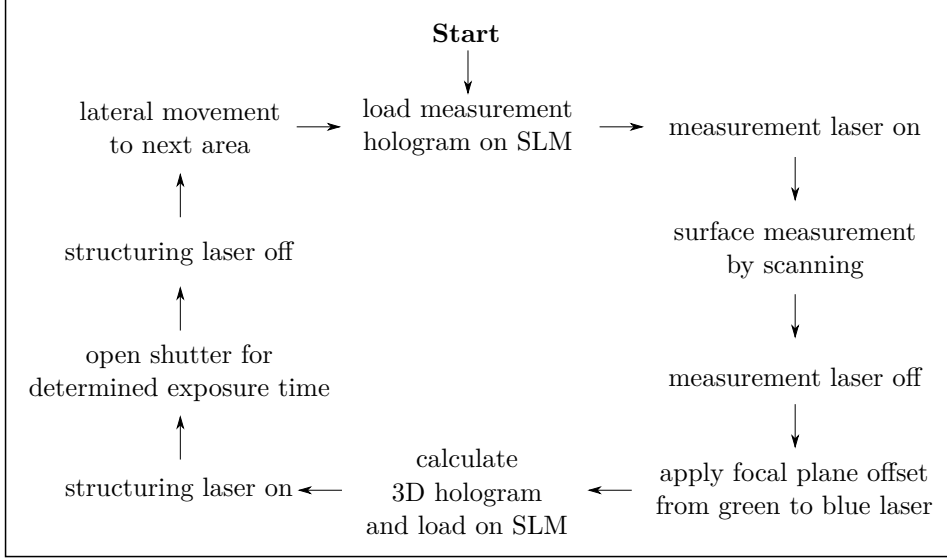


Figure 6.1: Schematic of measurement and structuring process.

power sensor and a measurement of the size of the fully illuminated projection is done with a "ids UI1492LE-M" camera chip (pixel size $1.67\mu\text{m}$ and resolution 3840×2748). Because of the nature of holographic projection, the incident intensity (in mW/cm^2) can be determined only for one set of input parameters of the hologram calculation:

- hologram calculation method,
- scaling factor,
- size of patterning field in pixels (all described in Chapter 4),
- lateral shift from the zero order due to blazed phase (described in section 5.2),

and changes to any of these parameters can change the intensity, which may then require an adjustment of the exposure time. Using the phase restricted hologram calculation algorithm from Fig. 4.3 with a scaling factor of 30.000 for the amplitude, a projection size of 256×256 pixels, and a blaze factor resulting in a lateral shift of 172 pixels in both x - and y -direction for separation from the zero order, holograms for exposure are calculated. From the measured power and area the incident intensity can be calculated

$$I = \frac{0.01\text{mW}}{4.45 \cdot 10^{-5}\text{cm}^2} = 225 \frac{\text{mW}}{\text{cm}^2}. \quad (6.1)$$

Information for exposure with a wavelength of 405nm is not included in the photoresist datasheet, so a first estimate of exposure time is calculated and a parameter variation of the exposure time is conducted to find the optimum dosage for good contrast in the photoresist.

The approximate exposure time is calculated from the intensity and the estimated required dosage for the AZ®ECI 3012 photoresist:

$$t_e = \frac{\text{dose}}{I} \approx \frac{72\text{mJ}/\text{cm}^2}{225\text{mW}/\text{cm}^2} \approx 0.32\text{s} \quad (6.2)$$

Tests are then conducted with an photoresist at $1\mu\text{m}$ layer thickness, results are displayed in Fig. 6.3.

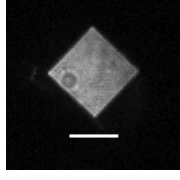


Figure 6.2: Measurement of projection size - Camera image of a projection resulting from hologram calculation with a target pattern of constant intensity. The size of the illuminated area is $\approx 4.45 \cdot 10^{-5} \text{cm}^2$. Scale bar is $50\mu\text{m}$.

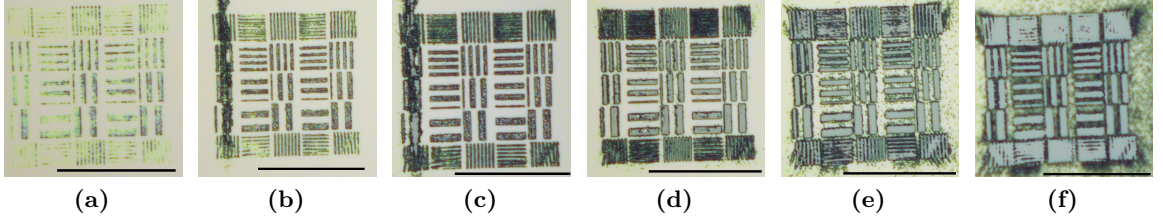


Figure 6.3: Variation of exposure time - Photoresist exposed with a dose of (a) 3.75 (b) 7.5 (c) 15 (d) 30 (e) 60 (f) 120 mJ/cm^2 . It can be seen that maximum contrast is obtained at a dose of around 30 mJ/cm^2 . The additional speckle contrast in some of the pictures, especially visible in (b), (c), and (f) is caused by incomplete filtering of the zero order. Scale bars are $50\mu\text{m}$.

6.2 Determination of projection resolution

In order to determine the linewidths that can be achieved with the system, a photoresist exposure is conducted with correct focus, exposure time, and blocking of the zero order. Fig. 6.4 shows the pattern, demonstrating that the smallest lines have $\approx 1\mu\text{m}$ linewidth. It is apparent that the pattern is in focus, demonstrating the correctness of the surface measurement and the calculated offset of the lasers described in section 5.4, Fig. 5.9. Also, Fig. 6.4 (a) demonstrates that the uniformity of the patterns intensity is sufficient for a mostly uniform structuring of the full pattern.

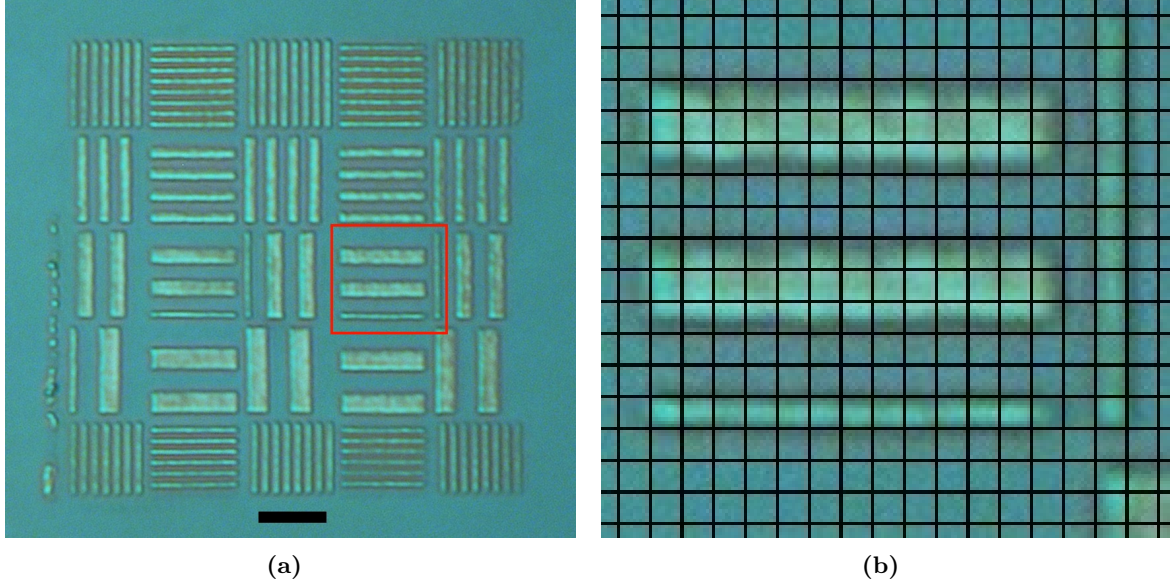


Figure 6.4: Pattern in Photoresist for determination of resolution - (a) Full view. Scale bar is $10\mu\text{m}$. (b) Detailed view of red rectangle. Overlaid grid has $1\mu\text{m}$ periodicity. Width of the smallest lines is thus $\approx 1\mu\text{m}$.

To demonstrate the effect of the optimizations and improvements achieved in this work, an image of a photoresist patterned with standard methods and no corrections applied is included in Fig. 6.5, whereas AZ@1518 photoresist with a layer thickness of $2\mu\text{m}$ is used, average dose is $80\text{mJ}/\text{cm}^2$. The standard speckle-inducing random phase IFTA algorithm is used for hologram calculation, and neither sinc^2 intensity gradient correction nor aberration correction are applied.

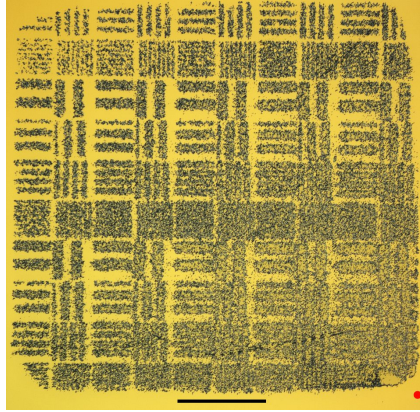


Figure 6.5: Pattern in Photoresist without corrections and optimizations - The speckle contrast completely deteriorates the projected pattern. Moreover, the intensity decrease with increased distance to the zero order is clearly visible. Red dot is zero order location (filtered by aperture). Scale bar is $500\mu\text{m}$.

6.3 Defocus variation

In order to determine the effect of defocused projection on the resulting pattern in photoresist, a parameter variation of the defocus distance is conducted. In Fig. 6.6 the high DOF can be seen for the larger structures, however the smaller structures with a linewidth of $\approx 1\mu\text{m}$

are much more sensitive to defocus. Comparing Fig. 6.6 (d) to (h), it is evident that the small structures have different focal planes, depending on their orientation and location. This indicates aberrations in the optical system, especially astigmatism [1].

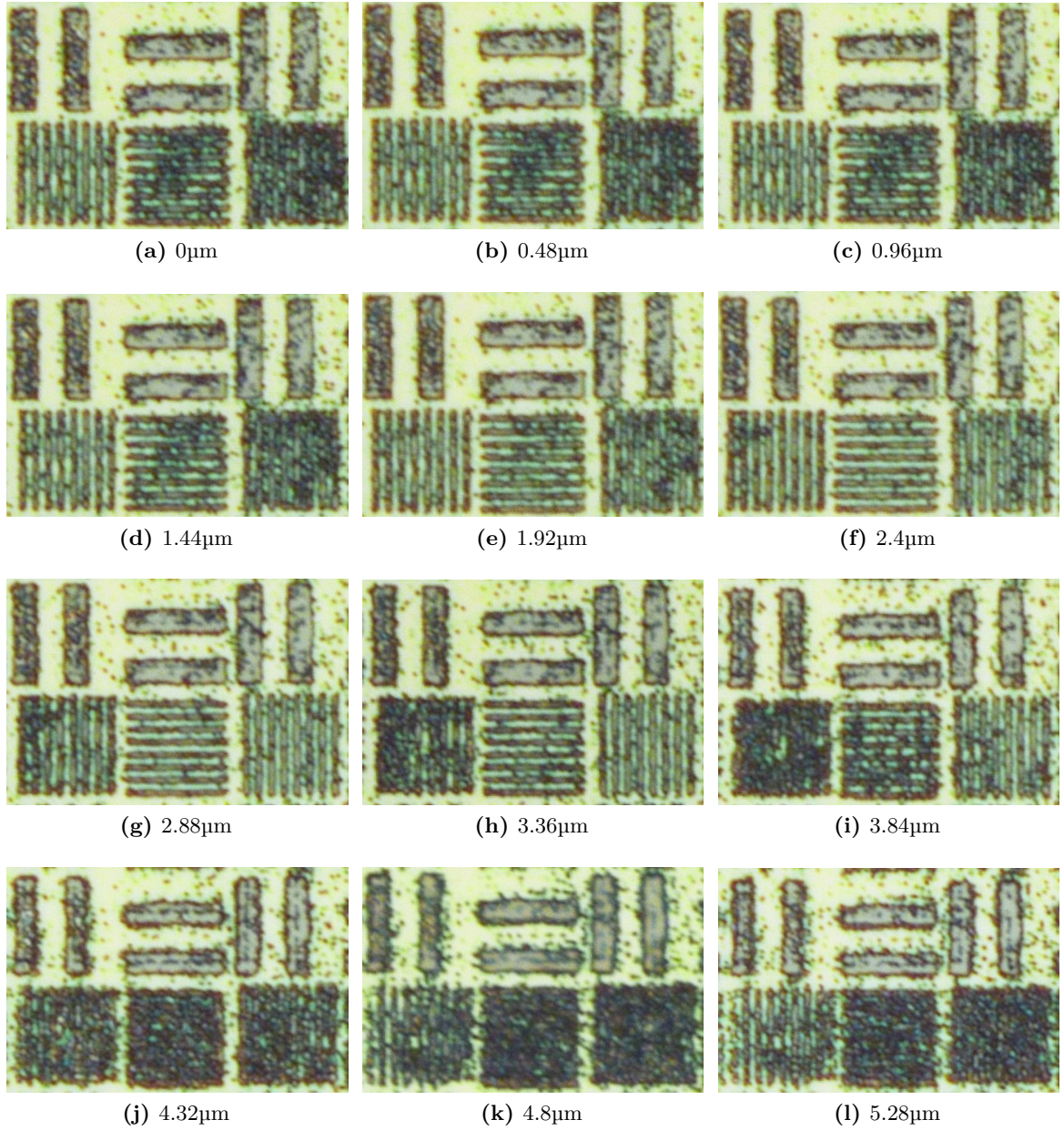


Figure 6.6: Variation of defocus - Detailed view of patterns in photoresist with the defocus varied in steps of 480 μm . The additional speckle contrast is caused by incomplete filtering of the zero order. Images are sized 42 μm ×28 μm each.

6.4 Summary of Chapter 6

In this chapter lithographic tests are conducted to characterize the projection system because the feature sizes are too small to be measured with a camera sensor directly. For this, first a parameter variation of the exposure time is done with which the correct exposure time is determined for a specific set of hologram calculation parameters. Then, the feature size of the written pattern is analyzed with a microscope to determine the resolution achieved

6. Lithography experiments

with the system. Finally, a variation of the defocus of the photoresist shows the effect of out-of-focus projection on the patterning result, which is larger on smaller features.

7

Summary and Outlook

In this work, a system for flexible (maskless) holographic lithography on nonplanar surfaces was designed. In order to achieve the 3D projection of micrometer-sized patterns, the system consists of an optimized hologram calculation method, a calibrated device for hologram display, and an optical system that allows the projection of small features.

For the hologram calculation, the trade-off is between diffraction efficiency, calculation time, and projection quality. This work uses a quadratic phase hologram calculation which is both fast and has good projection quality without temporal averaging, at the cost however of reduced diffraction efficiency. Simulations are conducted to optimize the algorithm increasing both quality and efficiency. Due to the defined phase of the projection, extension to 3D projection is possible with multi-plane propagation.

For the hologram display, a spatial light modulator (SLM) with the liquid crystal on silicon (LCoS) technology is chosen. This technology allows for phase-only modulation with a high space-bandwidth product (SBP), however some effects of the technology negatively affect the phase modulation, such as crosstalk and backplane aberrations. Both effects are measured and in the case of backplane aberrations, the required compensation of the effect is applied.

For design of the optical system, first the major elements were chosen according to the requirements: The laser, the SLM, and the type of projection setup. The system is designed in a way that a submicrometer lateral resolution is achievable. In order to provide a solution for the depth of focus (DOF) issue in lithography on nonplanar surfaces, the 3D projection capability of computer generated hologram (CGH) is combined with an optical surface measurement method. The surface measurement is integrated into the lithographic projection system.

The major challenge for measurement of tilted reflective surfaces through an objective is the decreased light efficiency with increased surface tilt, which is addressed in the design. Because the phase modulation of the SLM can be used for surface measurement as well, any phase distribution can be used. The projection of a focal spot array offers a high signal level and parallelized measurement. It is projected with a random phase hologram because the random phase causes a low DOF, resulting in better axial measurement resolution and also causes each focal spot to be illuminated from the full hologram aperture, decreasing susceptibility of

the measurement system to surface tilt. A validation of the system is done with lithographic structuring tests, which confirm the single micrometer resolution and demonstrate the large DOF of the hologram calculation method at least for the larger projected structures (linewidth of $\approx 4\mu\text{m}$).

The next steps are the measurement and structuring on tilted planar surfaces and curved surfaces, to demonstrate that the refocusing by hologram calculation can move out-of-focus pattern segments back in focus. In addition, the requirements for a correct stitching of pattern segments are investigated. Further approaches for optimization of the projection system are an automation of the measurement and lithography process in order to reduce the processing time, and usage of a polarizing beam splitter before the objective with a $\lambda/4$ -plate for the measurement wavelength between the objective and the beam splitter. This can increase the intensity for structuring by a factor of two and the intensity available for measurements by a factor of four.

In conclusion, a hologram calculation algorithm that allows for quick calculation of speckle-reduced 3D holograms was developed. Combined with an appropriately calibrated SLM for hologram display and a demagnifying optical system it allows for the patterning of micrometer-sized structures in parallel in photoresist. To the authors knowledge, this resolution has not yet been demonstrated with a SLM-based holographic lithography setup for arbitrary structure shapes without usage of an immersion objective or multi-photon processes.

Since the 3D projection capabilities of the algorithm have been demonstrated, the system developed in this work provides a basis for the parallelized patterning on nonplanar surfaces.

References

- [1] Harry J. Levinson. *Principles of lithography*. 2nd ed. Vol. PM146. SPIE Press monograph. Bellingham, Wash. (1000 20th St. Bellingham WA 98225-6705 USA): SPIE, 2005. ISBN: 9780819456601. URL: <http://dx.doi.org/10.1117/3.601520>.
- [2] Chris A. Mack. “Resolution and depth of focus in optical lithography”. In: *Micro lithographic Techniques in IC Fabrication*. Ed. by Soon Fatt Yoon, Raymond Yu, and Chris A. Mack. Vol. 3183. SPIE, 1997, pp. 14–27. DOI: 10.1117/12.280550.
- [3] Tor Sandstrom et al. “OML: Optical maskless lithography for economic design prototyping and small-volume production”. In: *Optical Microlithography XVII*. Ed. by Bruce W. Smith. Vol. 5377. SPIE, 2004, pp. 777–787. DOI: 10.1117/12.537391.
- [4] Hans-Christoph Eckstein et al. “High dynamic grayscale lithography with an LED-based micro-image stepper”. In: ed. by Andreas Erdmann and Jongwook Kye. SPIE Proceedings. SPIE, 2016, 97800T. DOI: 10.1117/12.2219099.
- [5] Nathan J. Jenness et al. “Three-dimensional parallel holographic micropatterning using a spatial light modulator”. In: *Optics Express* 16.20 (2008), p. 15942. ISSN: 1094-4087. DOI: 10.1364/OE.16.015942.
- [6] Christoph Bay et al. “Maskless photolithography via holographic optical projection”. In: *Optics Letters* 35.13 (2010), pp. 2230–2232. ISSN: 0146-9592. DOI: 10.1364/OL.35.002230.
- [7] Daniel R. McAdams and Daniel G. Cole. “Using a dwell-time increase to compensate for SLM pixelation-limited diffraction efficiency in DMHL”. In: *Advanced Fabrication Technologies for Micro/Nano Optics and Photonics V*. Ed. by Winston V. Schoenfeld, Raymond C. Rumpf, and Georg von Freymann. Vol. 8249. SPIE, 2012, pp. 302–311. DOI: 10.1117/12.909073.
- [8] Nathan J. Jenness et al. “A versatile diffractive maskless lithography for single-shot and serial microfabrication”. In: *Optics Express* 18.11 (2010), pp. 11754–11762. ISSN: 1094-4087. DOI: 10.1364/OE.18.011754.
- [9] Joshua J. Cowling et al. “Three-dimensional holographic lithography by an iterative algorithm”. In: *Optics Letters* 36.13 (2011), pp. 2495–2497. ISSN: 0146-9592. DOI: 10.1364/OL.36.002495.
- [10] Maxim Shusteff et al. “One-step volumetric additive manufacturing of complex polymer structures”. In: *Science advances* 3.12 (2017). DOI: 10.1126/sciadv.aao5496.

REFERENCES

- [11] A. Maiden et al. “Nonplanar photolithography with computer-generated holograms”. In: *Optics Letters* 30.11 (2005), p. 1300. ISSN: 0146-9592. DOI: 10.1364/OL.30.001300.
- [12] Alan Purvis et al. “Photolithographic patterning of bihelical tracks onto conical substrates”. In: *Journal of Micro/Nanolithography, MEMS, and MOEMS* 6.4 (2007), p. 043015. ISSN: 1932-5150. DOI: 10.1117/1.2824377.
- [13] Joseph W. Goodman. *Introduction to Fourier Optics*. 2. ed. Electromagnetics. New York: McGraw-Hill, 1996. ISBN: 0070242542.
- [14] *Mandrill and Peppers test images*. Retrieved on 13 May 2019. URL: <http://sipi.usc.edu/database/database.php?volume=misc>.
- [15] *Cameraman test image: Copyright Massachusetts Institute of Technology*. Retrieved on 13 May 2019. URL: <https://homepages.cae.wisc.edu/~ece533/images/cameraman.tif>.
- [16] Eugene Hecht. *Optics*. 5. ed. Pearson global edition. Boston, Columbus, and Indianapolis: Pearson, 2017. ISBN: 9780133977226.
- [17] Daniel C. Cole et al. “Derivation and Simulation of Higher Numerical Aperture Scalar Aerial Images”. In: *Japanese Journal of Applied Physics* 31.12S (1992), p. 4110. ISSN: 0021-4922. DOI: 10.1143/JJAP.31.4110.
- [18] Giang-Nam Nguyen et al. “Computationally efficient scalar nonparaxial modeling of optical wave propagation in the far-field”. In: *Applied Optics* 53.10 (2014), pp. 2196–2205. ISSN: 2155-3165. DOI: 10.1364/AO.53.002196.
- [19] Tomasz Kozacki and Konstantinos Falaggis. “Angular spectrum-based wave-propagation method with compact space bandwidth for large propagation distances”. In: *Optics Letters* 40.14 (2015), pp. 3420–3423. ISSN: 0146-9592. DOI: 10.1364/OL.40.003420.
- [20] Kyoji Matsushima and Tomoyoshi Shimobaba. “Band-limited angular spectrum method for numerical simulation of free-space propagation in far and near fields”. In: *Optics Express* 17.22 (2009), pp. 19662–19673. ISSN: 1094-4087. DOI: 10.1364/OE.17.019662.
- [21] Wenhui Zhang, Hao Zhang, and Guofan Jin. “Band-extended angular spectrum method for accurate diffraction calculation in a wide propagation range”. In: *Optics Letters* 45.6 (2020), pp. 1543–1546. ISSN: 0146-9592. DOI: 10.1364/OL.385553.
- [22] Tomasz Kozacki, Konstantinos Falaggis, and Malgorzata Kujawinska. “Computation of diffracted fields for the case of high numerical aperture using the angular spectrum method”. In: *Applied Optics* 51.29 (2012), pp. 7080–7088. ISSN: 2155-3165. DOI: 10.1364/AO.51.007080.
- [23] Fabian Shen and Anbo Wang. “Fast-Fourier-transform based numerical integration method for the Rayleigh-Sommerfeld diffraction formula”. In: *Applied Optics* 45.6 (2006), p. 1102. ISSN: 2155-3165. DOI: 10.1364/AO.45.001102.
- [24] Soheil Mehrabkhani and Thomas Schneider. “Is the Rayleigh-Sommerfeld diffraction always an exact reference for high speed diffraction algorithms?” In: *Optics Express* 25.24 (2017), pp. 30229–30240. ISSN: 1094-4087. DOI: 10.1364/OE.25.030229.

-
- [25] M. A. Seldowitz, J. P. Allebach, and D. W. Sweeney. "Synthesis of digital holograms by direct binary search". In: *Applied Optics* 26.14 (1987), pp. 2788–2798. ISSN: 2155-3165. DOI: 10.1364/AO.26.002788.
 - [26] Brian K. Jennison, Donald W. Sweeney, and Jan P. Allebach. "Efficient design of direct-binary-search computer-generated holograms". In: *Journal of the Optical Society of America A* 8.4 (1991), p. 652. ISSN: 1084-7529. DOI: 10.1364/JOSAA.8.000652.
 - [27] Matthew Clark and Robin Smith. "A direct-search method for the computer design of holograms". In: *Optics Communications* 124.1-2 (1996), pp. 150–164. ISSN: 00304018. DOI: 10.1016/0030-4018(95)00633-8.
 - [28] Hitoshi Tamura and Yasuhiro Torii. "Enhancement of the Lohmann-type computer-generated hologram encoded by direct multilevel search algorithm". In: *Optical Review* 19.3 (2012). ISSN: 1340-6000. DOI: 10.1007/s10043-012-0023-9.
 - [29] Sourangsu Banerji and Berardi Sensale-Rodriguez. "A Computational Design Framework for Efficient, Fabrication Error-Tolerant, Planar THz Diffractive Optical Elements". In: *Scientific reports* 9.1 (2019), p. 5801. ISSN: 2045-2322. DOI: 10.1038/s41598-019-42243-5.
 - [30] Jörgen Bengtsson. "Kinoform design with an optimal-rotation-angle method". In: *Applied Optics* 33.29 (1994), pp. 6879–6884. ISSN: 2155-3165. DOI: 10.1364/AO.33.006879.
 - [31] J. Jahns et al. "Dammann Gratings For Laser Beam Shaping". In: *Optical Engineering* 28.12 (1989), pp. 1267–1275. ISSN: 0091-3286. DOI: 10.1117/12.7977142.
 - [32] Qing Cao and Jürgen Jahns. "Comprehensive focusing analysis of various Fresnel zone plates". In: *Journal of the Optical Society of America A* 21.4 (2004), pp. 561–571. ISSN: 1084-7529. DOI: 10.1364/josaa.21.000561.
 - [33] R. W. Gerchberg and W. O. Saxton. "A practical algorithm for the determination of the phase from image and diffraction plane pictures". In: *Optik* 35 (1972), pp. 237–246. ISSN: 00304026.
 - [34] J. R. Fienup. "Iterative Method Applied To Image Reconstruction And To Computer-Generated Holograms". In: *Optical Engineering* 19.3 (1980). ISSN: 0091-3286. DOI: 10.1117/12.7972513.
 - [35] Rainer G. Dorsch, Adolf W. Lohmann, and Stefan Sinzinger. "Fresnel ping-pong algorithm for two-plane computer-generated hologram display". In: *Applied Optics* 33.5 (1994), p. 869. ISSN: 2155-3165. DOI: 10.1364/AO.33.000869.
 - [36] Hui Pang et al. "Speckle-reduced holographic beam shaping with modified Gerchberg–Saxton algorithm". In: *Optics Communications* 433 (2019), pp. 44–51. ISSN: 00304018. DOI: 10.1016/j.optcom.2018.09.076.
 - [37] Chenliang Chang et al. "Speckle-suppressed phase-only holographic three-dimensional display based on double-constraint Gerchberg–Saxton algorithm". In: *Applied Optics* 54.23 (2015), p. 6994. ISSN: 2155-3165. DOI: 10.1364/AO.54.006994.

- [38] Tal Aharoni and Shy Shoham. “Phase-controlled, speckle-free holographic projection with applications in precision optogenetics”. In: *Neurophotonics* 5.2 (2018), p. 025004. DOI: 10.1117/1.NPh.5.2.025004.
- [39] Marc Guillon et al. “Vortex-free phase profiles for uniform patterning with computer-generated holography”. In: *Optics Express* 25.11 (2017), pp. 12640–12652. ISSN: 1094-4087. DOI: 10.1364/OE.25.012640.
- [40] Hui Pang et al. “High-accuracy method for holographic image projection with suppressed speckle noise”. In: *Optics Express* 24.20 (2016), pp. 22766–22776. ISSN: 1094-4087. DOI: 10.1364/OE.24.022766.
- [41] Olivier Ripoll, Ville Kettunen, and Hans Peter Herzig. “Review of iterative Fourier-transform algorithms for beam shaping applications”. In: *Optical Engineering* 43.11 (2004). ISSN: 0091-3286. DOI: 10.1117/1.1804543.
- [42] Robert W. Floyd and Louis Steinberg. “An Adaptive Algorithm for Spatial Greyscale”. In: *Proceedings of the Society for Information Display* 17.2 (1976), pp. 75–77.
- [43] P. W. M. Tsang and T-C Poon. “Novel method for converting digital Fresnel hologram to phase-only hologram based on bidirectional error diffusion”. In: *Optics Express* 21.20 (2013), pp. 23680–23686. ISSN: 1094-4087. DOI: 10.1364/OE.21.023680.
- [44] Gao Yang et al. “Error diffusion method with optimized weighting coefficients for binary hologram generation”. In: *Applied Optics* 58.20 (2019), pp. 5547–5555. ISSN: 2155-3165. DOI: 10.1364/AO.58.005547.
- [45] Reiner Eschbach. “Comparison of error diffusion methods for computer-generated holograms”. In: *Applied Optics* 30.26 (1991), pp. 3702–3710. ISSN: 0003-6935. DOI: 10.1364/AO.30.003702.
- [46] David Fischer and Stefan Sinzinger. “Evaluation of quadratic phase hologram calculation algorithms in the Fourier regime”. In: *Applied Optics* 59.6 (2020), pp. 1501–1506. ISSN: 0003-6935. DOI: 10.1364/AO.381547.
- [47] Hui Pang et al. “Accurate Hologram Generation Using Layer-Based Method and Iterative Fourier Transform Algorithm”. In: *IEEE Photonics Journal* 9.1 (2017), pp. 1–8. ISSN: 1943-0655. DOI: 10.1109/JPHOT.2016.2634783.
- [48] Yuanbo Deng and Daping Chu. “Coherence properties of different light sources and their effect on the image sharpness and speckle of holographic displays”. In: *Scientific reports* 7.1 (2017), p. 5893. ISSN: 2045-2322. DOI: 10.1038/s41598-017-06215-x.
- [49] Mehdi Askari and Jae-Hyeung Park. “Pre-compensation of an image blur in holographic projection display using light emitting diode light source”. In: *Optics Express* 28.1 (2020), p. 146. ISSN: 1094-4087. DOI: 10.1364/OE.381282.
- [50] Dukho Lee et al. “Speckle Reduction for Holographic Display Using Optical Path Difference and Random Phase Generator”. In: *IEEE Transactions on Industrial Informatics* 15.11 (2019), pp. 6170–6178. ISSN: 1551-3203. DOI: 10.1109/TII.2019.2927454.

-
- [51] Yuhei Kuratomi et al. “Speckle reduction mechanism in laser rear projection displays using a small moving diffuser”. In: *Journal of the Optical Society of America A* 27.8 (2010), p. 1812. ISSN: 1084-7529. DOI: 10.1364/JOSAA.27.001812.
 - [52] Jui-Wen Pan and Chi-Hao Shih. “Speckle reduction and maintaining contrast in a LASER pico-projector using a vibrating symmetric diffuser”. In: *Optics Express* 22.6 (2014), p. 6464. ISSN: 1094-4087. DOI: 10.1364/OE.22.006464.
 - [53] Tim Stangner et al. “Step-by-step guide to reduce spatial coherence of laser light using a rotating ground glass diffuser”. In: *Applied Optics* 56.19 (2017), p. 5427. ISSN: 2155-3165. DOI: 10.1364/AO.56.005427.
 - [54] Zhenxiang Zeng et al. “Speckle suppression in holographic displays using temporal averaging effect combined with rotating symmetric diffuser”. In: ed. by Anand K. Asundi and Yu Fu. SPIE Proceedings. SPIE, 2015, p. 952410. DOI: 10.1117/12.2189141.
 - [55] J. Amako, H. Miura, and T. Sonehara. “Speckle-noise reduction on kinoform reconstruction using a phase-only spatial light modulator”. In: *Applied Optics* 34.17 (1995), pp. 3165–3171. ISSN: 2155-3165. DOI: 10.1364/AO.34.003165.
 - [56] Wei-Feng Hsu and Chuan-Feng Yeh. “Speckle suppression in holographic projection displays using temporal integration of speckle images from diffractive optical elements”. In: *Applied Optics* 50.34 (2011), H50. ISSN: 2155-3165. DOI: 10.1364/AO.50.000H50.
 - [57] He Ma et al. “Influence of limited random-phase of objects on the image quality of 3D holographic display”. In: *Optics Communications* 385 (2017), pp. 153–159. ISSN: 00304018. DOI: 10.1016/j.optcom.2016.10.042.
 - [58] Jingzhao Zhang et al. “3D computer-generated holography by non-convex optimization”. In: *Optica* 4.10 (2017), p. 1306. ISSN: 2334-2536. DOI: 10.1364/OPTICA.4.001306.
 - [59] Tomoyoshi Shimobaba et al. “Lensless zoomable holographic projection using scaled Fresnel diffraction”. In: *Optics Express* 21.21 (2013), p. 25285. ISSN: 1094-4087. DOI: 10.1364/OE.21.025285.
 - [60] L. Golan et al. “Design and characteristics of holographic neural photo-stimulation systems”. In: *J. Neural Eng. (Journal of Neural Engineering)* 6.6 (2009), p. 066004. DOI: 10.1088/1741-2560/6/6/066004.
 - [61] Alexander Jesacher et al. “Full phase and amplitude control of holographic optical tweezers with high efficiency”. In: *Optics Express* 16.7 (2008), pp. 4479–4486. ISSN: 1094-4087. DOI: 10.1364/OE.16.004479.
 - [62] Shaohua Tao and Weixing Yu. “Beam shaping of complex amplitude with separate constraints on the output beam”. In: *Optics Express* 23.2 (2015), pp. 1052–1062. ISSN: 1094-4087. DOI: 10.1364/OE.23.001052.
 - [63] Tomoyoshi Shimobaba et al. “Improvement of the image quality of random phase-free holography using an iterative method”. In: *Optics Communications* 355 (2015), pp. 596–601. ISSN: 00304018. DOI: 10.1016/j.optcom.2015.07.030.
 - [64] Pengcheng Zhou et al. “30.4: Multi-Plane Holographic Display with a Uniform 3D Gerchberg-Saxton Algorithm”. In: *SID Symposium Digest of Technical Papers* 46.1 (2015), pp. 442–445. DOI: 10.1002/sdtp.10411.

- [65] T. Haist, M. Schönleber, and H. J. Tiziani. “Computer-generated holograms from 3D-objects written on twisted-nematic liquid crystal displays”. In: *Optics Communications* 140.4-6 (1997), pp. 299–308. ISSN: 00304018. DOI: 10.1016/S0030-4018(97)00192-2.
- [66] Yan Zhao et al. “Accurate calculation of computer-generated holograms using angular-spectrum layer-oriented method”. In: *Optics Express* 23.20 (2015), pp. 25440–25449. ISSN: 1094-4087. DOI: 10.1364/OE.23.025440.
- [67] Tullio Tommasi and Bruno Bianco. “Computer-generated holograms of tilted planes by a spatial frequency approach”. In: *Journal of the Optical Society of America A* 10.2 (1993), p. 299. ISSN: 1084-7529. DOI: 10.1364/JOSAA.10.000299.
- [68] Chenliang Chang, Jun Xia, and Yanqiao Jiang. “Holographic Image Projection on Tilted Planes by Phase-Only Computer Generated Hologram Using Fractional Fourier Transformation”. In: *Journal of Display Technology* 10.2 (2014), pp. 107–113. DOI: 10.1109/JDT.2013.2285174.
- [69] Hui Pang et al. “Non-iterative phase-only Fourier hologram generation with high image quality”. In: *Optics Express* 25.13 (2017), pp. 14323–14333. ISSN: 1094-4087. DOI: 10.1364/OE.25.014323.
- [70] Kyoji Matsushima, Hagen Schimmel, and Frank Wyrowski. “Fast calculation method for optical diffraction on tilted planes by use of the angular spectrum of plane waves”. In: *Journal of the Optical Society of America A* 20.9 (2003), pp. 1755–1762. ISSN: 1084-7529. DOI: 10.1364/josaa.20.001755.
- [71] Joseph Rosen. “Computer-generated holograms of images reconstructed on curved surfaces”. In: *Applied Optics* 38.29 (1999), pp. 6136–6140. ISSN: 0003-6935. DOI: 10.1364/AO.38.006136.
- [72] Graeme Whyte and Johannes Courtial. “Experimental demonstration of holographic three-dimensional light shaping using a Gerchberg–Saxton algorithm”. In: *New Journal of Physics* 7 (2005), p. 117. ISSN: 1367-2630. DOI: 10.1088/1367-2630/7/1/117.
- [73] Zhen Zhang et al. “Full-color holographic 3D display using slice-based fractional Fourier transform combined with free-space Fresnel diffraction”. In: *Applied Optics* 56.20 (2017), p. 5668. ISSN: 0003-6935. DOI: 10.1364/AO.56.005668.
- [74] Hui Pang et al. “Improvement of image quality of holographic projection on tilted plane using iterative algorithm”. In: *Optics Communications* 405 (2017), pp. 323–328. ISSN: 00304018. DOI: 10.1016/j.optcom.2017.08.048.
- [75] *Hamamatsu SLM products*. Accessed on 11 November 2020. URL: <https://www.hamamatsu.com/eu/en/product/optical-components/lcos-slm/index.html>.
- [76] *Jasper Display SLM products*. Accessed on 11 November 2020. URL: <https://www.jasperdisplay.com/slm-products/srk-overview/>.
- [77] *Meadowlark SLM products*. Accessed on 11 November 2020. URL: https://www.meadowlark.com/spatial_light_modulators.php.
- [78] *Santec SLM products*. Accessed on 11 November 2020. URL: <https://www.santec.com/en/products/components/slm/>.

-
- [79] *Texas Instruments DMD products*. Accessed on 11 November 2020. URL: <https://www.ti.com/dlp-chip/overview.html>.
 - [80] *Thorlabs SLM products*. Accessed on 11 November 2020. URL: https://www.thorlabs.com/newgrouppage9.cfm?objectgroup_id=10378.
 - [81] *Holoeye SLM products*. Accessed on 11 November 2020. URL: <https://holoeye.com/spatial-light-modulators/>.
 - [82] Grigory Lazarev et al. “Beyond the display: Phase-only liquid crystal on Silicon devices and their applications in photonics Invited”. In: *Optics Express* 27.11 (2019), pp. 16206–16249. ISSN: 1094-4087. DOI: 10.1364/OE.27.016206.
 - [83] Zichen Zhang, Zheng You, and Daping Chu. “Fundamentals of phase-only liquid crystal on silicon (LCOS) devices”. In: *Light: Science & Applications* 3.10 (2014), e213. ISSN: 2047-7538. DOI: 10.1038/lsa.2014.94.
 - [84] Emiliano Ronzitti et al. “LCoS nematic SLM characterization and modeling for diffraction efficiency optimization, zero and ghost orders suppression”. In: *Optics Express* 20.16 (2012), pp. 17843–17855. ISSN: 1094-4087. DOI: 10.1364/OE.20.017843.
 - [85] Martin Persson, David Engström, and Mattias Goksör. “Reducing the effect of pixel crosstalk in phase only spatial light modulators”. In: *Optics Express* 20.20 (2012), pp. 22334–22343. ISSN: 1094-4087. DOI: 10.1364/OE.20.022334.
 - [86] Hao Zhang et al. “Elimination of a zero-order beam induced by a pixelated spatial light modulator for holographic projection”. In: *Applied Optics* 48.30 (2009), pp. 5834–5841. ISSN: 2155-3165. DOI: 10.1364/AO.48.005834.
 - [87] Alexander Jesacher and Martin J. Booth. “Parallel direct laser writing in three dimensions with spatially dependent aberration correction”. In: *Optics Express* 18.20 (2010), pp. 21090–21099. ISSN: 1094-4087. DOI: 10.1364/OE.18.021090.
 - [88] David Engström et al. “Calibration of spatial light modulators suffering from spatially varying phase response”. In: *Optics Express* 21.13 (2013), p. 16086. ISSN: 1094-4087. DOI: 10.1364/OE.21.016086.
 - [89] Stephan Reichelt. “Spatially resolved phase-response calibration of liquid-crystal-based spatial light modulators”. In: *Applied Optics* 52.12 (2013), pp. 2610–2618. ISSN: 0003-6935. DOI: 10.1364/AO.52.002610.
 - [90] Tao Zhao et al. “Multi-region phase calibration of liquid crystal SLM for holographic display”. In: *Applied Optics* 56.22 (2017), p. 6168. ISSN: 0003-6935. DOI: 10.1364/AO.56.006168.
 - [91] José Luis Martínez Fuentes et al. “Interferometric method for phase calibration in liquid crystal spatial light modulators using a self-generated diffraction-grating”. In: *Optics Express* 24.13 (2016), p. 14159. ISSN: 1094-4087. DOI: 10.1364/OE.24.014159.
 - [92] Francisco J. Martínez et al. “Averaged Stokes polarimetry applied to evaluate retardance and flicker in PA-LCoS devices”. In: *Optics Express* 22.12 (2014), pp. 15064–15074. ISSN: 1094-4087. DOI: 10.1364/OE.22.015064.

- [93] Jorge García-Márquez et al. “Flicker minimization in an LCoS Spatial Light Modulator”. In: *Optics Express* 20.8 (2012), pp. 8431–8441. ISSN: 1094-4087. DOI: 10.1364/OE.20.008431.
- [94] Haolin Zhang et al. “LCoS display phase self-calibration method based on diffractive lens schemes”. In: *Optics and Lasers in Engineering* 106 (2018), pp. 147–154. ISSN: 01438166. DOI: 10.1016/j.optlaseng.2018.02.019.
- [95] David Marco et al. “Measuring the spatial deformation of a liquid-crystal on silicon display with a self-interference effect”. In: *Optics Letters* 45.16 (2020), pp. 4480–4483. ISSN: 0146-9592. DOI: 10.1364/OL.396105.
- [96] Lior Golan and Shy Shoham. “Speckle elimination using shift-averaging in high-rate holographic projection”. In: *Optics Express* 17.3 (2009), pp. 1330–1339. ISSN: 1094-4087. DOI: 10.1364/OE.17.001330.
- [97] Hidetomo Takahashi, Satoshi Hasegawa, and Yoshio Hayasaki. “Holographic femtosecond laser processing using optimal-rotation-angle method with compensation of spatial frequency response of liquid crystal spatial light modulator”. In: *Applied Optics* 46.23 (2007), pp. 5917–5923. ISSN: 2155-3165. DOI: 10.1364/AO.46.005917.
- [98] A. Lizana et al. “Influence of the incident angle in the performance of Liquid Crystal on Silicon displays”. In: *Optics Express* 17.10 (2009), pp. 8491–8505. ISSN: 1094-4087. DOI: 10.1364/OE.17.008491.
- [99] Andreas Hermerschmidt et al. “Wave front generation using a phase-only modulating liquid-crystal-based micro-display with HDTV resolution”. In: *Adaptive Optics for Laser Systems and Other Applications*. Ed. by Gilles Cheriaux, Chris J. Hooker, and Michal Stupka. Vol. 6584. SPIE, 2007, pp. 109–118. DOI: 10.1117/12.722891.
- [100] David Fischer and Stefan Sinzinger. “Control of Projection Uniformity and Fidelity in Spatial Light Modulator-Based Holography”. In: *2019 IEEE International Conference on Mechatronics (ICM)*. IEEE, 2019, pp. 129–134. ISBN: 978-1-5386-6959-4. DOI: 10.1109/ICMECH.2019.8722858.
- [101] W. H. Southwell. “Wave-front estimation from wave-front slope measurements”. In: *Journal of the Optical Society of America* 70.8 (1980), p. 998. ISSN: 0030-3941. DOI: 10.1364/JOSA.70.000998.
- [102] Victor Arrizón et al. “Iterative optimization of phase-only diffractive optical elements based on a lenslet array”. In: *Journal of the Optical Society of America A* 17.12 (2000), p. 2157. ISSN: 1084-7529. DOI: 10.1364/JOSAA.17.002157.
- [103] Tomoyoshi Shimobaba and Tomoyoshi Ito. “Random phase-free computer-generated hologram”. In: *Optics Express* 23.7 (2015), pp. 9549–9554. ISSN: 1094-4087. DOI: 10.1364/OE.23.009549.
- [104] Michal Makowski, Tomoyoshi Shimobaba, and Tomoyoshi Ito. “Increased depth of focus in random-phase-free holographic projection”. In: *Chinese Optics Letters* 14.12 (2016), pp. 120901–120905. ISSN: 1671-7694. DOI: 10.3788/COL201614.120901.

- [105] Max Born and Emil Wolf. *Principles of optics: Electromagnetic theory of propagation, interference and diffraction of light*. 7th ed., 11th reprinting. Cambridge: Cambridge Univ. Press, 2016. ISBN: 9780521642224.
- [106] Tatiana Latychevskaia. “Lateral and axial resolution criteria in incoherent and coherent optics and holography, near- and far-field regimes”. In: *Applied Optics* 58.13 (2019), pp. 3597–3603. ISSN: 2155-3165. DOI: 10.1364/AO.58.003597.
- [107] Stefan Sinzinger and Jürgen Jahns. *Microoptics*. 2., rev. and enl. ed. Weinheim: Wiley-VCH, 2003. ISBN: 3-527-40355-8.
- [108] Sebastian Schlangen et al. “Autofocusing system for spatial light modulator-based maskless lithography”. In: *Applied Optics* 55.8 (2016), p. 1863. ISSN: 2155-3165. DOI: 10.1364/AO.55.001863.